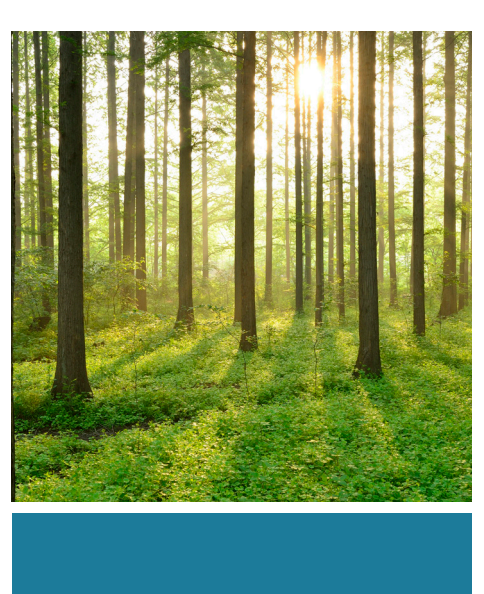
EFFECT OF ROOM TEMPERATURE DIFFERENCES ON SAFETY-RELATED REINFORCED CONCRETE FLOORS AND WALLS IN THE REACTOR BUILDING OF OL2 NPP

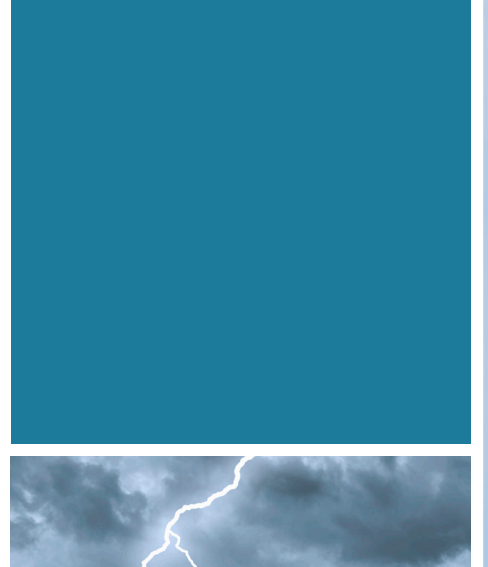
REPORT 2021:728







NUCLEAR POWER CONCRETE TECHNOLOGY









Effect of room temperature differences on safety-related reinforced concrete floors and walls in the reactor building of OL 2 NPP

VILJAMI RIEKKINEN

Foreword

This study was completed as a master's thesis that finalizes the studies of a Master of Science in Technology in Aalto University School of Engineering. The study is made in collaboration with Sweco Rakennetekniikka Oy and Teollisuuden Voima Oyj (TVO), and it is funded by Energiforsk AB.

I want to thank Energiforsk for funding the study as well as Sweco and TVO for giving the opportunity to complete such an interesting project. I am grateful for the guidance given by the supervising professor from Aalto University and thesis advisor M.Sc. (Tech) Jyrki Jauhiainen.

This project was carried out in the Energiforsk Nuclear Concrete Research Program, with stakeholders Vattenfall, Uniper/Sydkraft Nuclear, Fortum, Teollisuuden Voima Oy (TVO), Skellefteå Kraft, Karlstads Energi and the Swedish Radiation Safety Authority (SSM).

These are the results and conclusions of a project, which is part of a research programme run by Energiforsk. The author/authors are responsible for the content.



Sammanfattning

I denna rapport studerades inverkan av temperaturskillnader mellan 20°C och 65°C på den strukturella integriteten hos väggar och golv av armerad betong i reaktorbyggnaden till kärnkraftverket Olkiluoto 2. Undersökningen utfördes med finita element-modellering. Reaktorbyggnaden är en monolitisk betongkonstruktion som har minimalt med dilatationsfogar. På grund av skillnader i temperatur mellan olika rum utsätts byggnaden för termiska spänningar. Dessa kan delas in i primära termiska spänningar som härrör från olinjära temperaturfördelningar på grund av transienta effekter samt kontinuerliga termiska spänningar som uppstår på grund av tvång i den statiskt obestämd strukturen.

Målet med studien var att med finita element analys (FEA) undersöka om de termiska spänningarna som uppkommer under normala driftsförhållanden är tillräckligt stora för att orsaka sprickbildning i betongen. De beräknade termiska spänningarna jämfördes även med med mekaniska spänningar orsakade av laster i bruksgränstillståndet. Resultatet från FEA tyder på att en temperaturskillnad på endast 20°C inducerar termiska spänningar som överstiger betongens draghållfasthet och även överstiger de mekaniska spänningarna i av brukslaster i reaktorbyggnaden. Sprickbredderna beräknades enligt metoden som ges i Eurokod 2. Resultaten visade att sprickbredderna var mindre än det rekommenderade maxvärdet på 0,3 mm med den rådande temperaturfördelningen med en maximal temperatur på cirka 40 °C. När temperaturen och temperaturskillnaden ökas till det maximala av det studerade området, överskrider de beräknade sprickbredderna det rekommenderade maxvärdet. Dock underskrider de beräknade sprickbredderna generellt 1,0 mm. Resultaten visar även att krypning av betongen tenderar att minska storleken på de termiska spänningarna, och därför uppstår inte några genomgående sprickor i varekn väggar eller golv. Dessa resultat indikerar att reaktorbyggnadens strukturella integritet inte påverkas under normala driftsförhållanden mellan 20 och 65 °C. De situationer där termiska och mekaniska påkänningar samverkar bör dock studeras noggrannare.

Resultaten från FEA indikerar också att storleken på de kontinuerliga termiska spänningarna är betydligt större än de primära termiska spänningarna i denna applikation. Detta kan förklaras av att reaktorbyggnadens termiska expansionsbegränsande randvillkor och den relativt låga temperaturskalan i kombination med den svaga termiska konvektionen mellan rumsluft och betongytor. I praktiken betyder detta att vid avställning p.g.a. revision, vilket medför att temperaturen ändras över tiden, inte medför några betydande risker för strukturens integritet.

Studien innehåller också en litteraturöversikt om temperaturberoendet hos betongens termiska och mekaniska egenskaper. I det studerade temperaturområdet kunde något signifikant temperaturberoende av de termiska egenskaperna inte påvisas. Beroende på betongblandningen varierade emellertid storleken på dessa egenskaper avsevärt, särskilt värmeutvidgningskoefficienten. När det gäller de mekaniska egenskaperna, var tryckhållfasthet och brottöjning samt elasticitetsmodulen avsevärt temperaturberoende, även om vissa modeller indikerade att påverkan var försumbar.



Summary

This report studied the integrity of the reinforced concrete walls and floors in the reactor building of the Olkiluoto 2 nuclear power plant between temperatures of 20 to 65 °C using FE modelling. The reactor building is monolithic where the number of structural joints is minimized. With room temperature differences, the building is imposed to two types of thermal stresses: primary thermal stresses arising from nonlinear temperature distributions due to transient effects and continuity thermal stresses arising from restrained deformations as the structure is statically indeterminate.

The goal of the study was to estimate the magnitudes of thermal stresses compared to structural, mechanical stresses in normal operational conditions and to determine if the thermal stresses are large enough to cause significant crack widths. The results of the FEA suggests that thermal stresses can induce tensile stresses that exceed those induced by the mechanical stresses in the reactor building even with temperature differences of 20 °C. However, the crack widths evaluated by the method given by Eurocode 2 are smaller than a recommended value of 0.3 mm with the current temperature distribution with a maximum temperature of some 40 °C. When the temperature and the temperature difference is increased to the maximum of the studied range, the crack width estimates exceed the recommended value, though remaining in values that generally are clearly under 1.0 mm. Additionally according to the results, creep tends to decrease the magnitude of thermal stresses, and no through-thickness cracking of concrete is expected. These results suggest that the integrity of the reactor building is not critically impaired in normal operational conditions between 20 and 65 °C. However, attention should be given to situations where thermal and mechanical stresses simultaneously induce tension to a structural piece.

The results of FEA also suggest that the magnitude of continuity thermal stresses dominate over the primary thermal stresses in this application. This can be explained by the thermal expansion restraining boundary conditions of the reactor building and the relatively low temperature scale coupled with the weak thermal convection between room air and concrete faces. In practice, this means that maintenance ramp-ups, where temperature develops with time, are not significant a risk considering the integrity of the structure.

The study also includes a literature review on the temperature dependence of the thermal and mechanical properties of concrete. In the studied temperature range, the thermal properties showed no significant temperature dependence. However, depending on the concrete mix, the magnitude of these properties varied significantly, especially the coefficient of thermal expansion. As for the mechanical properties, compressive stress and strain as well as the modulus of elasticity showed considerable temperature dependence, although some models suggested negligible dependence.



List of content

1	Introd	uction		8
2	The re	actor bu	ilding of OL2 NPP unit	11
	2.1	Genera	linformation	11
	2.2	Geome	try and safety features	11
	2.3	Temper	rature information	14
3	Therm	al effect	s in reinforced concrete structures	16
	3.1	Genera	linformation	16
	3.2	Mechar	nical properties and cracking mechanism	16
	3.3	Temper	rature dependence of thermo-mechanical properties	19
		3.3.1	Stress and strain characteristics at elevated temperatures	21
		3.3.2	Thermal properties at elevated temperatures	24
	3.4	Therma	al loads	27
		3.4.1	Primary stresses	28
		3.4.2	Continuity stresses	31
		3.4.3	Total thermal stresses	32
	3.5	Concre	te creep	33
1	Finite	element	modelling	34
	4.1	Genera	linformation	34
	4.2	Modelli	ing goals	34
		4.2.1	Goal 1	35
		4.2.2	Goal 2	35
		4.2.3	Goal 3	35
		4.2.4	Goal 4	36
	4.3	Materia	al model and parameters	36
	4.4	Global	modelling	39
		4.4.1	Topology and element types	39
		4.4.2	Loading of the global model	44
		4.4.3	Boundary conditions	45
		4.4.4	Global modelling results	45
5	Local r	nodellin	g	54
	5.1	Genera	linformation	54
	5.2	Modelli	ing principles	54
	5.3	Topolog	gy and element types	55
		5.3.1	Elements of thermal analyzes	56
		5.3.2	Elements of structural analyzes	56
	5.4	Results	for linear temperature distribution	57
	5.5	Results	for nonlinear temperature distribution	65
5	Error a	analysis,	conclusions and future research	76
	6.1	-	s of error	76



6.2	Conclusions and future research	78
References		81
Table of An	nexes	83
Annex 1. Crack width calculations according to Eurocode 2 Part 1-1		84
Annex 2. Cr	ack width calculations (Global model)	85
Annex 3. Cr	ack width calculations (Local model)	88



1 Introduction

Nuclear power corresponds to around 25 % of the consumption of electrical energy in Finland in the 21st century (Suomen virallinen tilasto 2018). The relevance and share of nuclear power in Finland are not vanishing, which is supported by the implementation of Olkiluoto 3 nuclear power plant unit in the near future. Due to the high share of consumption, the safe and uninterrupted production of nuclear energy is essential for the energy needs of the society. To guarantee the safe operation of nuclear power plants (commonly abbreviated "NPP" in this thesis), independent internal and external oversights are performed together with continuous research and development activities.

Nuclear power plants are commonly made of reinforced concrete with or without pre-stressed concrete, depending on the application of individual buildings. Concrete is a well-known building material and its properties have been researched widely which enforces its use in many applications. However, one of the most well-known downsides of concrete is its relatively low tensile strength which exposes the material to cracking failure if the tensile strength is exceeded. According to Eurocode 2 part 1-1 (EN1992-1-1) design standard, cracking is normal and even expected in reinforced concrete structures, but it should be limited to an extent that will not impair the function, durability or visuality of the structure. Concrete cracking can be initiated by many actions including ordinary structural loading, chemical actions or imposed deformations.

This thesis studies the effect of temperature differences between rooms in reinforced concrete walls and floors in an NPP application. Temperature variations are known to induce thermal loads and therefore tensile stresses that exceed the tensile strength of the concrete, thus inducing cracking. There are two main types of thermal stresses: the continuity thermal stresses that are induced by restrained thermal strains in statically indeterminate structures, and primary thermal stresses that are induced by non-constant temperature gradients. (Vecchio 1987.) The cracking mechanism in both these types ultimately relates to the difference in free thermal strain and the actual strain of the structure.

In this thesis, the reactor building of Olkiluoto 2 NPP unit is used as a case study. The whole NPP of Olkiluoto (commonly abbreviated "OL") with all three of its units are shown in Figure 1. The reactor building is a part of the multi-level radioactive substance isolation system that isolates radioactivity of the fuel used in the plant's operation from the environment (TVO 2013). Therefore, its structural integrity is critical for safe operation of the NPP unit. In the design phase of the reactor building, some of its rooms were assigned a design temperature of 40 °C which corresponds to a temperature difference of some 20 °C to adjacent rooms. Currently, the temperatures of these rooms tend to rise to values that exceed the design temperature difference. The raise of temperature is likely for example due to increased power output of the unit which has risen from 660 megawatts to 890 MW during its lifetime and changes made in thermal isolation. As thermal loads induce cracking, the rise of temperature must be studied carefully in order to determine if larger temperature differences than assumed during design are allowable.





Figure 1. The three NPP units of Olkiluoto from left to right: OL3, OL1 and OL2. The reactor buildings of OL1 and OL2 are identifiable for being the tallest structures.

The reactor building is monolithic meaning it was cast in-situ. Due to this production method, the number of structural joints is minimized, and most of the structural pieces (i.e. walls and floors) are fixed to each other. When the structure tries to deform, for example due to temperature differences, the adjacent pieces tend to restrain the deformation inducing a stress state near the crossing of two or more structural pieces. If the stress state is such that the tensile strength of concrete is exceeded, cracking will occur. However, its extent should be limited. In Eurocode 2 part 1, the crack width in serviceability limit state is limited to recommended maximum values depending on the exposure class of the concrete. Therefore, it is natural to study not only if cracking will occur (i.e. the tensile strength of concrete is locally exceeded) but also what is the magnitude of crack widths.

To study the severity of thermal loading caused by temperature differences between rooms, four goals are introduced. Firstly, what is the severity of stresses caused by thermal loading in comparison with ordinary structural loads? Secondly, are the primary thermal stresses relevant in the reactor building, i.e. do they significantly increase the severity of thermal stresses? Thirdly, what is the extent of cracking in terms of maximum crack width with combined action from structural loading and the thermal loads? Lastly, how will concrete creep affect the stress state and therefore the cracking of the structure with given loading?

The creep effect can increase the strains from static loading over time, but if the deformations are restricted stresses can decrease due to relaxation (Bazant and Jirasek 2018) resulting into a redistribution of stresses and decrease in structural stiffness. The decrease of stiffness should also decrease thermal stresses, as thermal stresses are proportional to the stiffness. Therefore, creep effect will be studied.

To tackle the stated goals, numerical modelling in terms of Finite Element Method ("FEM") is used. Global modelling in the scale of the whole reactor building is performed with shell elements. The goal of global modelling is to find possible hotspots prone to cracking by altering the temperatures of certain rooms. Then, local modelling is performed with solid elements to yield more applicable results. In



local modelling, both nonlinear and linear temperature distributions are assumed to compare the severity of the two types of thermal stresses.

The study includes some restrictions or limitations. The studied temperature ranges from 20 to 65 °C. This is because the properties and/or microstructure of concrete can vary significantly at larger temperatures, and thus the modelling could turn out to be too complex in the framework of this thesis. Also, it is not expected that the actual temperature of the studied reactor building rooms would increase above 65 °C. Furthermore, the American Association of Mechanical Engineers have limited the normal long-term operation temperature in NPP containment buildings to this maximum temperature (Ashar et al. 2009). Additionally, the study is limited to non-accidental situation where the magnitudes of mechanical loads are assumed to correspond to normal operation of the reactor building. The material parameters used do not consider aging of material or the loading history of the building.

The structure of this thesis is as follows. In Chapter 2, the NPP unit of Olkiluoto 2 is discussed briefly, mostly focusing on the reactor building. Then, in Chapter 3 the properties of concrete at elevated temperatures and the mechanisms of thermal stresses are discussed. Chapter 4 discusses the modelling goals as well as principles used for global modelling and the results received by this approach. After global modelling, Chapter 5 concentrates on local modelling. Then, in Chapter 6 sources of error are discussed, final conclusions are made and suggestions for future research are given.



2 The reactor building of OL2 NPP unit

2.1 GENERAL INFORMATION

This chapter introduces the parts of the reactor building of OL2 NPP that are relevant in the scope of this thesis. First, a general overview of the operations of the OL NPP is given. This is followed by a description of the function of the reactor building and its role to the safety of the NPP unit. Then, some structural information and rules regarding the room temperatures of the reactor building are presented.

The nuclear power plant of Olkiluoto is located at Eurajoki, Finland and it consists of three individual units. The plant is owned and operated by TVO (Teollisuuden voima Oyj). The first two units (OL1 and OL2) are boiling water reactors, and they are nearly identical to each other. They were designed and built in the 1970's, and finally their commercial use started in 1979 (OL1) and 1982 (OL2). At first, the net power output of each unit was 660 megawatts which has then risen to 890 MW in today's operation. Figure 2 shows the layout of OL1/OL2 units together with the list of each individual building by their application. Additionally, a third unit known as Olkiluoto 3 (OL3) is being built at the time of writing of this thesis. Unlike the two first units, OL3 unit is a European pressurized water reactor. (TVO 2020.)

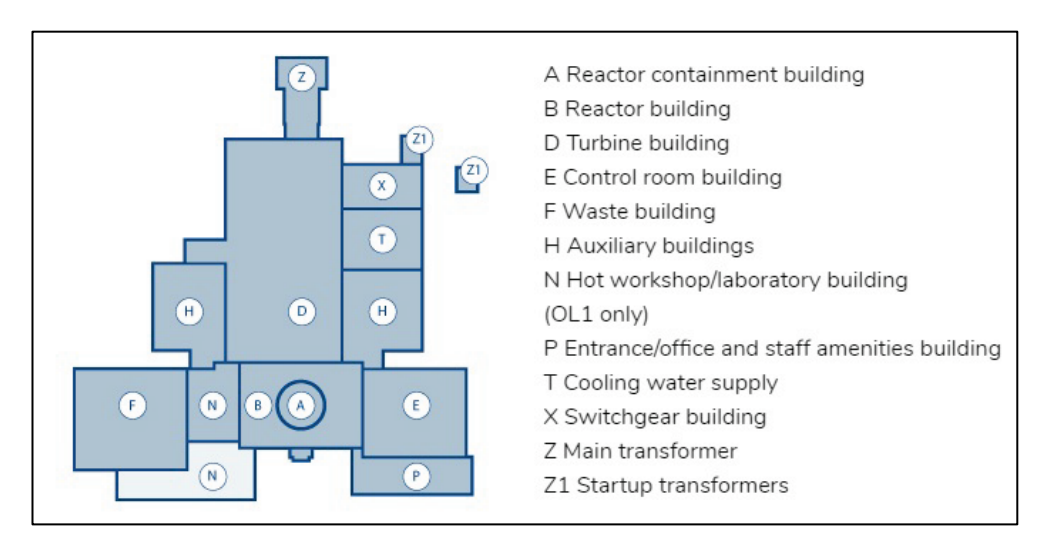
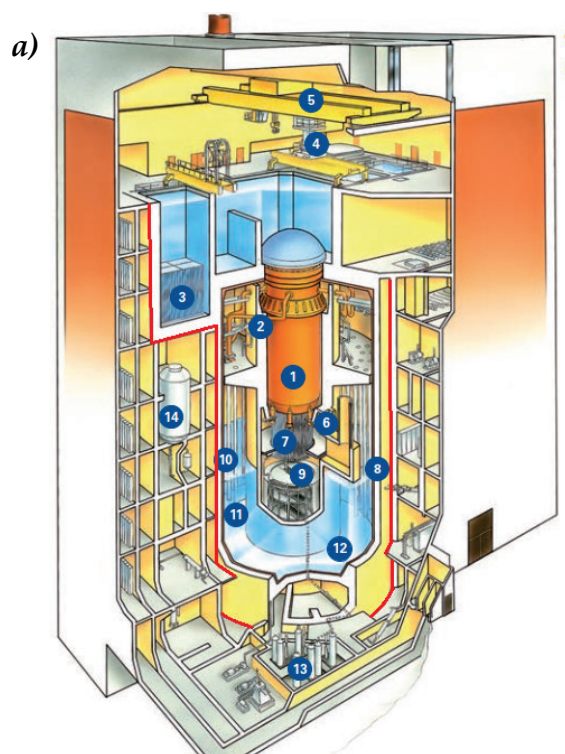


Figure 2. A layout of OL1/OL2 NPP units with a list of individual buildings (TVO 2020).

2.2 GEOMETRY AND SAFETY FEATURES

In the scope of this thesis, walls and floors of the reactor building of OL2 unit are of interest. Figure 2 shows the position of the reactor building (marked as area "B") in the layout of OL1/OL2 units, and Figure 1 shows an actual photo of the plant, where the reactor buildings are identifiable for being the tallest structures. Figure 3 shows a schematic cross-section of the reactor building and the containment building.





Cross section of the reactor and containment buildings

- 1. Reactor pressure vessel
- Main stream lines Fuel pool
- 4. Reactor service bridge
- 5. Reactor hall crane6. Recirculation pumps
- Control rod drives
- 8. Containment
- 9. Control rod service platform
- 10. Blow-down pipes
- 11. Embedded steel liner
- 12. Condensation pool
- 13. Scram system tracks
- 14. SAM scrubber

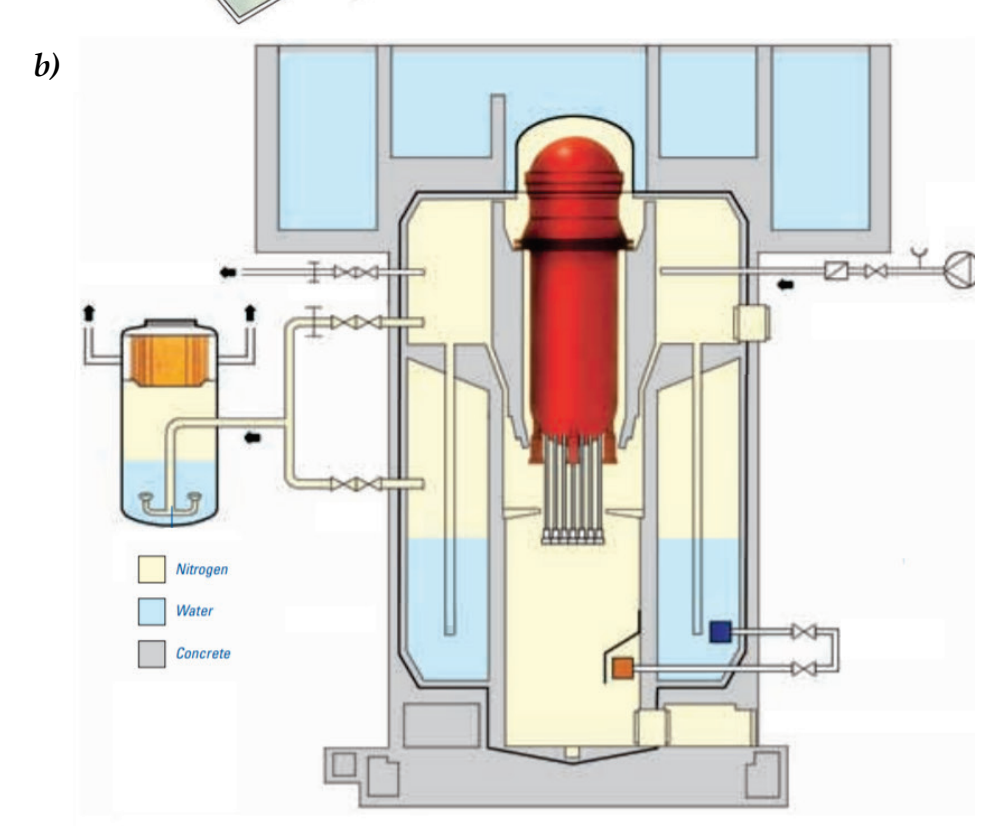


Figure 3. α) Cross section of the reactor building including the containment building and the reactor (TVO 2013, modified). Red line coarsely represents the border between containment building and reactor building. b) Crosssectional geometry of the containment building (TVO 2007, modified).



The reactor building has several operational and safety functions. First, it holds the containment building and the reactor within itself. It also contains storage space for fuel and cranes for transferring fuel and other heavy objects. Additionally, it holds considerable number of supporting mechanisms such as piping, and parallel safety systems to guarantee safe operations in normal use and accidental situations. As an example of a safety system, the emergency cooling system is located in the bottom of the reactor building, as indicated by number 13 in Figure 3.

In order to guarantee nuclear safety, wide-ranging safety precautions are used. The safety systems are designed and implemented according to the defence-in-depth philosophy, where multiple parallel systems and mechanisms prevent accidents even with human errors. The reactor safety is based on a multi-level physical isolation of radioactive matter from the natural environment. In this multi-level system, the reactor building serves as a secondary containment building being the fifth isolator. The four other isolators are ceramic fuel, gas-tight fuel rod, reactor pressure vessel and the containment building, as shown in Figure 4. (TVO 2013.)

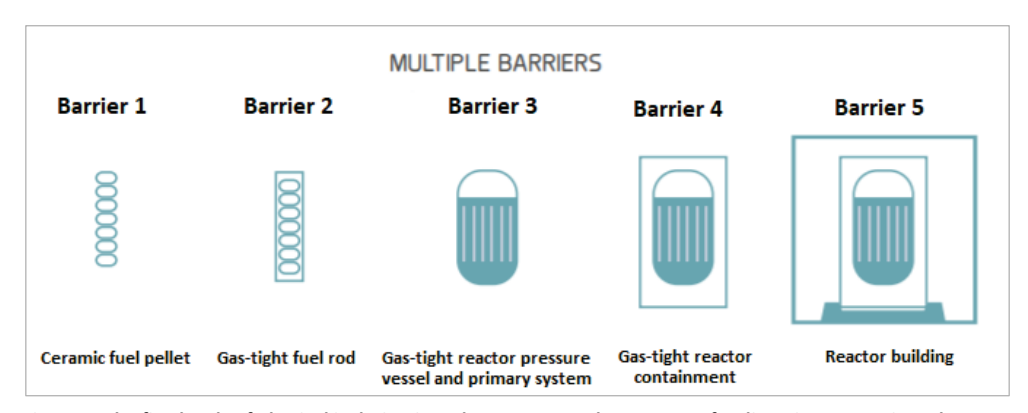


Figure 4. The five levels of physical isolation in order to prevent the passage of radioactive matter into the environment (TVO 2013, modified).

According to the drawings delivered by TVO, the perimeter of the reactor buildings is formed by a rectangle with lengths of some 52 and 40 meters. The lowest elevation is nine meters below ground, and the building raises to a height of 63 meters. The containment building inside the reactor building is crudely a cylinder-shaped building with a diameter of some 24 meters. The fuel pool, reactor pool and other pools in the upper spaces of Figure 3 are parts of the containment building. The reactor building is separated from the containment building and the surrounding buildings by expansion joints. For clarity, when speaking of reactor building from here on, it covers only area *B* excluding area *A* in the layout shown in Figure 2, and it refers to the reactor building of OL2 NPP unit solely.

Since this thesis studies the reactor building without the containment building, the topology of the calculation model will be such that there will be a large cylinder-shaped empty space in the middle of the building. Also, the fuel and condensation pools are parts of the containment building and thus are not part of the calculation model. The topology of the global calculation model is shown in Figure 15.



The wall thicknesses of the reactor building vary from 200 mm to 1200 mm, and the floor thicknesses vary from 200 mm to some 1000 mm. As a rule of thumb, the wall and floor thicknesses increase approaching to the containment building, where piping and other technical systems are located. The floor levels, excluding the upmost part of the reactor building, range from 3 500 mm to 6 500 mm.

It is evident that the reactor building has major importance in the overall safety of the plant unit. It is in itself a physical obstacle and it contains numerous safety systems. Therefore, any changes in the conditions of the structure that might compromise its integrity must be considered carefully. In the scope of this thesis, effects of increased room temperature differences are considered. Temperature variations can induce thermal loads large enough to cause concrete cracking, especially when paired with other loads. In this study, thermal loads are accompanied by mechanical loads shown in Table 7. If the reactor building has excessive cracking in walls or floors, the isolation can be compromised. Cracks can also act as barriers of heat conduction, harming the transfer of heat within solids of the structure. Through-thickness cracks can also create passages for fluids that can, for example, allow harmful gas leaks.

2.3 TEMPERATURE INFORMATION

Observing the conditions of rooms in the reactor building is important in order to guarantee safe operation by noticing any deviations quickly. The monitored conditions include quantities such as temperature, humidity, air pressure and gas composition. According to the safety analysis report of OL1 and OL2 units, a room temperature deviation of 2 ... 5 °C can already suggest a leakage or fault in air cooling. Depending on the applications of the rooms, these quantities have certain reference values in normal operations, minor accidents or major accidents. Predetermined threshold deviations from the reference values will trigger an alarm. Normally, the threshold is 5...10 % of the mean room temperature.

During the making of this thesis, daily temperature measurement data of numerous rooms in the reactor building since year 2003 have been available. The data is delivered directly by TVO. In the modelling phase, this allows for the use of more precise initial conditions that describe the actual operation conditions.

Room temperature changes can induce thermal loads in two main mechanisms that are relevant in the reactor building. The first mechanism is linked to static temperature differences. During normal operations, the plant unit works in quite a stable manner. In practice this means that the conditions should not vary significantly or at all in short timespans. For example, the room temperatures are semi-constants, but if the temperature of the structure differs from the reference temperature for thermal strains, static thermal loads are induced if the structure is restrained from deformations (Vecchio 1987). The other mechanism is linked to temperature changes that are functions of time. During annual maintenance overhauls the operation stalls and a drop in the room temperatures of the reactor building is expected. After the overhaul, the room temperatures again raise to the operational temperatures. According to the provided temperature data, it takes roughly four to 10 days to find the equilibrium temperature after ramp-up or



ramp-down with largest temperature differences occurring during the first day or two. In ramp-up or ramp-down situations, the room air temperature changes faster to the new equilibrium than the mean temperature of the concrete walls and floors of the same room, as illustrated in Figure 5. This can be explained by the fact that the heat from piping and machinery is (usually) first transmitted to room air which then transfers heat to walls and floors. While the temperature distribution in the concrete is setting towards the new equilibrium, a nonlinear temperature distribution can be formed, if the room temperatures change suddenly. As will be covered in Chapter 3, nonlinear temperature distributions in a body induce primary thermal loads that can harm the structure even if deformations are not restricted (Vecchio 1987).

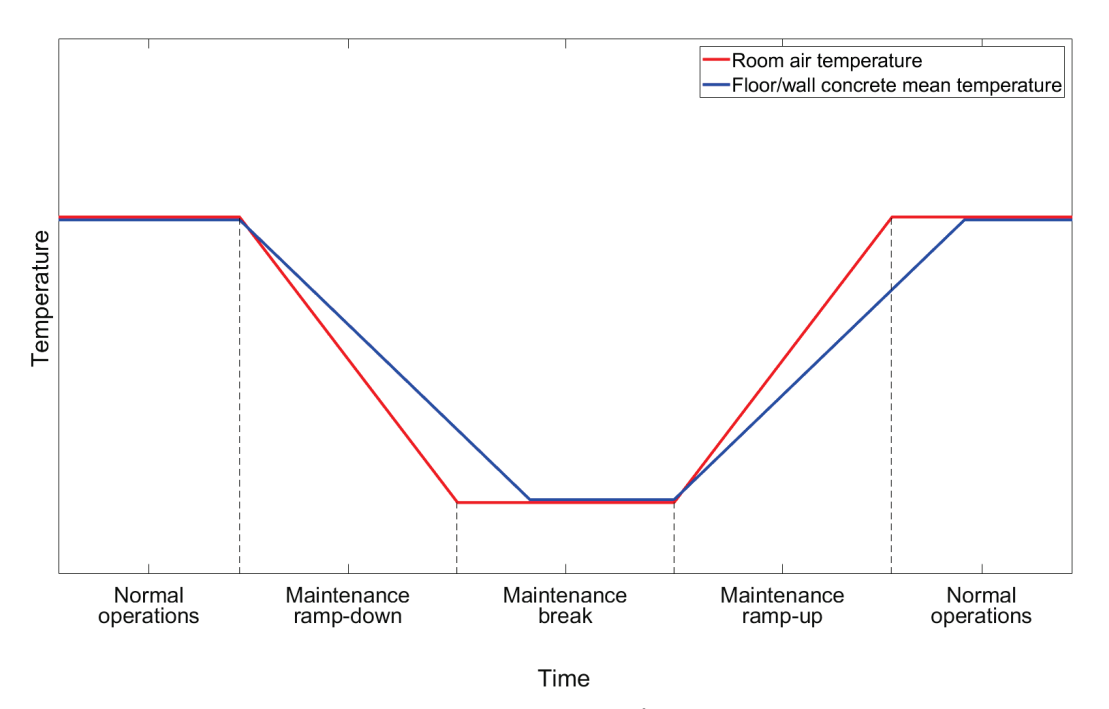


Figure 5. Illustration of room air temperature and mean concrete wall/floor temperature in maintenance ramp-down and ramp-up.



3 Thermal effects in reinforced concrete structures

3.1 GENERAL INFORMATION

Reinforced concrete is a common building material used in wide range of applications. At its essence, concrete is a mixture of water, cement and aggregate, i.e. grained materials such as gravel. Often, additives such as fly ash are added for certain applications. Depending on the ingredients and their ratios in the concrete mix, the final concrete structure can have a broad range of varying properties compared to other concrete mixes. Regardless of the large variety of possible concrete mixes, concrete as a building material has been studied comprehensively and some general thermal and mechanical properties for typical mixtures can be listed.

The aim of this chapter is to describe the effect of thermal loading in reinforced concrete structures. First, the mechanical properties of concrete and the reasons for concrete cracking are discussed. Then, the effects of moderately elevated temperatures, i.e. temperatures between 20 and 65 °C, to the mechanical and thermal properties of concrete are studied. After this, the origins of thermal loads are studied, and finally the creep effect of concrete structures is discussed.

3.2 MECHANICAL PROPERTIES AND CRACKING MECHANISM

Concrete is known for its relatively good resistance against compressive stresses. According to Eurocode 2 part 1, the mean value of concrete cylinder compressive strength, denoted by f_{cm} , varies from 20 to 98 MPa with typical strength classes. Simultaneously, the characteristic mean axial tensile strength of concrete, denoted by f_{ctm} , varies from 1.6 to 5.0 MPa. This means that the tensile strength is typically less than 10 % of the compressive strength, although this is dependent on several factors including the composition of the concrete and the test procedure (Wight and MacGregor 2012). Due to the large difference in compressive and tensile strengths, the tensile capacity of concrete is often neglected in design. For example, in the ultimate limit state design according to Eurocode 2 part 1-1, the tensile capacity of concrete is often disregarded when calculating the overall bending moment capacity of cross-sections.

A common shape of uniaxial stress-strain relation of plain concrete in both tension and compression is shown in Figure 6. It is worthy to mention that the tangent modulus of elasticity at zero strain, in the figure denoted by E_{θ} , is equal in both compression and tension. The compressive side of the curve shows clear nonlinearity before peak stress. In design standards the stress-strain relation of concrete in compression has many alternative forms. In Eurocode 2 ("EC2"), fully non-linear, parabola-rectangle or bi-linear compressive uniaxial stress-strain curves are defined for designing structures, but other idealizations are also applicable. However, instead of tangent modulus of elasticity at zero strain, EC2 uses secant modulus of elasticity which effectively averages the modulus of elasticity to a range of strains.



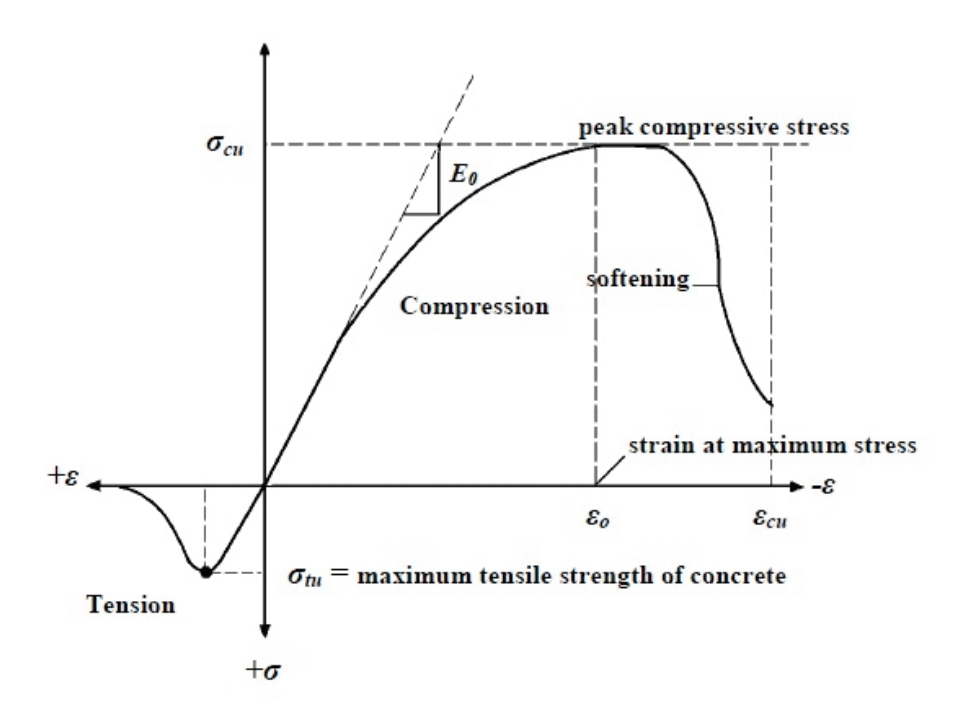


Figure 6. Illustration of stress-strain relationship of concrete in tension and compression (Hind, Mustafa and Talha (2016)). The scale does not represent true stress and strain ratios in tension and compression for typical concrete.

Cracking is expected in the design of concrete structures, and it can have multiple different origins, including cracks caused by mechanical loading, imposed deformations or by combination of such actions. Ultimately speaking, the cause of concrete cracking is the exceedance of its tensile strength. Cracking first initiates at the vicinity of the most tensioned point of the structure, often called the *fracture process zone*, if the tensile stresses exceed the tensile strength (Wight and MacGregor 2012). As cracking propagates, the stiffness of the cracked parts decreases and stresses within concrete are redistributed from cracked to undamaged parts. As shown in Figure 6, the tensile capacity of concrete decreases to zero with increasing strain after the tensile strength presenting a mechanism known as *tension softening* (Chen and Su 2013) which is a relevant when studying crack propagation.

Determining the compressive and tensile strengths of concrete with standardized testing procedures yield good initial values for the strength properties. However, in concrete structures the effective strength and strain properties (stress and strain state at failure) depend largely on the type of loading the structure is subjected to. For example, the strain corresponding to the maximum tensile stress is 0.01 % in pure tension and from 0.014 to 0.02 % in flexure (Wight and MacGregor 2012). Therefore, depending on the loading scenario the failure might occur at stress and strain values that differ from the values determined with the uniaxial test samples, as shown by Kupfer et al. (1969) regarding biaxial loading. As a practical design example, EC2 part 1-1 allows an increase in compressive strength and maximum strain when the structure is confined.



The dependence of loading scenario to the effective strength can easiest be discussed by studying concrete subjected to biaxial loading. In biaxial loading, a structural element is loaded simultaneously in two non-parallel directions. An example from such situation is shown in Figure 7c, where a concrete element is loaded in two perpendicular directions, while the direction perpendicular to those two directions is free.

Figure 7a can be used to determine the combination of stresses that yield to failure of concrete and to compare the stress state in failure to the uniaxial compressive and tensile strengths f_c' and f_t' , respectively. When the concrete element is loaded in biaxial tension (curve B - D - B' in Figure 7), the failure stress in the loading directions is effectively the same as f_t' , as shown by point D in comparison with point B and as reported by Kupfer et al. (1969). When the element is loaded in tension and compression (curve B - A) the tensile stress in failure in the tensile loading direction is effectively smaller than f_t' . The two above-mentioned loading scenarios correspond to Zones 1 and 2 marked in Figure 7. In these zones, the failure is caused by cracking, and the crack faces are perpendicular to the maximum principle tensile stress (Wight and MacGregor 2012).

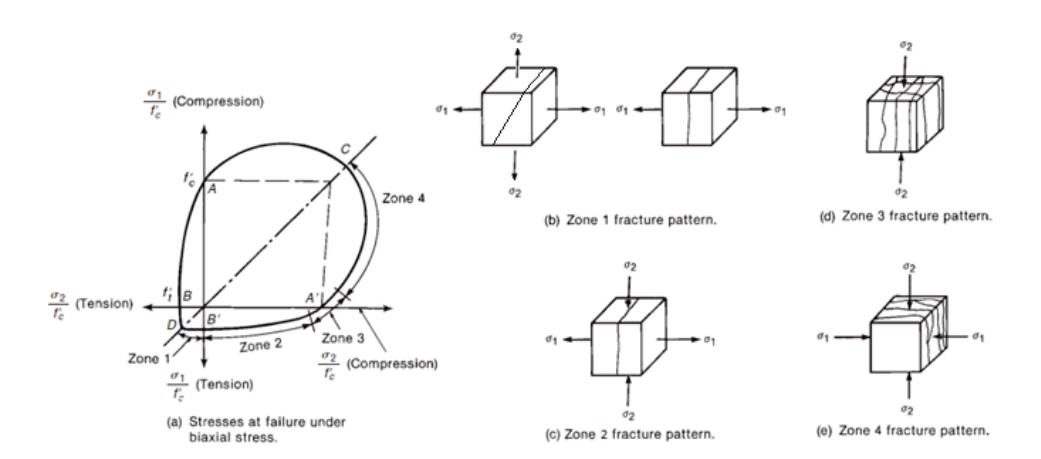


Figure 7. Failure envelope of concrete in biaxial loading. (Modified from Wight and MacGregor (2012)).

When the element is loaded in uniaxial compression as shown by Figure 7d, the failure occurs by crack planes having normal perpendicular to the applied compressive stress (Kupfer et al. 1969). Finally, curve A - C corresponds to biaxial compression loading. As shown by Figure 7a, the principle compressive stress can exceed uniaxial compressive stress f_c' without leading to failure in this loading scenario. The two above-mentioned loading scenarios correspond to Zones 3 and 4, which effectively fail by crushing, as opposed to Zones 1 and 2 that are dominated by cracking failure. (Wight and MacGregor 2012.) Results of Kupfer et al. (1969) suggest that the boundary between Zones 2 and 3 occur when the applied tensile stress is 1/15 parts of the applied compressive stress.

Figure 7 shows the combination of biaxial stresses that lead to failure of concrete, but it does not consider the effect on strains at failure. According to the results of Kupfer et al. (1969), the effect is noteworthy and again depends on the loading



scenario. In Zone 4, the compressive strains at failure in the direction of largest compressive stress are increased as compared to uniaxial compression strain. Triaxial compressive loading yields similar results (Wight and MacGregor 2012), which explains the aforementioned increase of compressive strength and strain at failure of confined concrete in EC2 part 1-1. In Zone 2, both compressive and tensile strains in failure in the loading directions decrease with increasing ratio of tensile stress to compressive stress. In Zone 1, increasing the ratio of smaller tensile stress to the larger one decreases the maximum tensile strain at failure. More detailed results regarding biaxial loading are given in the paper by Kupfer et al. (1969).

The lack of tensile strength in concrete structures is made up by using steel bars or by prestressed tendons. In the scope of this thesis, only reinforced concrete without prestressing is considered. The use of reinforcing bars in tensile regions of concrete structures is based on the fact that the reinforcing bars start carrying the tensile loads initially carried solely by concrete. Typical stress-strain relations for hot rolled and cold worked reinforcing steel are shown in Figure 8 (EC2 part 1-1). In the figure, f_{yk} stands for characteristic yield strength, f_t stands for tensile strength, $f_{0,2k}$ stands for 0.2 % proof stress, and ε_{uk} stands for strain at maximum force. The magnitude of f_{yk} is typically 500 MPa, which is significantly larger than the tensile strength of concrete. Comparing to the highest strength class given in EC2 part 1-1, the mean tensile strength of concrete is 5.0 MPa, which is 100 times smaller than f_{yk} . This means that the tension carrying capability of steel is vastly superior to that of concrete.

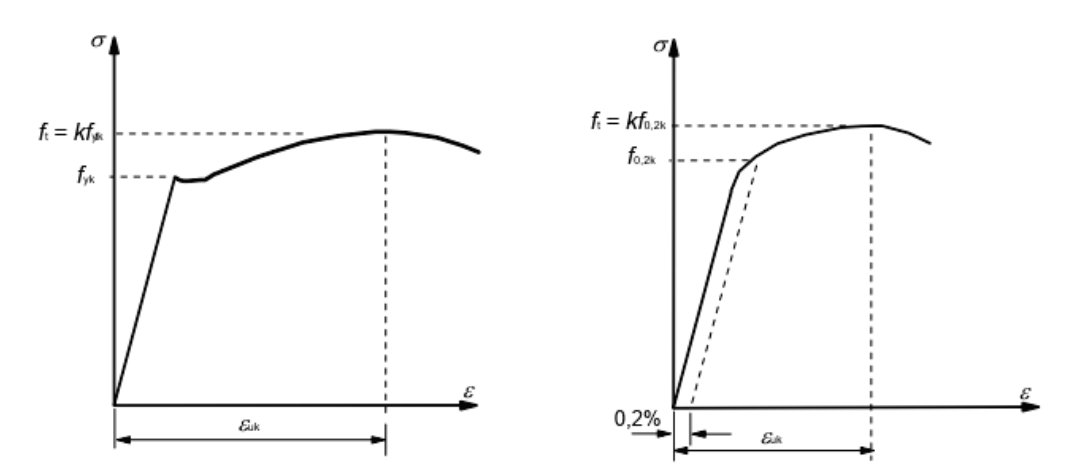


Figure 8. Typical compressive and tensile stress-strain relations of a) hot rolled and b) cold worked reinforcing steel (EC2 part 1-1).

3.3 TEMPERATURE DEPENDENCE OF THERMO-MECHANICAL PROPERTIES

The properties of concrete at elevated temperatures have been researched widely (see e.g. compilation by Naus 2010). Due to the large number of variables affecting the properties of concrete, the studies can yield suggestive results, but the actual behavior of concrete structures can be quite case-specific. These variables include the composition of concrete (cement type, aggregate type, water to cement ratio, etc.), the age, testing conditions (temperature, air humidity) or the size of the



studied structure. The goal of this subsection is to study how the mechanical and thermal properties of reinforced concrete are affected between temperature range of 20 to 65 °C. If the studied properties have negligible differences at this temperature range, the accuracy of the modelling need not be compromised by over-simplifications. The discussion in this section will affect the modelling assumptions and will therefore be important when considering the possible sources of error or inaccuracy post-modelling.

The thermo-mechanical properties of interest include the stress-strain relation, thermal expansion coefficient, thermal conductivity and specific heat. The properties are considered for both concrete and reinforcing bars unless otherwise stated.

Majority of papers related to the mechanical properties of concrete at elevated temperatures tend to study temperatures well above the threshold temperature of 65 °C (see e.g. compilation by Naus 2010). This suggests that the differences at range of 20 to 65 °C are not of interest and therefore small. However, this presumption should be confirmed. The Eurocode design standards define the basis for structural design, and it can therefore be considered a trustworthy source that compiles research results into a generally reliable and usable form. Therefore, parts of Eurocode are used to analyze if the studied properties are temperature dependent instead of relying on individual studies that can have case-specific results as discussed earlier. However, studies or reports compiling number of individual studies may be used for comparison. Eurocode 2 part 1-1 "General rules and rules for buildings" contains little information concerning the temperature dependence of the studied properties, and it is more concentrated on general design values at ambient temperature. However, EC2 part 1-2 "General rules. Structural fire design" contains information at elevated temperatures.

This sub-chapter contains tables that summarize the differences of properties in the studied temperature range. These tables include an estimate of the properties' temperature dependence. The estimate is defined based on the relative difference given in Equation (1).

$$RD = Relative \ difference = \left| \frac{Property \ value \ at \ 65 \, ^{\circ}C}{Property \ value \ at \ 20 \, ^{\circ}C} - 1 \right| \cdot 100\% \tag{1}$$

Equation (1) is then used to determine a verbal value for the dependency. The threshold values and the verbal values, arbitrarily chosen by the author of this thesis, are shown in Table 1.

Table 1. Definition of a property's temperature dependency.

Relative difference, RD [%]	Temperature dependency
$0 \le RD \le 2$	None
$2 < RD \le 10$	Negligible
$10 < RD \le 20$	Moderate
RD > 20	Considerable



3.3.1 Stress and strain characteristics at elevated temperatures

The stress-strain relation of uniaxially compressed concrete used in EC2 part 1-2 is shown in Figure 9. The relation is defined using three parameters:

- the characteristic compressive strength $f_{c,\theta}$,
- strain $\varepsilon_{c1,\theta}$ corresponding to $f_{c,\theta}$, and
- the ultimate compressive strain $\varepsilon_{cu1,\theta}$.

For normal weight concrete made of siliceous or calcareous aggregates, $f_{c,\theta}$ is unaffected by the temperature between 20°C $\leq T \leq$ 100 °C and is equal to the characteristic compressive cylinder strength of concrete at 28 days, f_{ck} . However, $\varepsilon_{c1,\theta}$ increases linearly from 0.25 % to 0.4 % between that temperature range, corresponding to

 $\varepsilon_{c1,\theta}(T=65 \,^{\circ}\text{C}) = 0.334 \,\%$. This results into a considerable difference in tangent elastic modulus at zero strain as shown next. The ascending part of the stress-strain relation in Figure 9 is given in Equation (2).

$$\sigma(\varepsilon) = \frac{3f_{c,\theta} \cdot \varepsilon}{\varepsilon_{c1,\theta} \cdot \left(2 + \left(\frac{\varepsilon}{\varepsilon_{c1,\theta}}\right)^3\right)}$$
 (2)

The tangent elastic modulus at zero strain E_0 can be evaluated from Equation (2) as shown by Equation (3).

$$E_0 = \frac{d\sigma(\varepsilon)}{d\varepsilon} \bigg|_{\varepsilon=0} \tag{3}$$

Using $\varepsilon_{c1,\theta}(T=20\,^{\circ}\text{C})=0.25\,\%$ and $\varepsilon_{c1,\theta}(65\,^{\circ}\text{C})=0.334\,\%$ results into $E_0(20\,^{\circ}\text{C})=600f_{c,\theta}=600f_{ck}$ and $E_0(65\,^{\circ}\text{C})=449f_{c,\theta}=449f_{ck}$. Thus, E_0 decreases by some 25 % between 20 °C and 65 °C with the model given in EC2 part 1-2. For reference, using strength class C30/37 of EC2 part 1-1 with $f_{ck}=30\,$ MPa and secant elastic modulus of $E_{cm}=33\,$ GPa, the initial elastic modulus at 20 °C and 65 °C gets values of $E_0(20\,^{\circ}\text{C})=18\,$ GPa and $E_0(65\,^{\circ}\text{C})\approx13.5\,$ GPa. Both of these values are significantly lower than the secant elastic modulus. This is unintuitive as the stress-strain relation of concrete generally has decreasing gradient with increasing strain, meaning that the secant elastic modulus should be smaller than initial elastic modulus.



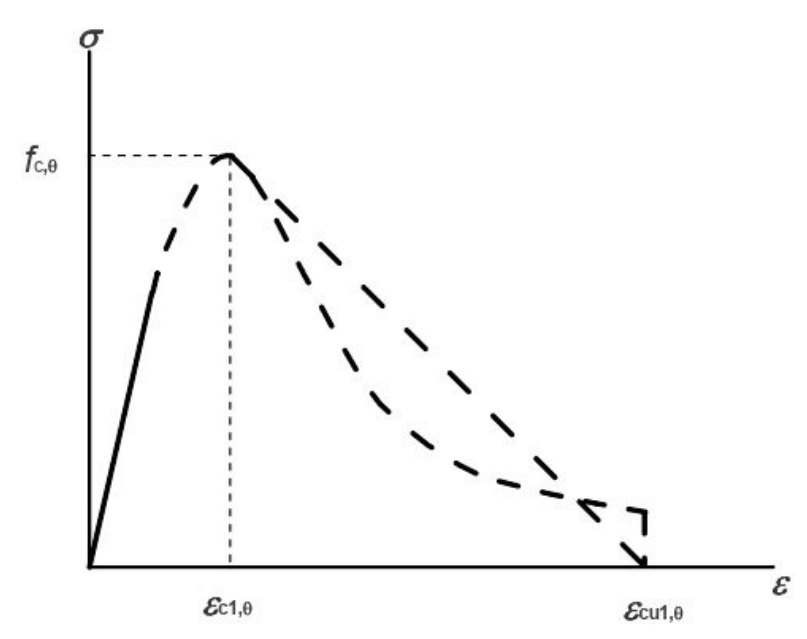


Figure 9. Uniaxial compressive stress-strain relation of EC2 part 1-2.

It is noteworthy that EC2 part 3 "Liquid retaining and containment structures" considers the temperature dependence of the modulus of elasticity of concrete directly in its Annex K. Annex K.3 clause (102) states the following: "The modulus of elasticity of concrete may be assumed to be unaffected by temperature up to 50 °C. For higher temperatures, a linear reduction in modulus of elasticity may be assumed up to a reduction of 20 % at a temperature of 200 °C". At 65 °C, the modulus of elasticity is 98 % of that at 20 °C using the above rule. This differs significantly from the value derived using the stress-strain relation of EC2 part 1-2. However, it should be considered that the scopes of these Eurocode parts differ from each other and thus the material models and calculation methods can also differ. Nonetheless, the differences between the parts are considerable and they illustrate the uncertainty of using strict values when considering concrete structures.

The ultimate strain $\varepsilon_{cu1,\theta}$ increases from 2 % to 2.25 % between the temperature range of 20 °C $\leq T \leq$ 100 °C, according to EC2 part 1-2. This corresponds to $\varepsilon_{cu1,\theta}(65 \, ^{\circ}\text{C}) = 2.14 \, \%$. The material model of EC2 part 1-2 does not require changes to the characteristic tensile strength of concrete between 20°C $\leq T \leq$ 100 °C , and it does not consider the tensile strain values directly. The lack of tensile stress and strain values compared to those of compressive can likely be explained by the fact that the tensile strength of concrete does not have a significant role in fire design. However, in uniaxial stress-strain relationship, the initial modulus of elasticity is of similar magnitude in compression and tension as shown in Figure 6. This would suggest, if using the model of EC2 part 1-2, that the tensile strain corresponding to characteristic tensile strength should increase, because the elastic modulus is decreasing.



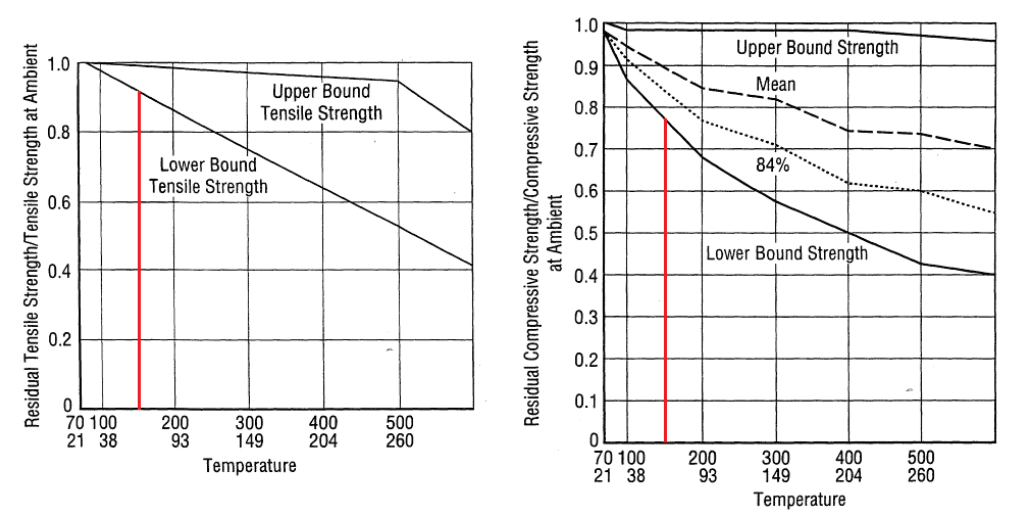


Figure 10. Residual tensile and compressive strengths of concrete at elevated temperatures. The red line indicates temperature of 65 °C. (Modified from Kassir, Bandyopadhyay and Reich (1996).)

For comparison, a report from Kassir, Bandyopadhyay and Reich (1996) compiled plots shown in Figure 10 for the ratios of residual compressive and tensile strengths at elevated temperatures to reference values at ambient temperature. The report is based on a test database involving different concrete mixes and testing conditions, and thus the results can only be regarded as suggestive. The figure shows that the scatter between upper and lower bound is larger for compressive strength. At 65 °C the lower and upper bounds range roughly between 0.9 to 0.99 and 0.77 to 0.99 for tensile and compressive strengths, respectively. Similar plot for the elastic modulus is given in Figure 11. The figure shows that the elastic modulus at 65 °C has upper and lower bound ratios of 0.7 and 0.98 compared to that at ambient temperature. These values fall into the range EC2 part 1-2 and EC2 part 3. A summary of the temperature dependence of stress-strain related values of concrete is shown in Table 2.

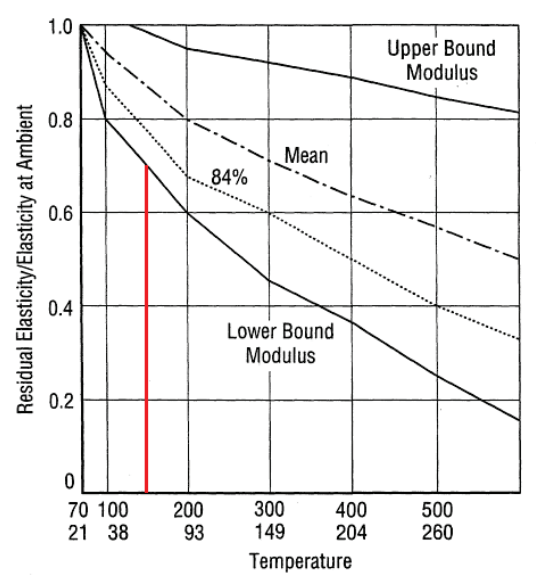


Figure 11. Residual elastic modulus of concrete at elevated temperatures. The red line indicates temperature of 65 °C. (Modified from Kassir, Bandyopadhyay and Reich (1996).)



For reinforcing bars, EC2 part 1-1 does not directly give the temperature range at which the design according to it can be performed. As for concrete, EC2 part 1-2 yields a temperature dependent stress-strain relation for reinforcement. However, between 20 °C to 100 °C the temperature dependence of strength properties of reinforcing steel is none or negligible. Elghazouli, Cashell and Izzuddin (2009) compared the stress-strain model of EC2 part 1-2 for reinforcing steel to experimental tests with small diameter bars. Between 20 °C to 100 °C the experiments and the stress-strain model were in line with each other showing no major differences. Hence, it can be assumed that the strength properties of reinforcing steel are independent of temperature between 20 °C to 65 °C.

Table 2. Summary of temperature dependence of stress-strain relation related values of concrete. Bolded values are reference values normalized to 1.

Property	Value at 20 °C	Value at 65 °C	Temperature dependency
Compressive strength			
 EC2 part 1-2 	f_{ck}	$f_{\it ck}$	None
 Figure 10 	1	0.77 to 0.99	Considerable to none
Tensile strength			
 EC2 part 1-2 	$f_{ck,t}$	$f_{\mathit{ck},t}$	None
• Figure 10	1	0.9 to 0.99	Negligible to none
Compressive strain corresponding to compressive strength (EC2 part 1-2)	0.25 %	0.334 %	Considerable
Ultimate compressive strain (EC2 part 1-2)	2 %	2.14 %	Negligible
Elastic modulus			
 EC2 part 1-2* 	$600f_{ck}$	$449f_{ck}$	Considerable
 EC2 part 3 	= 18 GPa	= 13.5 GPa	None
• Figure 11	1 1	0.98 0.7 to 0.98	Considerable to none

^{*}Derived from stress-strain relation, not directly given. Absolute values are computed for strength class C30/37 of EC2 part 1-1.

3.3.2 Thermal properties at elevated temperatures

The coefficient of thermal expansion, α , describes how a solid body expands or contracts due to temperature differences. As will be shown later, the magnitude of α will affect the stress state due to thermal loads, and therefore its temperature dependency should be studied. According to Naik, Kraus and Kumar (2011), typically some 75 % of concrete volume constitutes of coarse aggregates, and therefore the magnitude of the coefficient of thermal expansion of concrete is mainly affected by that of the used coarse aggregate. EC2 part 1-2 yields thermal strain of concrete as a function of temperature separately for concretes constituting of siliceous or calcareous aggregates. The thermal strain of concrete according to EC2 part 1-2 for siliceous and calcareous aggregates are respectively given in Equations (4) and (5).

$$\varepsilon_{cs}(T) = -1.8 \cdot 10^{-4} + 9 \cdot 10^{-6} \cdot T + 2.3 \cdot 10^{-11} \cdot T^3$$
 (4)



where 20 °C \leq T \leq 700 °C and

$$\varepsilon_{c,c}(T) = -1.2 \cdot 10^{-4} + 6 \cdot 10^{-6} \cdot T + 1.4 \cdot 10^{-11} \cdot T^3$$
 (5)

where 20 °C \leq T \leq 805 °C.

Differentiating Equations (4) and (5) with respect to *T* yield coefficients of thermal expansion given in Equations (6) and (7) with temperature ranges according to those of Equations (4) and (5).

$$\alpha_{c.s} = \frac{d\varepsilon_{c.s}(T)}{dT} = 9 \cdot 10^{-6} + 6.9 \cdot 10^{-11} \cdot T^2$$
 (6)

and

$$\alpha_{c.c} = \frac{d\varepsilon_{c.c}(T)}{dT} = 6 \cdot 10^{-6} + 4.2 \cdot 10^{-11} \cdot T^2$$
 (7)

EC2 part 1-2 also yields the thermal strain of reinforcing steel. With similar procedure, the coefficient of thermal expansion of reinforcing steel, α_s , is given in Equation (8) with a temperature range of 20 °C \leq T \leq 750 °C.

$$\alpha_s = 1.2 \cdot 10^{-5} + 0.8 \cdot 10^{-8} \cdot T \tag{8}$$

The values for $\alpha_{c.s}$, $\alpha_{c.c}$ and α_s at 20 °C and 65 °C are shown in Table 3. The table shows that the coefficients of thermal expansion have negligible temperature dependency. However, the difference in values of concrete made with the two aggregate types is considerable. For modelling, the coefficient of thermal expansion should therefore be chosen carefully to describe the actual structure as its value is directly proportional to the magnitude of thermal loads. Furthermore, the difference in the values for reinforcing steel and concrete is noticeable as α_s is over two times larger than $\alpha_{c.c}$ and over 33 % larger than $\alpha_{c.s}$. This will be a source of error if the coefficient of thermal expansion is assumed equal between concrete and reinforcement. However, a in study by Vodak et al. (1997) measurements of the concrete used in French Penly NPP concluded that the coefficient of thermal expansion of concrete is some $11 \cdot 10^{-6}$ °C⁻¹ and $12.3 \cdot 10^{-6}$ °C⁻¹ at 20 °C and 65 °C, respectively. The studied concrete was regarded siliceous according to the study. These values are closer to those of α_s , but differ from those of $\alpha_{c.s}$ or $\alpha_{c.c}$.

Table 3. Coefficients of thermal expansion of concrete and reinforcing steel.

Material	Value at 20 °C [°C ⁻¹]	Value at $65 ^{\circ}\text{C}$ $[^{\circ}\text{C}^{-1}]$	Temperature dependency
Concrete • Siliceous ($\alpha_{c.s}$, Eq. (6)) • Silicieous (Vodak et al. 1997) • Calcareous ($\alpha_{c.c}$, Eq. (7))	$9.03 \cdot 10^{-6}$ $11 \cdot 10^{-6}$ $6.02 \cdot 10^{-6}$	$9.29 \cdot 10^{-6}$ $12.3 \cdot 10^{-6}$ $6.18 \cdot 10^{-6}$	Negligible Moderate Negligible
Reinforcing steel (α_s , Eq. (8))	$12.16 \cdot 10^{-6}$	$12.52 \cdot 10^{-6}$	Negligible

Concerning heat transfer by conduction in solids, the thermal conductivity (λ) and thermal diffusivity (D) are important measures. Thermal conductivity has units of



 $W/(m \cdot K)$ and the thermal diffusivity has units of m^2/s . The thermal diffusivity is defined in Equation (9).

$$D = \frac{\lambda}{\rho \cdot c_p} \tag{9}$$

where

 ρ is the density of the material $[kg \cdot m^{-3}]$ and c_p is the specific heat of the material of $[J \cdot (kg \cdot {}^{\circ}C)^{-1}]$.

Before diving into the mathematics concerning heat transfer by conduction in solids, let us study the temperature dependency of thermal conductivity, density and specific heat of concrete. Relevant mathematics are discussed in Part 3.4.1. The reinforcement is not discussed, as the ratio of reinforcement area to concrete area in a typical cross-section in the reactor building is some 0.15 % per section face. Therefore, the effect of reinforcement in heat transfer is assumed to be negligible in the temperature range of 20 °C and 65 °C.

According to EC2 part 1-2, only the thermal conductivity is non-constant between the studied temperature range. For 20 °C $\leq T \leq$ 1 200 °C It is given as lower and upper limit that are respectively given in Equations (10) and (11).

$$\lambda_{c.l} = 1.36 - 0.136 \cdot \left(\frac{T}{100}\right) + 0.0057 \cdot \left(\frac{T}{100}\right)^2 \quad \left(\frac{W}{m \cdot K}\right)$$
 (10)

and

$$\lambda_{c.u} = 2 - 0.2451 \cdot \left(\frac{T}{100}\right) + 0.0107 \cdot \left(\frac{T}{100}\right)^2 \quad \left(\frac{W}{m \cdot K}\right)$$
 (11)

Evaluating Equations (10) and (11) at T = 20 °C and T = 65 °C yields the results given in Table 4. The table shows that the thermal conductivity tends to decrease with temperature, but between studied temperatures, the differences for each limit are small. As with coefficient of thermal expansion, it is more important to choose a value that describes the actual structure as the lower and upper limits differ from each other notably. In the study of Vodak et al. (1997), the conductivity decreased linearly with increasing temperature, and the results suggest conductivities of $2.24 \ W/(m \cdot K)$ and $2.16 \ W/(m \cdot K)$ at 30 °C and 65 °C, respectively. Extrapolating to 20 °C yields $2.26 \ W/(m \cdot K)$. As Table 4 indicates, the temperature dependency is similar, but the upper limit of EC2 part 1-2 is exceeded.

Table 4. Thermal conductivity of concrete.

Limit	Value at $20 ^{\circ}$ C $[W/(m \cdot K)]$	Value at 65 °C $[W/(m \cdot K)]$	Temperature dependency
Lower ($\lambda_{c,l}$, Eq. (10))	1.33	1.27	Negligible
Upper ($\lambda_{c,u}$, Eq. (11))	1.95	1.84	Negligible
Vodak et al. (1997)	2.26	2.16	Negligible

The specific heat describes the heat energy needed to increase the temperature of one kilogram of material with one degree Celsius. According to Schneider (1988), the aggregate type does not affect the specific heat at low temperatures. However,



the water content in the concrete affects the specific heat considerably at temperatures lower than 200 °C. At 100 °C the vaporization of free water will result into a sudden increase in specific heat as the model of EC2 part 1-2 shows. In temperatures below 100 °C EC2 part 1-2 suggests a constant value of $c_p = 900 \, J \cdot (kg \cdot {}^{\circ}C)^{-1}$ for dry concrete made of siliceous or calcareous aggregates. For comparison, Vodak et al. (1997) reported experimental values of some 750 $J \cdot (kg \cdot {}^{\circ}C)^{-1}$ and 770 $J \cdot (kg \cdot {}^{\circ}C)^{-1}$ between 20 °C and 65 °C. Table 5 summarizes the results for the specific heat of concrete.

Table 5. The specific heat of concrete.

Limit	Value at 20 °C	Value at 65 °C	Temperature
	$[J \cdot (kg \cdot {}^{\circ}C)^{-1}]$	$[J \cdot (kg \cdot {}^{\circ}C)^{-1}]$	dependency
EC2 part 1-2	900	900	None
Vodak et al. (1997)	750	770	Negligible

Finally, the temperature dependency of density of concrete is covered. The density changes with respect to temperature are linked to the evaporation of water in concrete and the thermal expansion (EC2 part 1-2). In a model from EC2 part 1-2, the density of concrete is assumed to be constant in the temperature range from 20 °C and 115 °C, after which it decreases.

Tables 2 to 5 summarize the temperature dependency of concrete and reinforcing steel for properties relevant in the scope of this thesis. As discussed earlier, the properties of concrete can be quite case-specific which is related to differences in the concrete mixture (e.g. aggregate and cement type, water-to-cement ratio), testing methods and testing conditions. Therefore, the temperature dependencies given in these tables should be considered as suggestive results. Using the relative difference based classification defined in Equation (1) and Table 1, compressive strength, compressive strain corresponding to compressive strength, and the elastic modulus of concrete showed signs of considerable temperature-dependency between 20 °C and 65 °C. However, the compressive strength and the elastic modulus also had results or models that suggested that there was no temperaturedependency at all. The thermal properties of concrete showed mostly no or negligible temperature-dependency in the studied temperature range. The magnitudes of thermal properties did however show considerable discrepancy, suggesting that weight should be given to the determination of thermal properties that represent the actual structure when entering the modelling phase.

3.4 THERMAL LOADS

According to EN 1991-1-5 "General actions. Thermal actions", the temperature distribution of a structural element can be presented as a sum of four basic components. This is illustrated in Figure 12.



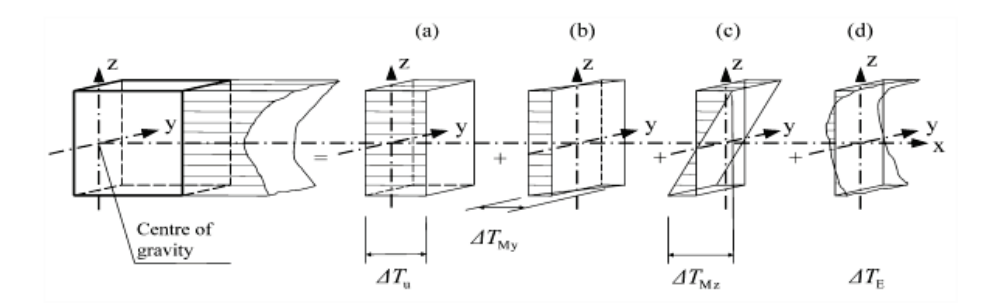


Figure 12. Dividing a temperature distribution to a) a constant linear, b,c) a linearly varying and d) a non-linearly varying component (EC1 part 1-5).

As shown by Figure 12, the temperature distribution can be divided into a constant linear, two linearly varying and to a nonlinearly varying component. These components induce a thermal strain, ε_T , according to Equation (12).

$$\varepsilon_T = \alpha \Delta T$$
 (12)

where α is the coefficient of thermal expansion of the material [°C⁻¹] ΔT is the change of temperature from a reference temperature [°C].

Thermal loads are loads induced by the difference between realized strain, ε , and the thermal strain of a body. In other words, when $\varepsilon - \varepsilon_T \neq 0$, a thermal load is induced. According to Thurston (1978) thermal loads in reinforced concrete structures can be induced for example by

- 1. nonlinear temperature distributions,
- 2. temperature changes of statically indeterminate structures or
- 3. the incompatibility of reinforcing steel and concrete
- 4. incompatibility between the constituents of concrete.

In this thesis, Items 3 and 4 are assumed negligible which effectively means that the coefficients of thermal expansion are assumed to be the same for the average of concrete constituents and reinforcing steels. A stress state induced by Item 1 is known as a primary thermal stress, and a stress state induced by Item 2 is known as a continuity thermal stress (Vecchio 1987). From here on in, the two types of thermal stresses are used without the word "thermal" for simplicity.

3.4.1 Primary stresses

Primary stresses can be induced to any solid body regardless of the boundary conditions of the body. According to El-Badry and Ghali (1995) this can be explained by the inability of material fibers to freely expand (or contract) as they are monolithically attached to adjacent fibers. Therefore, when nonlinear temperature strain is present a thermal load is induced. This is illustrated in Figure 13 for an unrestrained beam that is free to deform. The figure shows a nonlinear temperature distribution over the beam section. When the thermal strain exceeds the realized section strain, i.e. $\varepsilon_T - \varepsilon > 0$, a compressive stress is induced into the material. This is because the material tends to push against the realized strain. While $\varepsilon_T - \varepsilon < 0$, a tensile stress is induced as the body tries to pull the material



towards the actual strain. Characteristic for primary stresses is that they are self-equilibrating meaning the net reaction forces caused by them are zero if the structure is statically determinate (El-Badry and Ghali 1986). This is illustrated in Figure 13 with the sums of forces and moments being zero, i.e. $\Sigma P = 0$ and $\Sigma M = 0$.

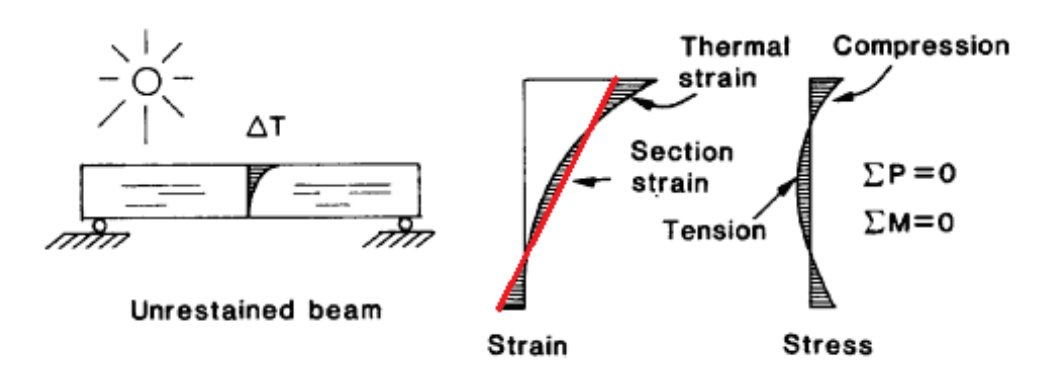


Figure 13. The effect of nonlinear temperature gradient in an unrestrained beam (Vecchio 1987). The red line represents the realized section strain.

El-Badry and Ghali (1986) investigated the thermal loads in concrete structures, concentrating on bridges. In their work, the primary stress, $\sigma_{T.p}$, for a cross-section where temperature varies in one coordinate direction (here variable y is used) is given by Equation (13), which through Equations (14) to (17), assumes that the structure is statically determinate and that only a thermal load is present. If other loads are present, they are to be added to Equations (15) and (16) (El-Badry and Ghali 1995).

$$\sigma_{T,p}(y) = E[\varepsilon_0 + \psi y - \alpha \Delta T(y)] \tag{13}$$

where

E is the modulus of elasticity

 $\Delta T(y)$ is the temperature difference at coordinate y $\varepsilon = \varepsilon_0 + \psi y$ is the actual strain distribution with ε_0 and ψ being the constant term and the slope given in Equations (14) and (15).

$$\varepsilon_0 = \frac{-N}{EA} \tag{14}$$

$$\psi = \frac{-M}{EI} \tag{15}$$

where

A and *I* are the section area and second moments of area through section centroid, respectively

N and *M* are normal force and bending moment given in Equations (16) and (17), respectively.

$$N = -E\alpha \int \Delta T(y) \, dA \tag{16}$$



$$M = -E\alpha \int \Delta T(y) y \, dA \tag{17}$$

where $d\mathbf{A}$ is an area element. Rewriting Equation (13) with Equations (14) to (17) yields Equation (18) which shows that the magnitude of primary stresses is directly proportional to the modulus of elasticity and the coefficient of thermal expansion. This magnifies the importance regarding them discussed in Part 3.3.

$$\sigma_{T,p}(y) = E\alpha \left[\frac{1}{A} \int \Delta T(y) \, dA + \frac{y}{I} \int \Delta T(y) y \, dA - \Delta T(y) \right] \tag{18}$$

Equations (13) through (15) are well known and also given in a more general form e.g. in another work by El-Badry and Ghali (1995). Although their work focused on bridge-like structures (both statically determinate and indeterminate), the principle governing primary stresses is similar for walls and floors. However, the realized strain of a wall or floor section is different due to the different boundary conditions.

A nonlinear temperature distribution could occur in the studied reactor building during a ramp-up or a ramp-down of a maintenance overhaul, as discussed in Part 2.3. During overhauls, room air temperatures can vary quickly, and due to a relatively low thermal conductivity of concrete, the thermal equilibrium (i.e. linear temperature distribution) of concrete walls and floors will take time to develop. The time to develop equilibrium is hypothetically increased with thick walls or floors.

Vecchio and Sato (1990) studied the thermal gradient effect in reinforced concrete frames with experiments. With a temperature difference of 73 °C (range of 18...91 °C) between the surfaces of a 300 mm thick concrete frame, tensile stresses of some 4 MPa were achieved exceeding tensile strength of typical concrete. In the specific case, primary stresses were the only load in the frame, the heating of the warmer surface was performed with water, and relevant properties of concrete were an elastic modulus of 30 GPa and a coefficient of thermal expansion of 12.1 \cdot 10^{-6} °C⁻¹. The study suggests that primary stresses can alone cause cracking and if quick temperature changes in concrete occur, they should be considered in design.

When considering the primary stresses, the temperature field of a body at a given time is of interest as it can be used to measure the nonlinearity of the temperature distribution. The development of temperature field of a body can be described with heat conduction equation. According to Santaoja (2014), heat conduction equation can be written as shown by Equation (19). The heat conduction equation can be derived from the law of conservation of energy and the Fourier's law of heat conduction (Thirumaleshwar 2006).

$$\rho c_p \dot{T} = \rho r + \nabla \cdot (\lambda(T) \nabla T) \tag{19}$$

where

 ρ is the density of the material $[kg \cdot m^{-3}]$ \dot{T} is the time derivative of temperature field T(t,x,y,z) [°C/s] r is heat source per unit time and mass $[J \cdot (kg \cdot s)^{-1}]$ or $[W \cdot kg^{-1}]$ ∇ is the gradient operator $(\nabla = \left(\frac{\partial}{\partial x} \mathbf{i} + \frac{\partial}{\partial y} \mathbf{j} + \frac{\partial}{\partial z} \mathbf{k}\right)$ in Cartesian coordinates.



Let us assume that thermal conductivity, λ , is not a function of the temperature, which is a fair assumption as per results shown in Table 4. Let us also assume that thermal conductivity behaves isotropically, i.e. it is constant and equal in each coordinate direction. Then Equation (19) can be written in forms shown by Equations (20), (21) and (22).

$$\rho c_p \dot{T} = \rho r + \lambda (\nabla \cdot \nabla T) \tag{20}$$

$$\rho c_p \frac{\partial T}{\partial t} = \rho r + \lambda \left(\frac{\partial^2 T}{\partial x^2} + \frac{\partial^2 T}{\partial y^2} + \frac{\partial^2 T}{\partial z^2} \right) \tag{21}$$

$$\frac{\partial T}{\partial t} = \frac{r}{c_p} + \frac{\lambda}{\rho c_p} \left(\frac{\partial^2 T}{\partial x^2} + \frac{\partial^2 T}{\partial y^2} + \frac{\partial^2 T}{\partial z^2} \right). \tag{22}$$

In Equation (22), quotient $\lambda \cdot (\rho c_p)^{-1}$ is the thermal diffusivity of the material as shown by Equation (9). According to Thirumaleshwar (2006), thermal diffusivity can be regarded as a material's ability to find the thermal equilibrium in the sense that materials with higher thermal diffusivity find the thermal equilibrium faster. In other words, materials with high thermal diffusivity can transfer heat into the material faster. The thermal diffusivity of concrete is relatively low, which means that it responds to temperature changes quite slowly. This was illustrated in Figure 5. No internal heat source is present in the problem at hand, thus the term r/c_p in Equation (22) can be omitted.

3.4.2 Continuity stresses

Continuity stresses are induced in statically indeterminate structures with temperature changes. As the temperature changes and the structure tries to deform, the supporting forces tend to restrain these deformations, thus causing a state of stress. As with primary stresses, the principal mechanism behind continuity stresses is the difference between the realized strains and the free thermal strains of a body. Even constant temperature gradients, such as those in Figure 12a-c, are enough to induce a stress state in a body if the structure is statically indeterminate.

By definition, continuity stresses are dependent on the boundary conditions and the geometry of the structure. Analytical solutions for continuity stresses have been developed for beam and frame structures, although they can over-simplify the problem or be overly complicated as discussed by Vecchio (1987). In beam or frame structures, the number of supports is finite as opposed to continuous support reactions in the studied reactor building. A hypothesis is made that the stress state induced by continuity stresses is localized to the volume near the intersection of adjacent structural pieces. Therefore, no effort to find analytical solutions for continuity stresses is given as the problem is too complex and localized. However, an example on the relation between temperature difference and accompanied stress state can be given as follows:



Assume a concrete body with properties according to EC2 part 1-1:

• coefficient of thermal expansion $\alpha = 10^{-5} \, {}^{\circ}\text{C}^{-1}$

• mean tensile strength for class C40/50 $f_{ctm} = 3.5 MPa$

elastic modulus for class C40/50 $E_{cm} = 35 GP$

From Hooke's law, the strain corresponding to tensile strength is given in Equation (23) as

$$\varepsilon_t = \frac{f_{ctm}}{E_{cm}} = \frac{3.5 \, MPa}{35 \, GPa} = 10^{-4} \tag{23}$$

According to Equation (12), the temperature difference compared to the reference temperature for thermal strains, needed to induce a thermal strain equal to that of Equation (23) is given in Equation (24).

$$\Delta T = \frac{\varepsilon_t}{\alpha} = \frac{10^{-4}}{10^{-5} \, {}^{\circ}\text{C}^{-1}} = 10 \, {}^{\circ}\text{C}$$
 (24)

If the concrete body subjected to a temperature difference of $\Delta T = 10$ °C is fully restrained from deformations, the continuity stresses could cause tensile stresses equal to tensile strength resulting into initiation of cracking.

3.4.3 Total thermal stresses

The total thermal stress affecting a body is the sum or primary and continuity stresses. One of the goals in the modelling phase is to estimate the severity of primary stresses in comparison with the continuity stresses. An estimate can be made by comparing the results from the two following modelling methods with same topology:

- 1. a linear temperature distribution is assumed between wall or floor surfaces where thermal equilibrium is already attained
- 2. a three-dimensional heat transfer model coupled with static structural analysis is performed where thermal equilibrium forms with time.

Here, Item 1 returns the response to continuity stresses alone, whereas Item 2 returns the response to total thermal stresses. By comparing the results, the severity of primary stresses can be evaluated and compared with continuity stresses.

Thurston (1978) states that in bridge-like structures the magnitudes of continuity stresses are usually larger than those of primary stresses. Intuitively, this holds also for monolithic buildings such as the reactor building. However, knowing the severity of both continuity and thermal stresses is important for the following reasons. The magnitude of continuity stresses yields information on the temperature differentials the structure can withstand, whereas primary stresses consider the importance of developing rate of room temperature differentials. As discussed in Part 3.1, cracking reduces the stiffness of concrete structures. As the thermal stresses are function of the elastic modulus, the magnitudes of thermal



stresses tend to decrease with cracking. Furthermore, the elastic modulus is decreased by the creep effect which is discussed next.

3.5 CONCRETE CREEP

Creep effect is a mechanism where strain increases under constant stress. If the strain is held constant, the stresses tend to decrease for materials that exhibit creep. This is known as relaxation. The mechanism behind concrete creep ultimately lies in the atomic bond formations and breakages in the silicate hydrate gels of the cement paste. (Bazant and Jirasek 2018.) Here, the mechanism and reasons behind creep are not covered further. However, the effect of creep on the structural stiffness and therefore to the magnitudes of thermal loads is shortly discussed with its temperature dependence.

In serviceability limit state according to EC2 part 1-1, the effect of creep is considered by an effective modulus of elasticity of concrete, given in Equation (25). According to EC2 part 1-1, creep is a function of ambient humidity, dimensions of the structure and composition of concrete. Creep is also a history-dependent property, as the age at which the concrete was loaded and the overall load history affect the magnitude of creep.

$$E_{c,eff} = \frac{E_{cm}}{1 + \varphi(\infty, t_0)} \tag{25}$$

where

 E_{cm} is the secant elastic modulus of concrete [GPa] $\varphi(\infty, t_0)$ is the final value of creep coefficient loaded at age t_0 [-] given by Annex B of EC2 part 1-1.

Equation (25) effectively assumes that the load history of the structure consists of only one step which in many cases is untrue. The error of considering creep effects by means of Equation (25) can be large for structures loaded at early age having a long response under the load. (Bazant and Jirasek 2018.) However, it is endorsed by Eurocodes and it is valid for typical structures. In monolithic buildings, the strains are restrained at intersections of adjacent structural pieces and thus the relaxation may also occur. This supports the use of effective elastic modulus to avoid the overestimation of thermal stresses.

As the value of $\varphi(\infty, t_0)$ is positive, $E_{c,eff}$ is smaller or equal to E_{cm} as shown by Equation (25). Usually, the creep coefficient $\varphi(\infty, t_0)$ is also larger than one, meaning that $E_{c,eff}$ is often less than half of E_{cm} . As mentioned earlier and as shown, for example, by Equation (18), the magnitudes of thermal stresses are proportional to the magnitude of elastic modulus of concrete. Thus, the creep effect has a favorable effect when considering only the magnitude of thermal stresses.

The rate of creep development is significantly increased even with low temperature increments. Already at temperature of 32 °C creep is significantly increased plateauing at some 70 °C. (Wright and MacGregor 2012.) Many of the rooms in the reactor building are between these temperatures, and thus the creep effect should be considered. One of the goals in the modelling phase is to estimate the effect of creep on the structural response to thermal loads.



4 Finite element modelling

4.1 GENERAL INFORMATION

To study the sub-problems introduced in Chapter 1, numerical modelling in terms of FEM is used. Commercial FEM software Ansys is used for its versatility and as it also contains material models for reinforced concrete.

Modelling the behavior of reinforced concrete structures realistically is difficult as it requires the use of multiple materials and as the failure mechanisms and criteria can be complex as described in Part 3.1. Using more than one material demands that the interaction between the materials is defined so that it describes the behavior realistically. The material models need to be well defined to consider the nonlinear effects such as tensile or compressive yielding criteria or post-cracking behavior so that they fit the problem at hand. Furthermore, the complexity is increased if the size of the structure under concern is large, as is with the reactor building.

This chapter first describes the modelling goals after which the principles governing the global modelling are discussed. Then, the global modelling results are introduced and discussed. Based on the results, estimates of the crack widths are also given.

4.2 MODELLING GOALS

The modelling phase has four goals listed as follows:

- 1. estimate possible crack widths considering structural loads relevant in normal operations and at room temperatures of 65 °C or less,
- 2. study the level of thermal loads compared to mechanical, structural loads,
- study the level of primary thermal loads compared to continuity thermal loads,
- 4. study the effect of concrete creep to the structural response to thermal loading.

The goals are tackled by combining global and local modelling. Global modelling is performed in the scale of the whole reactor building using shell elements to represent reinforced concrete walls and floors. The reinforcement is considered as rebar layers in shell elements. A linear temperature distribution through the thickness of walls and floors is assumed, and thus primary stresses are not considered. This assumption is reasonable as the magnitude of continuity stresses are assumed to be greater. In addition to thermal loading, the global model includes a basic structural load combination and the self-weight of the structure. The results of global modelling are used to find hotspots for local modelling and to estimate the global behavior of the reactor building.

In local modelling solid elements are used to represent walls and floors, and the reinforcing bars are modelled discretely into the models. Furthermore, the topology in local modelling contains only a sub-section (certain room with nearby surroundings) of the reactor building to keep computational time reasonable. The sub-section is chosen in accordance with the results of global modelling. With solid elements the local behavior near the intersection of structural pieces can be modelled with better precision than by global modelling. To capture the different



thermal loads, a transient heat analysis coupled with structural analysis is performed. With transient heat analysis, thermal equilibrium is developed with time and the nonlinear behavior of temperature can be considered. The mechanical loads are not considered in the local models for reasons explained in Part 5.2. However, the magnitudes of thermal stresses or cracking from global and local models can be compared to each other.

4.2.1 Goal 1

The crack widths are estimated by using the analytical method given in EC2 part 1-1. This method is presented in Annex 1.

4.2.2 Goal 2

The level of thermal loads can be best compared by using the global model as it contains both mechanical loads and thermal loads. The level is measured in terms of maximum principal plastic strain, ε_{p1} , and maximum principal stress, σ_1 , that are defined in Equations (26) and (27), respectively (Ansys 2020). Due to nonlinear effects, simply calculating ratios of mechanical stresses to thermal stresses is not meaningful which is why plastic strains are also to be considered.

$$\begin{vmatrix} \varepsilon_{p,xx} - \varepsilon_p & \frac{1}{2}\varepsilon_{p,xy} & \frac{1}{2}\varepsilon_{p,xz} \\ \frac{1}{2}\varepsilon_{p,xy} & \varepsilon_{p,yy} - \varepsilon_p & \frac{1}{2}\varepsilon_{p,yz} \\ \frac{1}{2}\varepsilon_{p,xz} & \frac{1}{2}\varepsilon_{p,yz} & \varepsilon_{p,zz} - \varepsilon_p \end{vmatrix} = 0$$
 (26)

where

"| |" denotes determinant of a matrix $\varepsilon_{p.ij}$, i,j=x,y,z are the plastic strain components ε_p denotes the three roots of the principal plastic strain $(\varepsilon_{p1},\varepsilon_{p2})$ and ε_{p3}) ε_{p1} is the maximum of the three roots ε_p .

$$\begin{vmatrix} \sigma_{xx} - \sigma & \sigma_{xy} & \sigma_{xz} \\ \sigma_{xy} & \sigma_{yy} - \sigma & \sigma_{yz} \\ \sigma_{xz} & \sigma_{yz} & \sigma_{zz} - \sigma \end{vmatrix} = 0$$
 (27)

where

 σ_{ij} , i,j=x,y,z are the stress components σ denotes the three roots of the principal stress (σ_1 , σ_2 and σ_3) σ_1 is the maximum of the three roots σ .

4.2.3 Goal 3

Goal 3 is performed by using the local models by first performing a transient thermal analysis where the room temperatures are considered by convection boundary conditions which allows for the development of temperature distribution with time. The time scale is chosen so that the temperature distribution develops to or near to the thermal equilibrium. Then, the temperature fields from multiple time steps are applied to static structural analyzes and maximum principal plastic strains, maximum principal stresses and stresses in the reinforcement are retrieved for each applied time step. These results can then be



compared to an analysis, where the temperature boundary conditions are applied in a state where thermal equilibrium is achieved. The modelling principles are discussed in more detail in Part 5.2.

4.2.4 Goal 4

Goal 4 is performed similarly to Goal 3, but by using a modified modulus of elasticity for concrete to account for creep.

4.3 **MATERIAL MODEL AND PARAMETERS**

Ansys material model library contains ready-made material models that can be used to model concrete-like materials. To keep the models simple while still considering the nonlinear effects, "Drucker-Prager Concrete" material model is used. According to Ansys documentation (2020), the tension and tensioncompression yield surface f_{DP_t} and the compression yield surface f_{DP_c} of the Drucker-Prager concrete model are given by Equations (28) through (35). A more detailed overview is available on Ansys manual (2020). Note that Ansys contains other Drucker-Prager based models that have different yield surfaces, yield criteria and parameters as compared to the Drucker Prager Concrete used here.

$$f_{DP_t} = \frac{\sigma_e}{\sqrt{3}} + \beta_t \sigma_m - \sigma_{Yt}$$
 (28)

$$f_{DP_c} = \frac{\sigma_e}{\sqrt{3}} + \beta_c \sigma_m - \sigma_{Yc} \Omega_c \tag{29}$$

$$\beta_t = \frac{\sqrt{3}(R_c \Omega_c - R_t \Omega_t)}{R_c \Omega_c + R_t \Omega_t}$$
(30)

$$\sigma_{Yt} = \frac{2R_c \Omega_c R_t \Omega_t}{\sqrt{3}(R_c \Omega_c + R_t \Omega_t)} \tag{31}$$

$$\beta_c = \frac{\sqrt{3}(R_b - R_c)}{2R_b - R_c}$$
 (32)

$$\sigma_{Yc} = \frac{R_b R_c}{\sqrt{3}(2R_b - R_c)} \tag{33}$$

$$\sigma_e = \sqrt{3J_2} \tag{34}$$

$$\sigma_m = \frac{\sigma_{11} + \sigma_{22} + \sigma_{33}}{3} \tag{35}$$

where

 R_c

 Ω_c and Ω_t

is the uniaxial compressive strength $(R_c > R_t)$ is the biaxial compressive strength ($R_b > R_c$) is the uniaxial tensile strength ($R_t > 0$) are hardening/softening functions in compression and tension, respectively. When using ideal plasticity after yielding, these values are equal to 1.



 J_2 is the second stress invariant of the deviatoric stress tensor

 σ_{ij} with i, j = 1,2,3 are the stress tensor components.

The yield surfaces given by Equations (28) and (29) are shown in Figure 14 in three and two-dimensional spaces (see the resemblance of Figure 14b and Figure 7). Simplest, the material model can be defined only by using elastic material data (modulus of elasticity and Poisson's ratio), uniaxial and biaxial compressive strengths and uniaxial tensile strength. Using only these definitions, the material behavior is perfectly plastic after yielding. A perfectly plastic or ideally-plastic behavior after yielding is assumed here because even through a lot of trial-and-error, the finite element solutions did not converge when applying a softening behavior to the material model. Material parameters used in both global and local models are shown in Table 6.

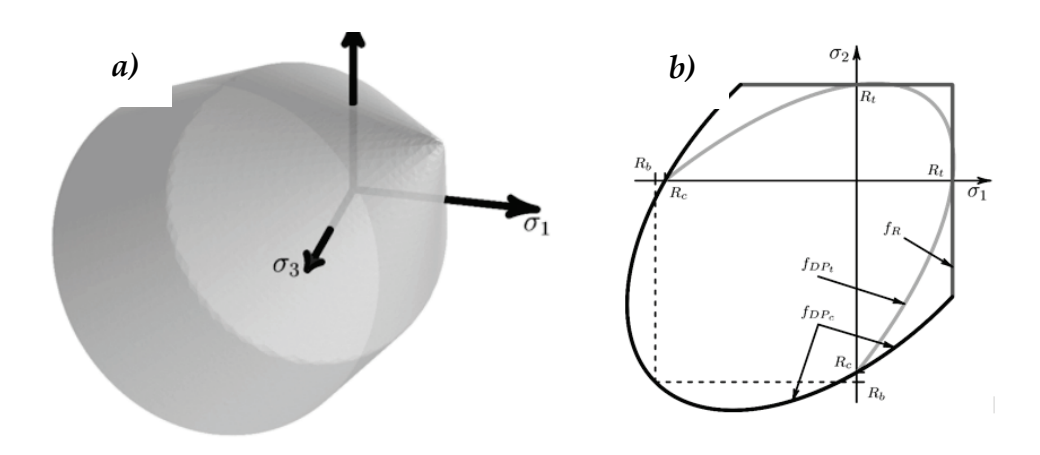


Figure 14. Yield surface given by f_{DP_t} and f_{DP_c} of Drucker-Prager Concrete in the principal stress domain in a) 3D and b) 2D. Part b) also shows a Rankine tension failure surface denoted by f_R which is not used here. (Ansys 2020).

Yielding of the material occurs when $f_{DP_t} = 0$ or $f_{DP_c} = 0$. Considering the magnitude and direction of plastic straining, the *flow rule* describes these measures. According to the Ansys manual, the flow rule is given by Equation (36).

$$\{d\varepsilon^{pl}\} = \lambda \left\{ \frac{\partial Q}{\partial \sigma} \right\} \tag{36}$$

$\{darepsilon^{pl}\}$	is a vector containing the plastic strain increment entries is a plastic multiplier that governs the amount of plastic
	straining
Q	is function of stress termed the plastic potential or flow
	potential given in Equations (37) and (38) for the used
	material model
$\{\sigma\}$	is a vector containing the stress tensor entries.
	λ Q



For Drucker-Prager Concrete model the flow potential in tension and tension-compression yielding Q_{DP_t} , and in compression yielding Q_{DP_c} are given in Equations (37) and (38). Without hardening or softening rules (ideal-plasticity after yielding), the material model assumes an associated flow which means that plastic strains increase to the direction normal to the yield surface. (Ansys 2020).

$$Q_{DP_t} = \frac{\sigma_e}{\sqrt{3}} + \delta_t \beta_t \sigma_m \tag{37}$$

$$Q_{DP_c} = \frac{\sigma_e}{\sqrt{3}} + \delta_c \beta_c \sigma_m \tag{38}$$

where δ_t and δ_c are the tension and compression dilatancy parameters, respectively. For associated flow, $\delta_t = \delta_c = 1$.

Unfortunately, Ansys manual does not define a material parameter needed to compute the plastic multiplier λ shown in Equation (36). This material parameter is called "translation multiplier" and it is marked with "C" or "C". For additional information, see the theory reference of Ansys manual part 4.2. "Rate-Independent Plasticity".

It should be noted that the material model does not recognize "discrete" cracks in the body. Cracking is expected to occur when yielding occurs (on the yield surface given by f_{DP_t}) and plastic strains are formed. As the concrete parts that have yielded no longer have stiffness due to ideal-plasticity, the reinforcement in these parts start carrying additional loads if loading is increased so that the stresses increase only in the reinforcement. The reinforcement stresses are maximized in parts where plastic strains are the largest as will be explained in Part 4.4.1. As the reinforcement stress is the only variable in the crack width calculation of EC2 part 1-1 (when the position where crack width estimate is performed is fixed), plastic strains in concrete can be used to locate positions where crack widths are maximized. Therefore, plastic strains are used to display modelling results in forthcoming parts of this thesis. Another option would be to display the total strain without thermal strains, but this does not directly tell if concrete has yielded. With only plastic strains displayed, any value over zero means that concrete has exceeded its tension capacity and cracking occurs.

Due to the post-yielding ideal-plasticity of the material model, the stresses in the reinforcement given by FEM are lower than in reality as the concrete does not lose its tensile capacity. When concrete loses its tensile capacity, the reinforcement must carry additional loads as there is no concrete at the crack opening. This is considered in the crack width estimates by manually transferring tensile stresses from concrete to the reinforcement. The transferring process is presented in Annex 3.

The Drucker-Prager Concrete is not the most sophisticated material model available but compared to other material models the number of needed parameters (three) is substantially lower. For example, simple Mohr-Coulomb model requires five parameters plus additional two parameters for Rankine yield surface for tension. These numbers do not include the parameters related to linear elasticity and including hardening/softening effects would increase the number of necessary



parameters. (Ansys 2020.) Furthermore, the parameters needed for the Drucker-Prager Concrete model are more easily available compared to those needed for Mohr Coulomb and other models.

Here, the material model is not validated with an external model. However, for example Kedziora and Anwaar (2019) performed FEA of a circular composite column loaded eccentrically in the vertical direction where concrete was modelled using Drucker-Prager Concrete. The results of FEA (in terms of maximum deflection versus axial load) were then compared to available test results with satisfactory (or excellent as per the authors) agreement. Even though the scope of their study differed from the scope of this thesis, the study included features relevant in this thesis. With a thin steel tube covering the concrete, the triaxiality of stress state is considered in the model via confinement. Furthermore, the degree of degradation or failure in their study is more severe compared to the problem at hand showing that the material model can be used to model the nonlinear response of concrete atleast in problems similar to that described above. However, validating the material model with suitable a test setting or earlier studies would increase its credibility in this application.

Table 6. Material parameters for concrete and reinforcement.

Material parameter	Value		
Concrete			
Density	2300 kg/m^3		
Elastic modulus (nominal)	30 GPa		
Elastic modulus (creep modified)	13 GPa*		
Poisson's ratio	0.2		
Uniaxial compressive strength	30 MPa**		
Biaxial compressive strength	36 MPa		
Uniaxial tensile strength	3 MPa		
Thermal expansion coefficient	$9.2 \cdot 10^{-6} \text{ 1/°C}$		
Specific heat	900 J · (kg · °C) ⁻¹		
Thermal conductivity	$1.5 \mathrm{W}\cdot(\mathrm{m}^{\circ}\mathrm{C})^{-1}$		
Reinforcement			
Density	7850 kg/m^3		
Elastic modulus	210 GPa		
Poisson's ratio	0.3		
Thermal expansion coefficient	$9.2 \cdot 10^{-6} \text{ 1/°C}$		

^{*}corresponds to $\varphi \approx 1.3$ as per Equation (25)

4.4 GLOBAL MODELLING

4.4.1 Topology and element types

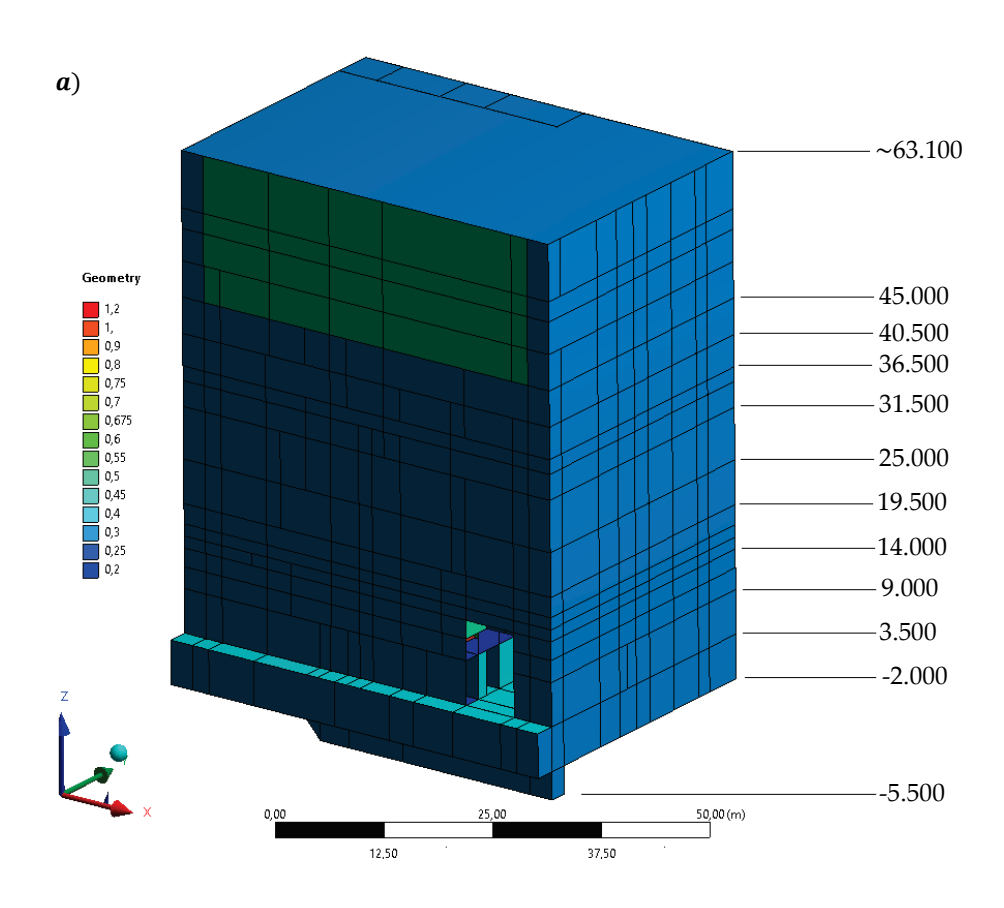
The topology of the global model consists of shell surfaces that represent walls and floors. Large openings in the reactor building are considered in the topology. For simplicity however, door openings and similar are left unmodelled. This simplification is non-conservative, but it fits the overall goal of the global modelling. In reality, doorways are not empty in the sense that they are filled with doors that add stiffness to the doorways. Even though the doors are not fixed to the surrounding walls and floors similarly as a doorway modelled with concrete,



^{**}corresponds to cubic strength of K30 strength class concrete that is mostly used in the reactor building according to data provided by TVO.

the simplification is estimated to be reasonable. A topologically major simplification is made to the space below containment building. As the containment building is not present in the model, the space below it is left unmodelled and replaced with a thick shell. An overview of the global model is shown in Figure 15. A global mesh size of 0.5 meters is used in the global model.





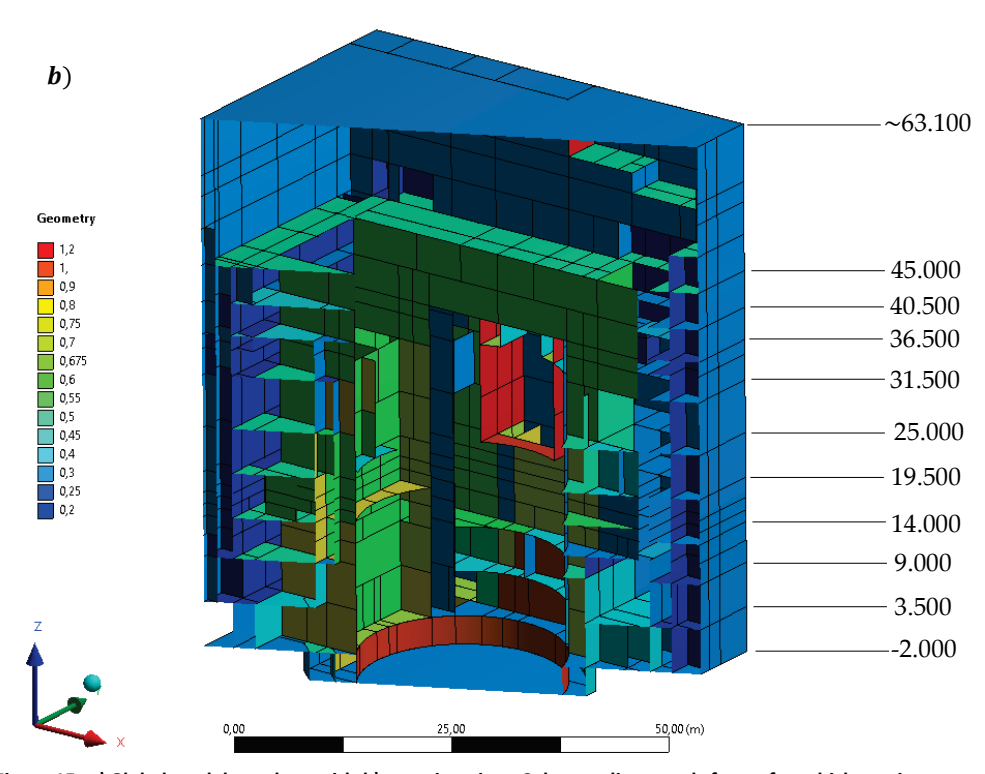


Figure 15. a) Global model topology with b) a section view. Colour coding stands for surface thickness in meters. The directions of global coordinates are parallel to the reactor building edges. The floor at elevation -9.000 is not shown in the figure.



The walls and floors are modelled with "SHELL181" elements. The element is quadrilateral, and it has four nodes, although a three-node triangular element is also available. The element has both membrane and bending stiffness, thus having six displacement degrees of freedom (translation and rotation in three Cartesian local coordinate directions) in each node. Each node can also be given two temperature body loads allowing a linear temperature distribution in the thickness direction of the element. SHELL181 element is illustrated in Figure 16 with both quadrilateral and triangular shapes. (Ansys 2020.)

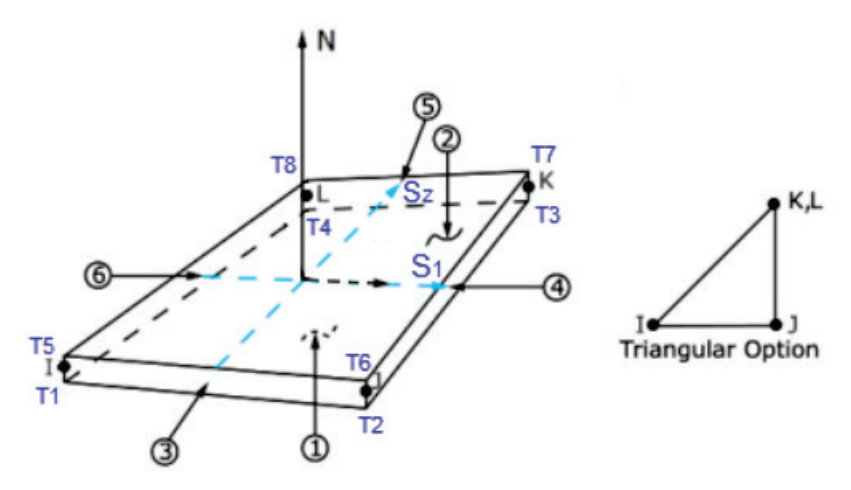


Figure 16. SHELL181 element. I, J, K and L denote node locations, circled numbers denote the faces, and T1...T8 denote the possible temperature body loads (Ansys 2020).

The SHELL181 elements can be reinforced with "REINF265" elements that are assumed to have a perfect bond together. The reinforcing can be executed with several methods, but here a smeared layer approach is used. This method allows embedding reinforcing layers that act as membranes with unidirectional stiffness within the concrete medium. A shell element can be assigned several layers of reinforcing, which allows reinforcing both top and bottom sections of the concrete walls and floors. Furthermore, the orientation of the reinforcement can be selected to be parallel to both height and width of the floors and walls. Reinforcement in the thickness direction cannot be modelled. The reinforcing layer in a three-dimensional shell element is illustrated in Figure 17. (Ansys 2020.)

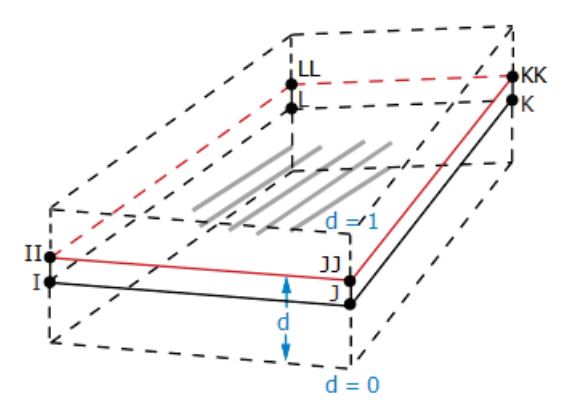


Figure 17: Smeared reinforcement layer in a 3-D shell element, such as SHELL181 (Ansys 2020).



A reinforcing layer is defined by assigning it a material, a thickness, the orientation, and the distance from the base shell element. The layer thickness, t_{rl} , is indirectly assigned by giving the cross-sectional area of a single rebar, A_r , and the distance between adjacent rebars, s_r . The layer thickness is given in Equation (39).

$$t_{rl} = \frac{A_r}{S_r} \tag{39}$$

To simplify the setting, the rebar layers are assumed to have an equal relative distance, $d_{rel} = 10$ %, from the bottom and top sections of all floor and wall sections. Walls are reinforced so that the area of vertical and horizontal reinforcement equals to 0.3 % of the concrete area in that section. Floor slabs are assumed to have reinforcement equalling 0.3 % of the concrete area in that section in the global X and Y directions. The assumed reinforcement values are to be divided equally to both faces of the walls and the floor slabs. The orientations of reinforcing bars are assumed to be such that they are parallel to the global coordinates of the reactor building shown in Figure 15. There are curved floors at the border of containment building and the reactor building that in reality also have curved reinforcement. However, the number of curved reinforcing bars is negligible compared to that in global coordinate directions, and they are therefore omitted.

Figure 18 shows a common discretization error with shell elements at intersection of two structural pieces, for example walls. As shown by the figure, the intersecting pieces partly overlap on the inside corner meaning also that the reinforcing layers overlap each other. On the outside corner however, the situation is opposite.

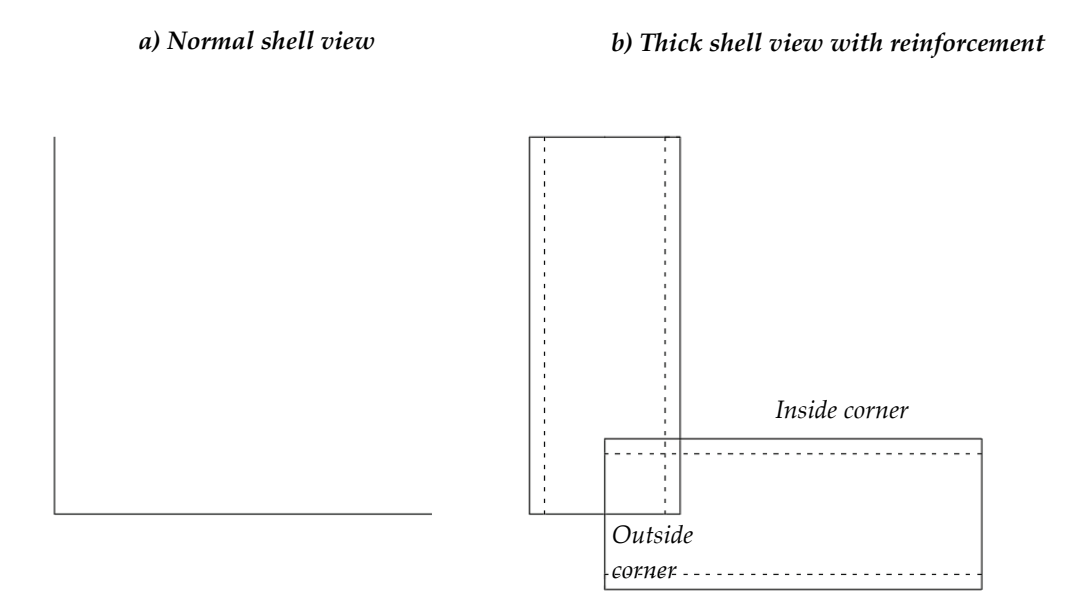


Figure 18. Intersection of two structural pieces with a) normal shell view and b) with a thick shell view. In b) solid lines represent boundaries of concrete and dashed lines represent reinforcing layers.



4.4.2 Loading of the global model

The global model is loaded with both mechanical loads and thermal loads. The number of possible loading scenarios is great, and therefore choosing the scenario will involve arbitrariness. The chosen loading scenario should represent the reactor building in normal, non-accidental conditions that could occur in everyday operation.

The loading is applied in six static steps that are shown in Table 7. As the table shows, load step 2 includes three load types. Light imposed loads are applied to outer perimeter floors where the amount of heavy equipment is generally lower, whereas heavy imposed load is applied to inner perimeter floors where heavier equipment lies (see Figure 19). The snow and wind load magnitudes are assumed not to include magnifying effects such as gust winds. Cranes, located at elevation +45.000, are omitted in the model as their maximum weight equals to some 2 % of the deadweight of a single storey, as they are far away from areas of interest (where thermal stresses are relevant) and as applying the load realistically is difficult.

Table 7. Loading of the global model.

Load step	Load type	Magnitude
1	Self-weight of the	
	structure	-
2	Light imposed load	$2 kN/m^2$ on outer perimeter floors
2	Heavy imposed load	$4 kN/m^2$ on inner perimeter floors
2	Transport vehicle	24 tonnes on an area of $48\ m^2$ near the delivery zone
3	Snow load	$0.6 \ kN/m^2$ on the roof
3	Wind load (X direction)	$0.6 \ kN/m^2$ from positive to negative X axis
3	Wind load (Y direction)	$0.6 \ kN/m^2$ from negative to positive Y axis
4	Temperature step 1	Max. 43 °C (+21 °C to reference temperature)
5	Temperature step 2	+12 °C to certain rooms (Max. 55 °C)
6	Temperature step 3	$+10~^{\circ}\text{C}$ to certain rooms (Max. 65 $^{\circ}\text{C}$)

The temperature steps in Table 7 are applied and defined as follows. In temperature step 1, the average room temperature values from the last three years are imposed on the corresponding shell surfaces. In this step, the maximum temperature is 43 °C. According to the temperature measurement data, the rooms with increasing temperature trendline are varied in temperature steps 2 and 3, while the temperatures in the rest of the rooms are held constant. In all the steps, the reference temperature for thermal strains is 22 °C.



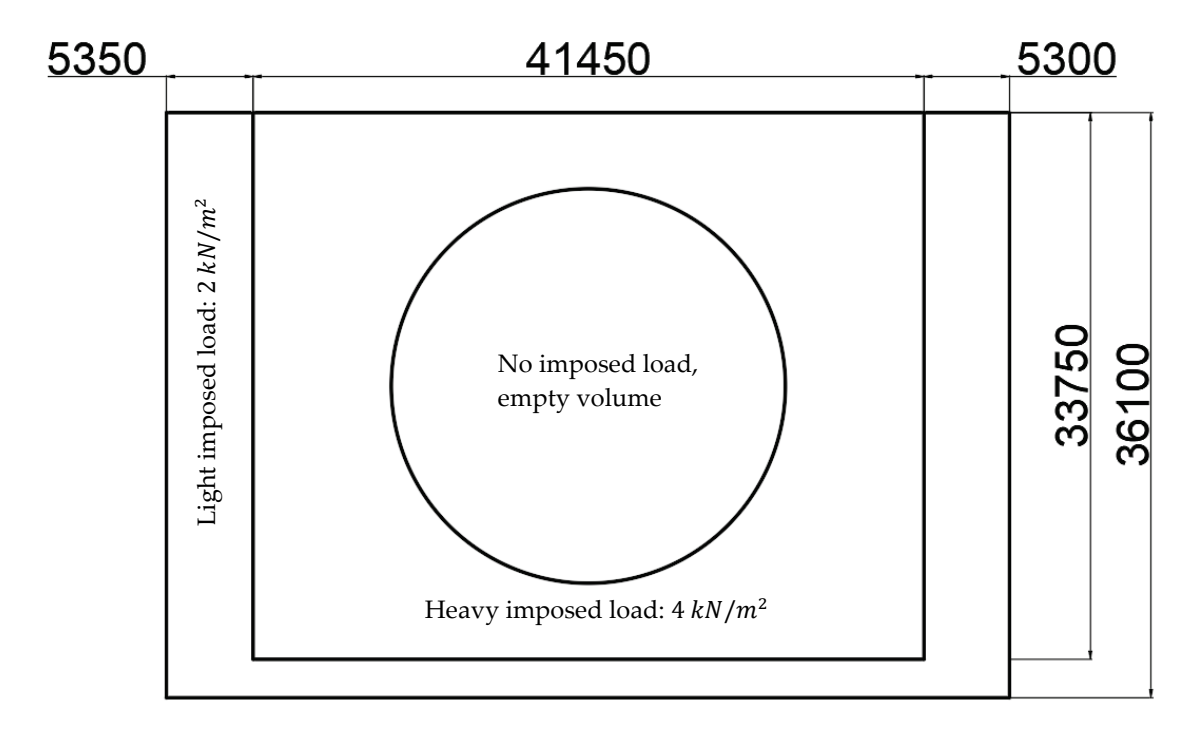


Figure 19. Imposed loads on a generic elevation. Dimensions are in millimetres.

4.4.3 Boundary conditions

The global model is supported by elastic supports on faces (both vertical and horizontal) that are ground-supported. The magnitude of the elastic supports is arbitrarily chosen to be 10^8 N/m 3 . This can be converted to units of [N/m] by multiplying the support magnitude by the area of the ground-supported faces. The magnitude of the elastic supports imitates a fixed support but allows for deformation on the supported faces. The rooms of interest that are subjected to temperature differences are located multiple stories away from the supports. Thus, the effect of boundary conditions is negligible when considering the state of those rooms.

4.4.4 Global modelling results

The results of the global modelling suggest that room temperature differences can induce considerable stresses and tensile yielding in the reactor building. With the given loading, the minimum principle stress has an absolute value of some 21 MPa, and thus compressive yielding is not occurring. Tensile yielding (measured in this discussion by maximum principal plastic strain) occurs on the ground-supported faces and in the walls and floors of the rooms that are subjected to temperature differences. In these rooms, tensile stresses are induced on the faces with lower temperatures as explained by the simplified idea in Figure 20.



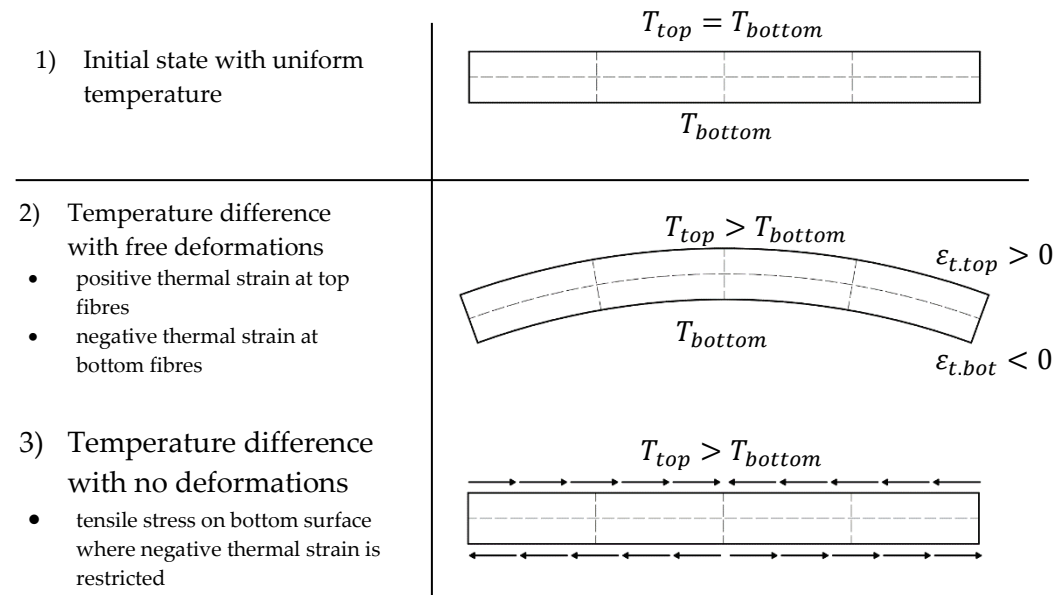


Figure 20. Effect of temperature differences on shell surfaces. A temperature difference with no allowed deformations induces a tensile stress to the colder surface and a compressive stress to the warmer surface, as shown by State 3.

Tensile stresses are also induced to structural pieces where intersecting walls or floors are imposed to a higher temperature. In such situations, the thermal elongation of the intersecting wall or floor tends to deform the structural piece it intersects, as shown by Figure 21. However, the problem in the reactor building is more closely related to the temperature differences between rooms where thermal stresses induced by the idea in Figure 20 are more relevant. Furthermore, the number of areas where tensile stresses are caused by intersecting pieces is minimal, which could imply that the problem is considered already in the design process.

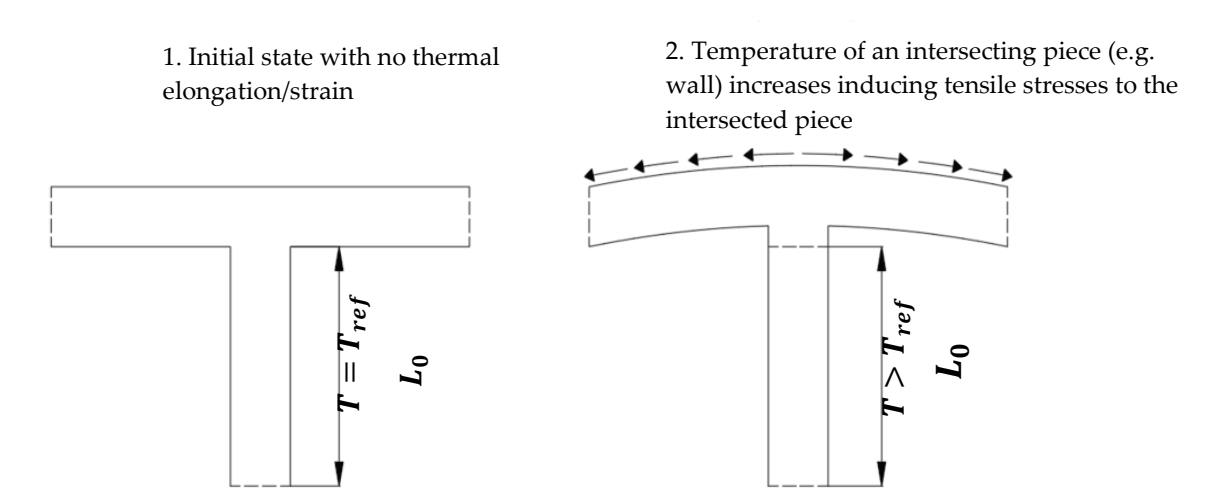


Figure 21. Effect of temperature changes at an intersection of two structural pieces.



Figure 22 shows the room under concern together with the thermal boundary conditions. Figure 23 and Figure 24 show the maximum principal plastic strain distribution for load steps 3 to 6. As the figures shows, no plastic strains are present with bare mechanical loading (load step 3). With increasing temperature difference, the amount of plastic strain increases significantly which suggests that thermal loading is a source of high stresses in the reactor building. The largest values of plastic strain in walls locates at the intersection of two walls, where deformations are restricted by the upper and lower floors as well as the intersecting walls themselves. The high temperature of the studied room also induces plastic strains to the floor of the room above it which is at constant 22 °C. The magnitude of the plastic strain is larger in the floor which can be explained by extra constraints (by walls) in the above room that are not shown in the figure but are shown in Figure 27 for the local model. For reference, the strain corresponding to tensile strength is some $1 \cdot 10^{-4}$ as shown by Equation (23).

The stress state caused by the thermal loads in the room is shown in Figure 25 and Figure 26 where the maximum principal stress is plotted for load steps 3 to 6. The maximum principal stress with bare mechanical loading reaches a value of some 1.2 MPa locally, while already at load step 4 the value reaches 2.6 MPa and over. Because of yielding of concrete, the stress states caused by mechanical loading and thermal loading cannot be directly compared. However, the difference between load steps 3 and 4 show that the effect of thermal loading is more significant than mechanical loading with the given loading scenario already at low temperature differences. Furthermore, at load step 3 the maximum principal stresses are negative or close to zero in areas where high maximum principal stresses or maximum principal plastic strains are occurring at load steps 4 to 6. This suggests that thermal loads can counteract the effect of mechanical loads even with low temperature differences. Furthermore, if the loading scenario is such that tensile stresses from mechanical loads are magnified by thermal loads, the tensile stresses and strains can be significant and should be considered in design.



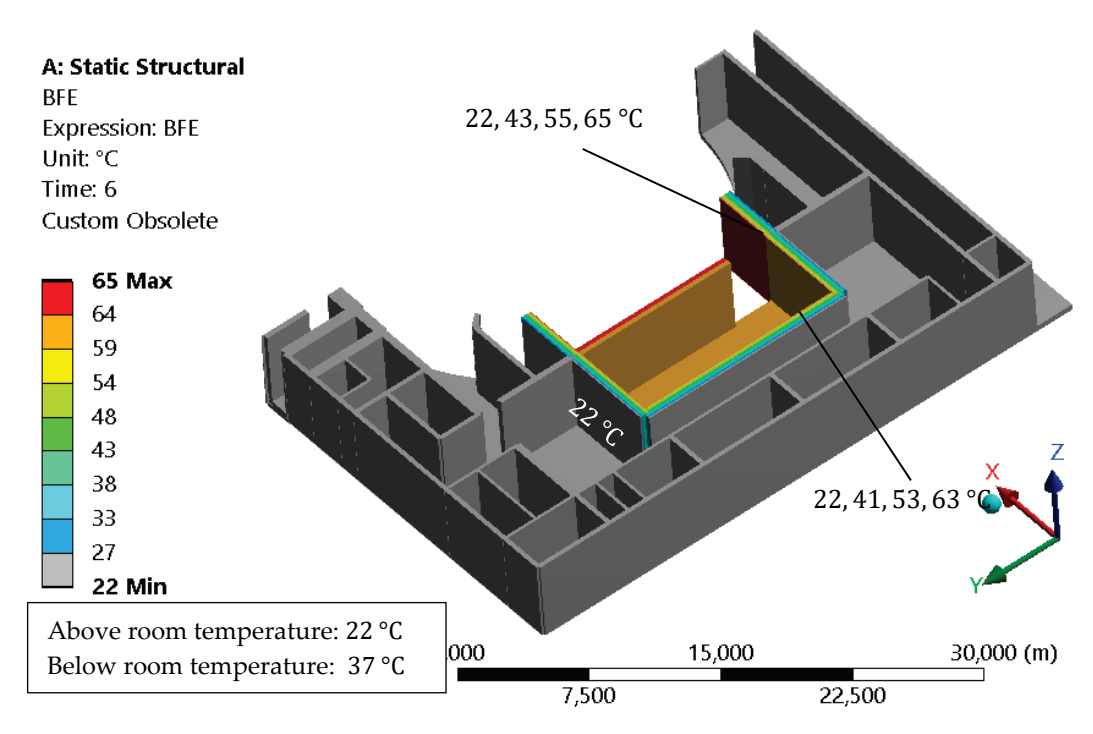


Figure 22. Temperature boundary conditions of the room under concern at load steps 3...6.



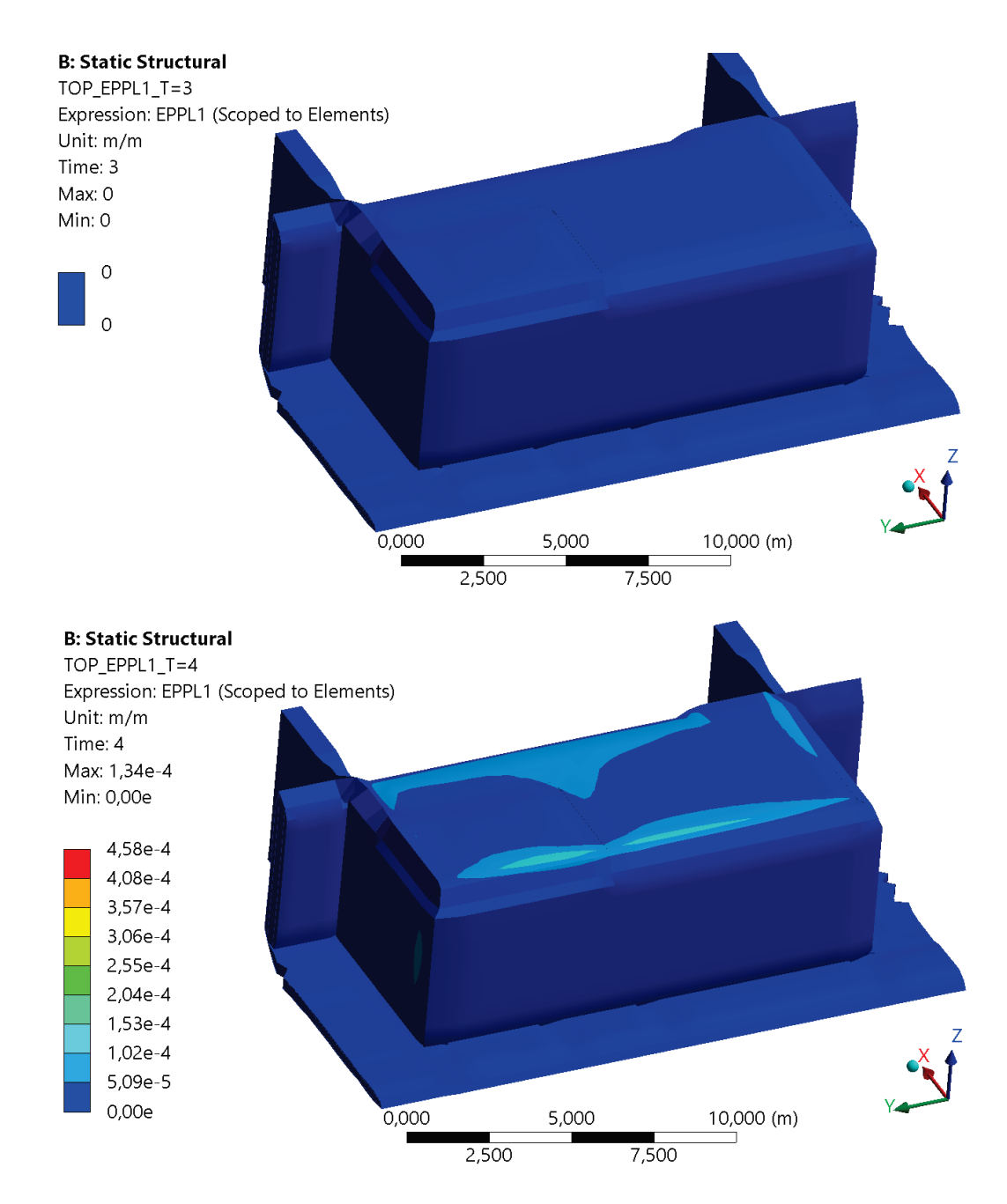


Figure 23. Maximum principal plastic strain distribution of the room under concern at load steps 3 and 4. Results coloring is normalized to that of load step 6.



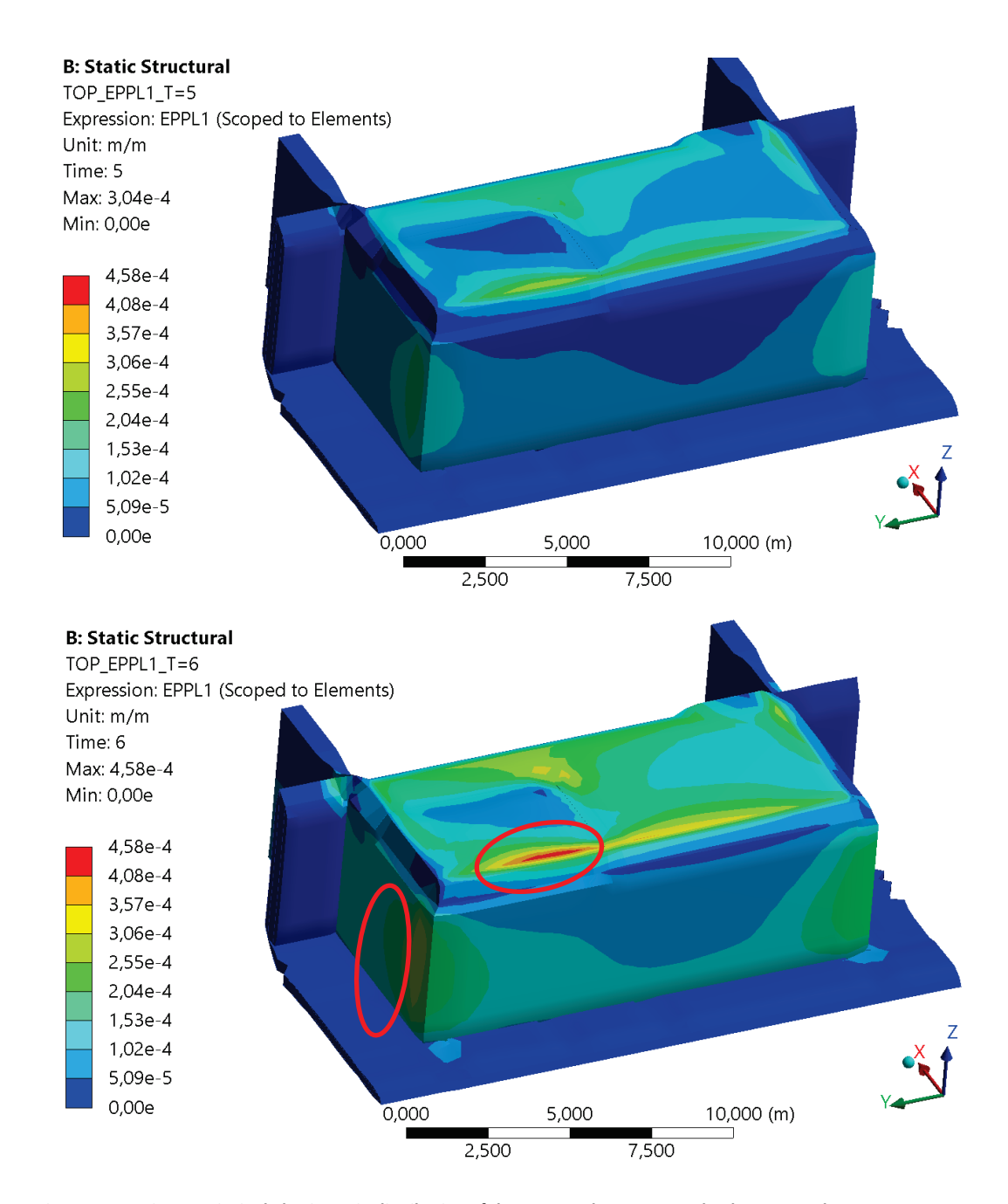
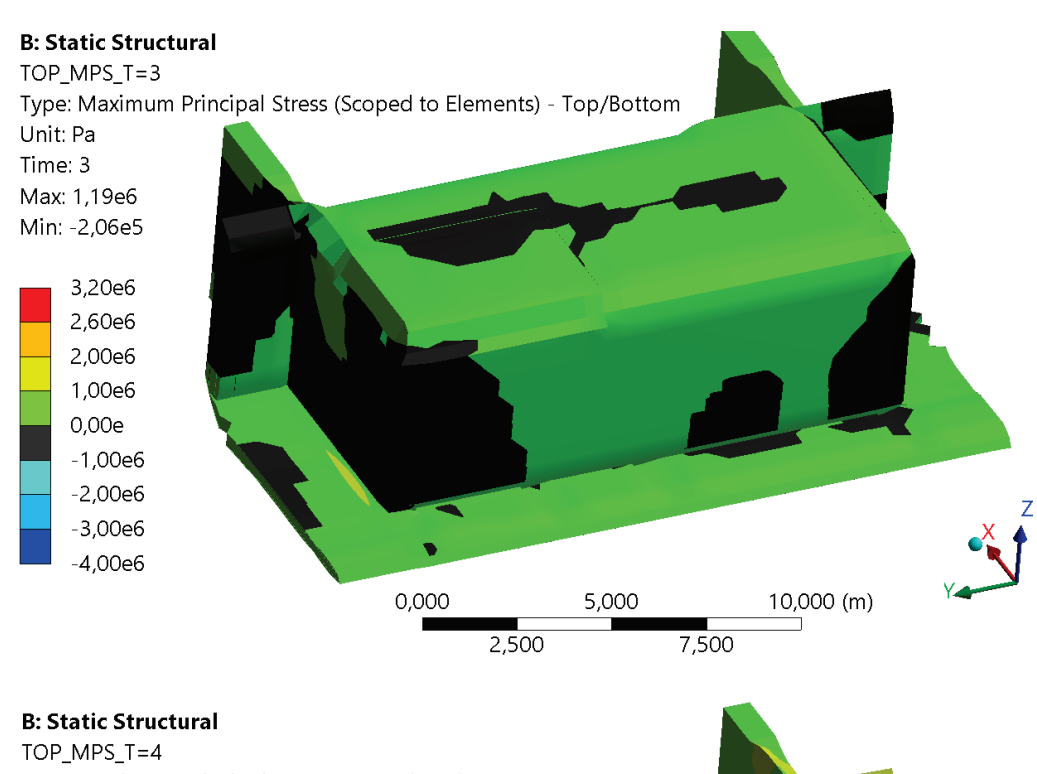


Figure 24. Maximum principal plastic strain distribution of the room under concern at load steps 5 and 6. Results coloring is normalized to that of load step 6. The red ellipses represent positions where crack width estimates are performed.





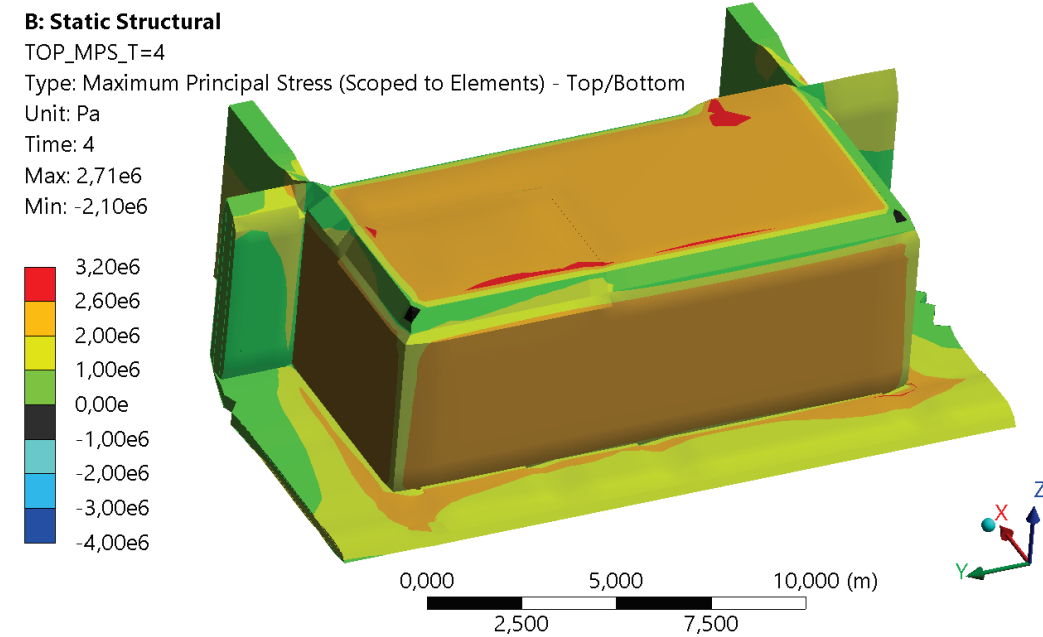


Figure 25. Maximum principal stress distribution of the room under concern at load steps 3 and 4.



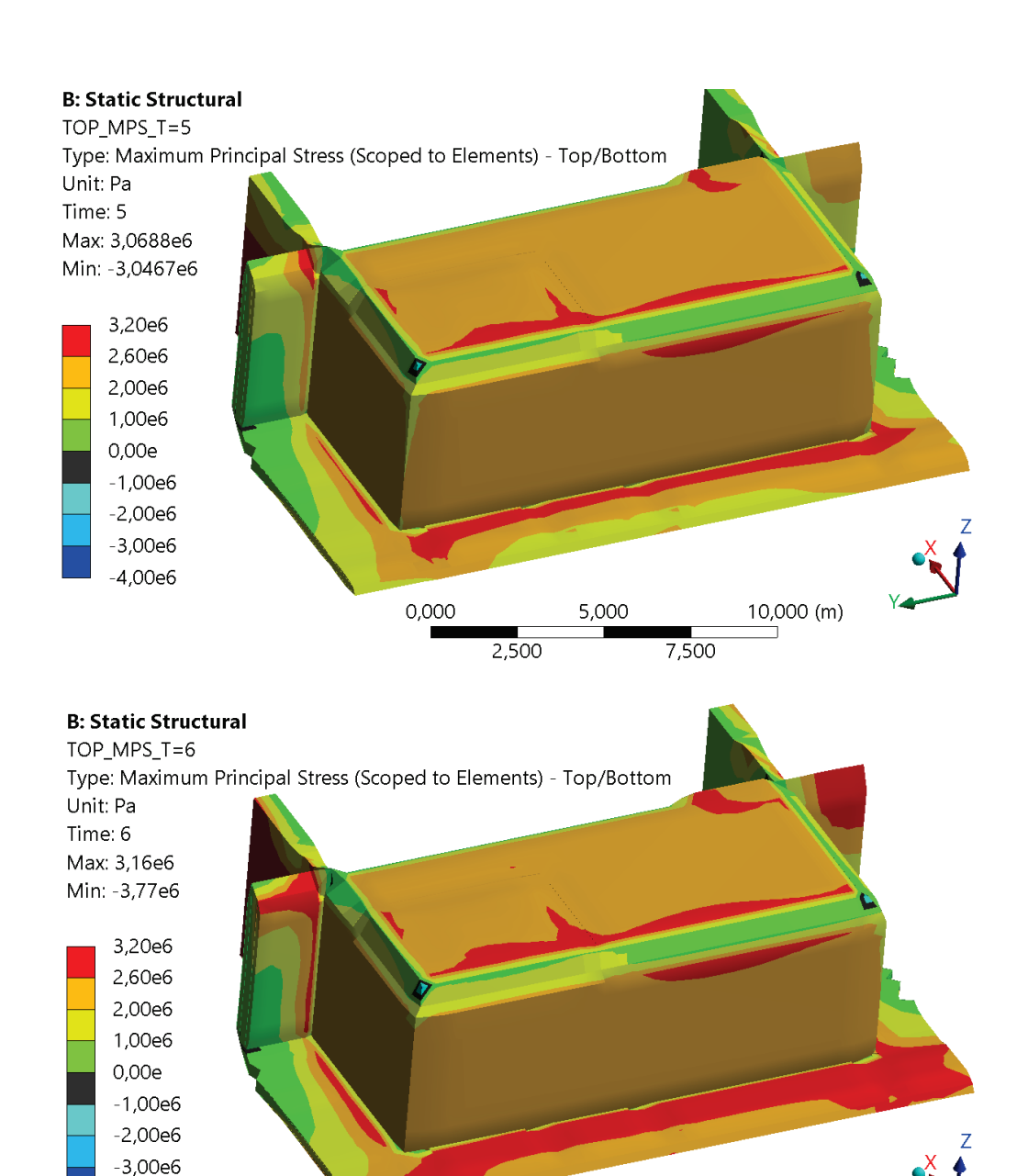


Figure 26. Maximum principal stress distribution of the room under concern at load steps 5 and 6.

0,000

2,500

5,000

7,500

10,000 (m)

-4,00e6



Maximum principal plastic strain or maximum principal stress do not by themselves fully consider the integrity of the reactor building. Converting the global modelling results to crack width estimates requires use of analytical methods and simplifying assumptions. In this thesis, the crack widths are estimated by using EC2 part 1-1 method. The method is presented in Annex 1 and related calculations concerning global model are shown in Annex 2. The results are summarized in Table 8, and the positions where crack width estimates are made are shown in Figure 24. For reference, EC2 part 1-1 provides a recommended maximum crack width value of 0.3 mm for most exposure classes. As Table 8 shows, with the temperature conditions met in the operation of the plant nowadays (load step 4), the crack width estimates remain well under the recommended value. However, at load steps 5 and 6, the recommended value is exceeded.

Table 8. Maximum crack widths in the studied room according to global modelling results.

Load step	Maximum crack width, walls (mm)	Maximum crack width, floor above (mm)		
3	No cracking*	No cracking*		
4	0.122	0.187		
5	0.371	0.336		
6	0.643	0.548		

^{*}No plastic strains at this load step in positions where crack widths are evaluated.

All in all, the results of global modelling can be summarized as follows. The model shows that positive temperature deviations from a reference temperature tend to induce considerable tensile stresses and plastic strains in comparison with mechanical loading. The magnitude of plastic strains is generally maximized near intersections of structural pieces where free thermal deformations are more strictly restricted. As illustrated by the idea in Figure 20, compressive stresses are developed to the surfaces with warmer temperature. As a generalization, this tends to protect the floor or wall sections from through-thickness cracking. However, the results suggest that increasing the temperature can have a significant effect on the crack widths, and if crack widths are the only criteria for the integrity of the building, variations from the design temperature should be performed cautiously. Although load steps 5 and 6 resulted into exceedance of the recommended value of 0.3 mm, it should be noted that the structural response to thermal loads is estimated to be localized. Considering the localized response and the protection from through-thickness cracking, the global modelling results suggest that the integrity of the reactor building is not compromised solely by the temperature differences between rooms. However, the temperature differences may magnify the tensile stresses or strains where they are already present from mechanical loading. It should be noted that the global model does not consider the primary thermal stresses and it involves topology discretization errors due to the use of shell elements. Therefore, performing local modelling with solid elements is necessary.



5 Local modelling

5.1 GENERAL INFORMATION

This chapter focuses on presenting the local model of the studied room mentioned in Chapter 4. First, the modelling principles and element types are discussed. Then, the results of local model are presented.

5.2 MODELLING PRINCIPLES

In local modelling, solid elements are used to represent concrete bodies which reduces the discretization error at the boundaries of adjacent structural pieces and allows for more realistic thermal boundary conditions and temperature distributions. The main objective of the local modelling is to analyze the severity of thermal stresses and to determine if nonlinear temperature distributions can induce significant thermal stresses compared to a linear temperature distribution. To tackle these objectives, shell elements are no longer sufficient.

Mechanical loading is not considered in local modelling. Ansys has a "submodelling" capability where, simplifying, the nodal degrees-of-freedom of a coarse model are mapped to a finer model. The submodelling can be performed between shell and solid models. (Ansys 2020.) In theory, this allows to map the total mechanical loads from load step 3 to the local model. In practice, the mapped results in the local model were erroneous even through a lot of trial-and-error. As the thermal loads dominated the results according to the global model, the mechanical loads were omitted wholly from the local model.

To induce a realistic temperature distribution, thermal analyzes are first performed, and the resulting temperature distributions are imposed as input values to structural analyzes. A linear temperature distribution is solved from a static thermal analysis with three different room temperature distributions that correspond to load steps 4 to 6 in global modelling. The boundary conditions in the static thermal analysis are set as face temperatures.

A nonlinear temperature distribution is solved from a transient thermal analysis with the same room temperature distributions. However, in the transient analysis thermal conditions are set as convection boundary conditions instead of direct face temperatures. This allows for the development of the temperature with time. Then, the temperature distributions are retrieved for several instances of time ranging from 10 minutes to 96 hours, after which they are imposed to a static structural analysis. As the topology model is heavy and the solution is nonlinear, transient structural analysis would require too much computational power to be reasonable. The reasons for this are explained in Section 5.3. The inaccuracy of using static structural analysis instead of transient is due to the fact that the true stress and strain states from a previous time-step are not imposed to the current time-step. However, as the temperature does not vary rapidly with time the inaccuracy is estimated to be small. This is supported by the results discussed later that suggest that the continuity stresses dominate over the primary stresses.



The analyzes with nonlinear temperature distribution are somewhat conservative from the safety point-of-view. This is because the convection boundary conditions in the transient thermal analysis are set so that the concrete bodies are at the reference temperature of 22 °C while the room air is already at the maximum temperature governed by the load step. As discussed in Part 2.3, the room temperatures take roughly 4 to 10 days to reach the operational temperature after ramp-up. During this time, the temperatures of the concrete bodies are also increased, which is not considered in the analysis.

A film coefficient (or convective heat transfer coefficient) of 12 W/(m²K) is used with the convection boundary condition in transient analysis. This value is in line with the results from Lee et al. (2009) where values of 8.1 to 29.3 W/(m²K) were reported for air velocities ranging from 0 to 4.3 m/s and concrete thermal conductivities ranging from 1.7 to 2.3 W/(mK). According to the results, the film coefficient tends to increase with increasing thermal conductivity and air velocity.

5.3 TOPOLOGY AND ELEMENT TYPES

The topology of the local model includes the studied room with its surroundings. Figure 27 shows the local topology of the room which can be compared to Figure 22 and Figure 23 for the global model. All in all, the lengths of the geometry of the local model in *X*, *Y* and *Z* coordinate directions are 11.7, 19.0 and 8.5 meters, respectively. The structural pieces are continued by 1.3 to 2 meters from the studied room so that the boundary conditions do not interfere with the results at areas of interest. Fixed boundary conditions are applied to the edge surfaces of the model in structural analyzes.

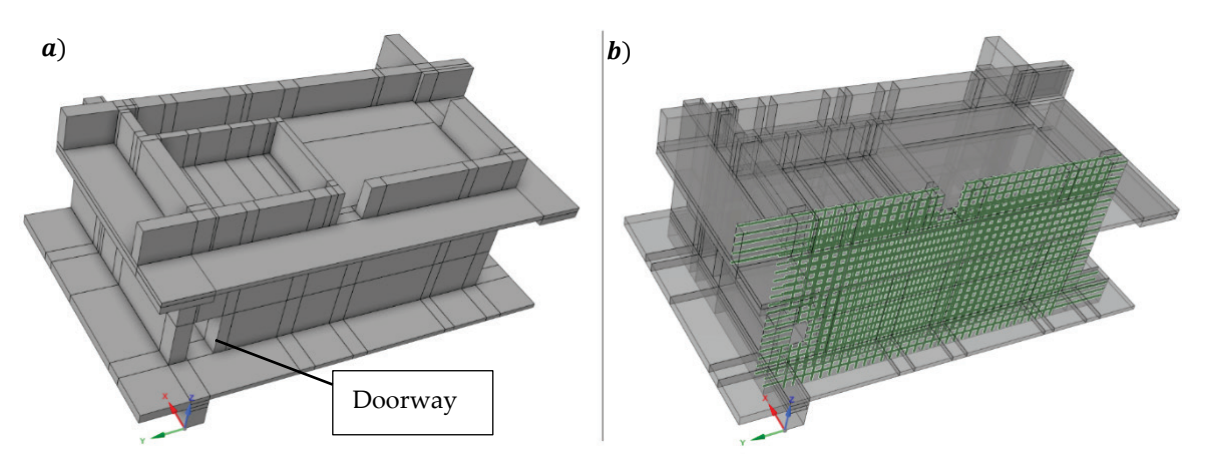


Figure 27. Local model of the studied room with a) an opaque view and b) a transparent view with reinforcement displayed on one wall.

To guarantee that results of the structural analyzes are natural (and non-discontinuous), bonded contacts are not used as they tend to yield discontinuous results, likely due to the nonlinear effects in the material model of concrete. Bonded contacts are usually applied automatically to contact regions in Ansys meaning that the bodies on those regions cannot slide or separate in relation to



each other. However, the formulation is not similar compared to simply sharing nodes, and according to Ansys bonded contact is better suited for linear solutions. Here, not using bonded contacts tends to increase the problem size, because simultaneously the topology should be discretized realistically, mesh should be kept dense and uniform, and the nodes between adjacent concrete bodies should be shared (no bonded contacts). This effectively decreases the element size to a value where the model is heavy but should yield precise results. As a result, the mesh of the local model consists of uniform cubes with a vertex length of 100 mm.

5.3.1 Elements of thermal analyzes

The mesh and element types for static and transient thermal analyzes are the same. Concrete objects are modelled using "SOLID70" linear element which is an 8-node thermal solid with temperature degrees-of-freedom in each node. An overview of the SOLID70 element is shown in Figure 28. In addition to cubic shapes, prism, tetrahedral and pyramid shape options are available, but they are not relevant here as the geometry is constructed so that the mesh consists of uniform cubes. SOLID70 elements can be loaded by convection/heat flux or radiation on the element faces or by temperature/heat generation on the element nodes (here "/" means the loading types are mutually exclusive). (Ansys 2020.) In static analysis, direct temperature loading is used whereas in transient analysis convection loading is used.

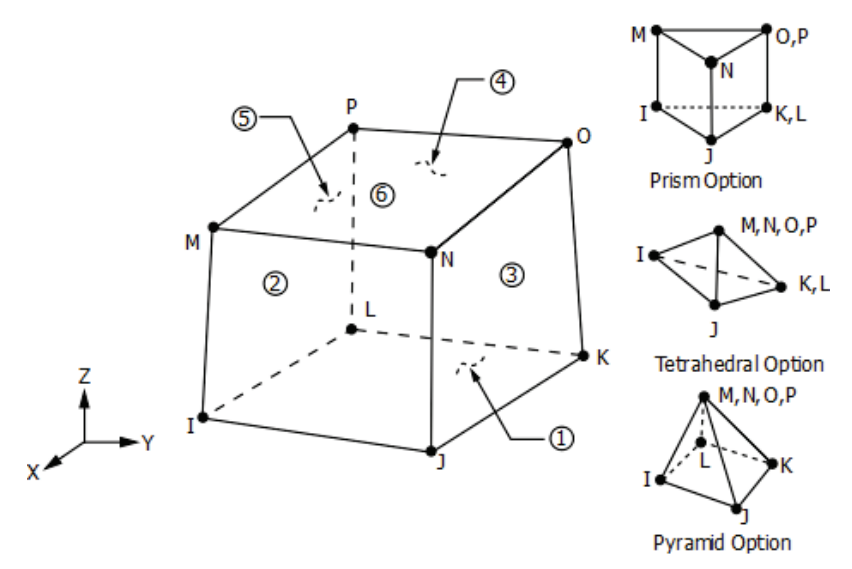


Figure 28. Element shape for SOLID70 (thermal) and SOLID185 (structural) elements of Ansys element library. Circled numbers denote the element faces. (Ansys 2020.)

5.3.2 Elements of structural analyzes

The structural counterpart of SOLID70 element is "SOLID185" linear, 8-node element which has the same shapes as SOLID70 element as shown by Figure 28. The nodal degrees-of-freedom are the displacements in *X*, *Y* and *Z* Cartesian coordinate directions. SOLID185 element can be loaded by temperature body loads in its nodes, which allows for imposing the results of thermal analyzes to structural analyzes. (Ansys 2020.)



Instead of reinforcing the structure with smeared layers as in global modelling, discrete rebars are used in the local models. The reinforcing is performed by using "REINF264" elements that have their shape and coordinate system shown in Figure 29. REINF264 elements are used with base elements (here SOLID185) to simulate reinforcing fibres that only have uniaxial stiffness. The nodes and degrees-of-freedom of the reinforcing element are identical to those of the base element, and the bond between concrete and reinforcement can be regarded as perfectly bonded. Furthermore, the temperature of REINF264 element is directly given from the base element. Thus, any temperature differences between reinforcement and concrete during the development of thermal equilibrium are neglected.

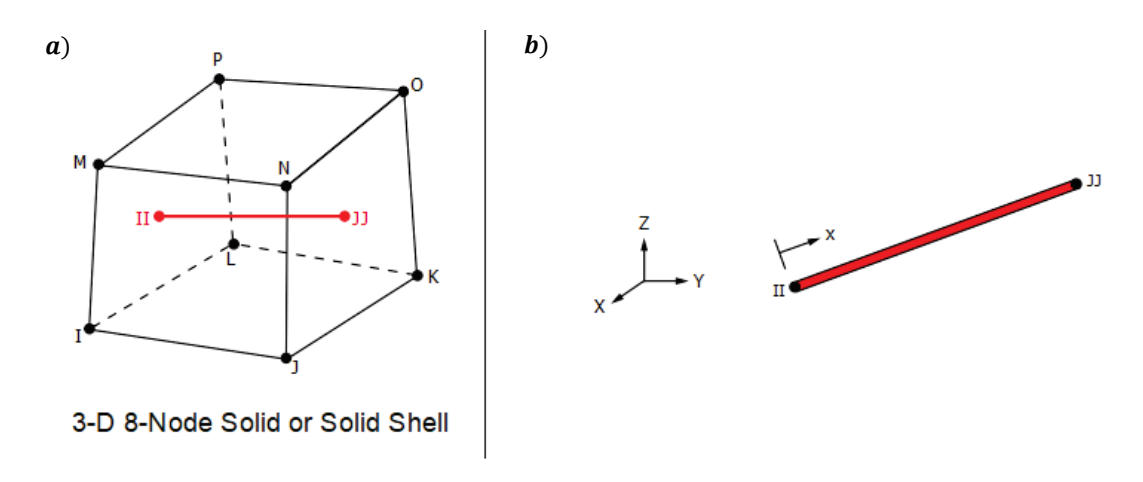


Figure 29. a) REINF264 element in a base element and b) coordinate system of the element (Ansys 2020).

5.4 RESULTS FOR LINEAR TEMPERATURE DISTRIBUTION

The results of local modelling correspond well to those of global modelling. However, the local models contain sharp corners where very localized stress singularities are induced. In the results this can be observed by high, localized plastic strains. Also, the Drucker-Prager Concrete model tends to induce stresses that exceed the tensile and compressive strengths near the fixed supports. However, stresses at the supports are not expected to affect the results at areas of interest as they are relatively far away from the supports.

Figures 30 to 32 show the maximum principal plastic strain distribution for the local model with linear temperature distribution. Respective distributions for maximum principal stress are shown in Figures 33 to 35. In the figures, the temperatures boundary conditions correspond to load steps 4...6 of the global model. Comparing the principal plastic strain distributions of local model to those of the global model (Figure 23 and Figure 24) shows that the plastic strains tend to locate in the same areas between the two models, which suggests that the thermal loads dominate in the global model and that the global modelling method has correct response to thermal loads. Even though the shape of the plastic strain distribution is similar, in the global model plastic strains are induced to the whole face already at load step 5, whereas in the local model plastic strains are more



localized around their maximum values. Of course, the mechanical loading between the models is not the same, but the global model likely over-estimates the extent of plasticity. The difference in extent cannot be explained for example by effects of gravity as the maximum principal stresses are quite low with only mechanical loading present as shown by Figure 25.

In the local model the maximum plastic strain values are notably larger compared to the global model. As the areas where the values are exceeded are very localized near sharp corners, they can likely be explained by singularities. Although geometric discontinuities (such as sharp corners) are generally positions of high stress, trial analyzes with larger element size yielded lower values of plastic strain, possibly suggesting that results in the *immediate* vicinity of corners can be regarded as singularities. The positions where plastic strains are maximized can still be considered as the positions where cracking occurs, but due to the singularities the plastic strain magnitudes should be analyzed cautiously. It should be noted that the trial analyzes did not have as uniform meshes as the actual analyzes.

The discussion above suggests that omitting doorways in the global model was a more non-conservative simplification than initially estimated during building of the global model. Any geometric nonlinearities should be considered in the presence of high loads unless making a conscious decision to omit them. Here, local modelling was used to consider doorways with more precision but if analysis is to be made only in the global extent one should be careful when simplifying the geometry.

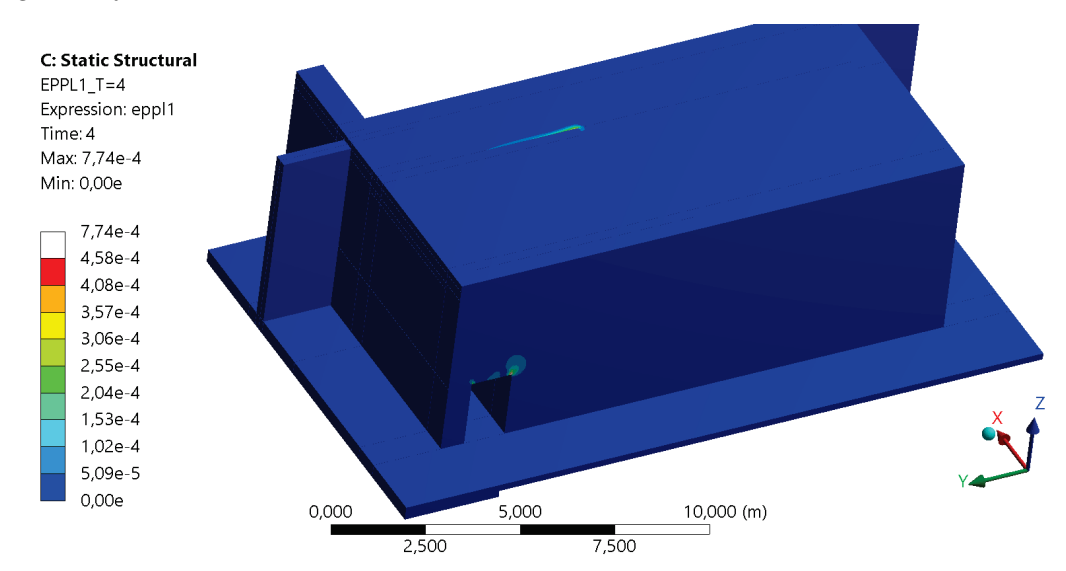


Figure 30. Maximum principal plastic strain distribution with linear temperature distribution at time step 4. The results coloring is normalized to that of global model.



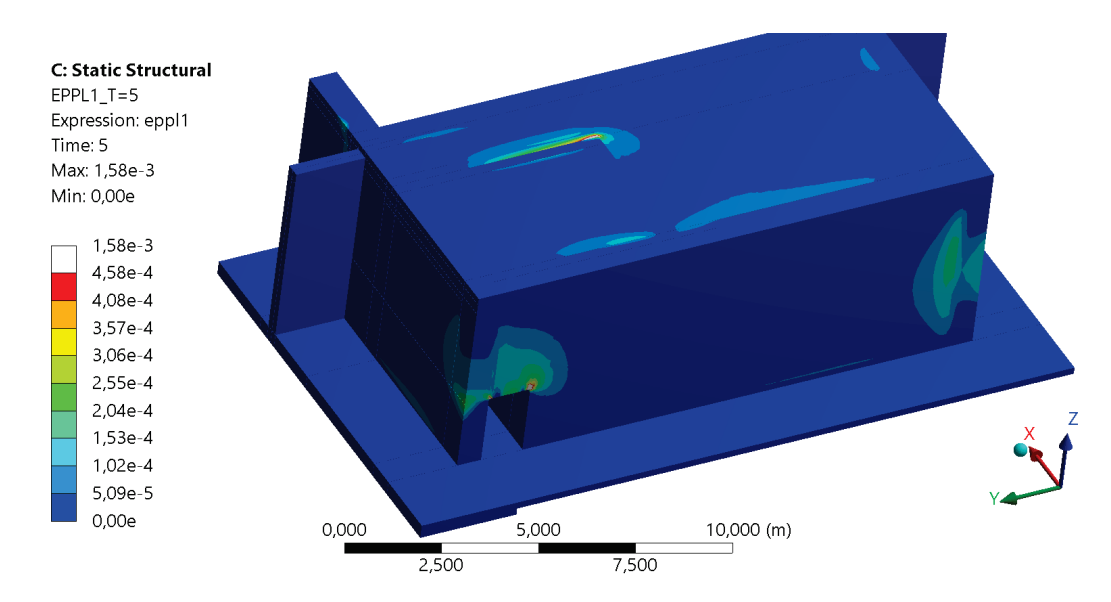


Figure 31. Maximum principal plastic strain distribution with linear temperature distribution at time step 5. The results coloring is normalized to that of global model.

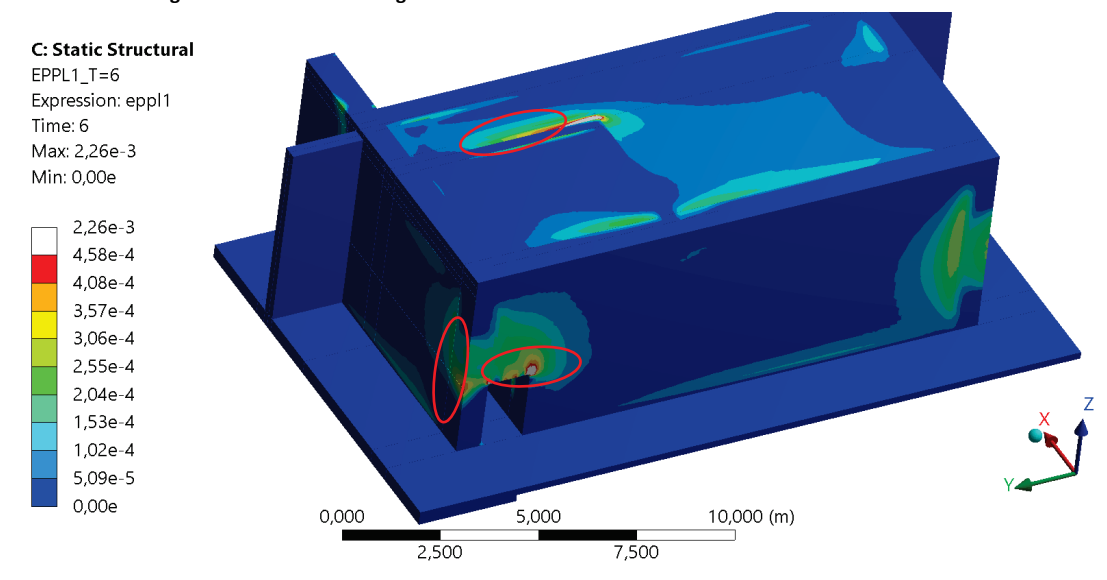


Figure 32. Maximum principal plastic strain distribution with linear temperature distribution at time step 6. The results coloring is normalized to that of global model. Circled areas represent positions where crack widths are estimated.

The maximum principal stresses are near the tensile capacity of concrete in relatively large extent even at low temperature differences as shown by Figure 33. However, the maximum principal stresses are very low or even negative at the warmer wall or floor face, and no through-thickness cracking occurs which was also the result observed in the global model. To illustrate the through-thickness effects, two cross-sections where the magnitudes of plastic strain are large are presented. Figure 36 and Figure 37 show the maximum principal plastic strain and maximum principal stress distributions at load step 6 in cross-sections above the doorway and on the floor above of the studied room, respectively. As shown by the figures, tensile yielding is relatively localized to small areas and it is not expected to occur through the whole thickness of a section. Furthermore, the



maximum principal stresses at the warmer faces are very low (generally between 0 to 1 MPa) or even negative meaning that cracking is not a relevant threat on these faces.

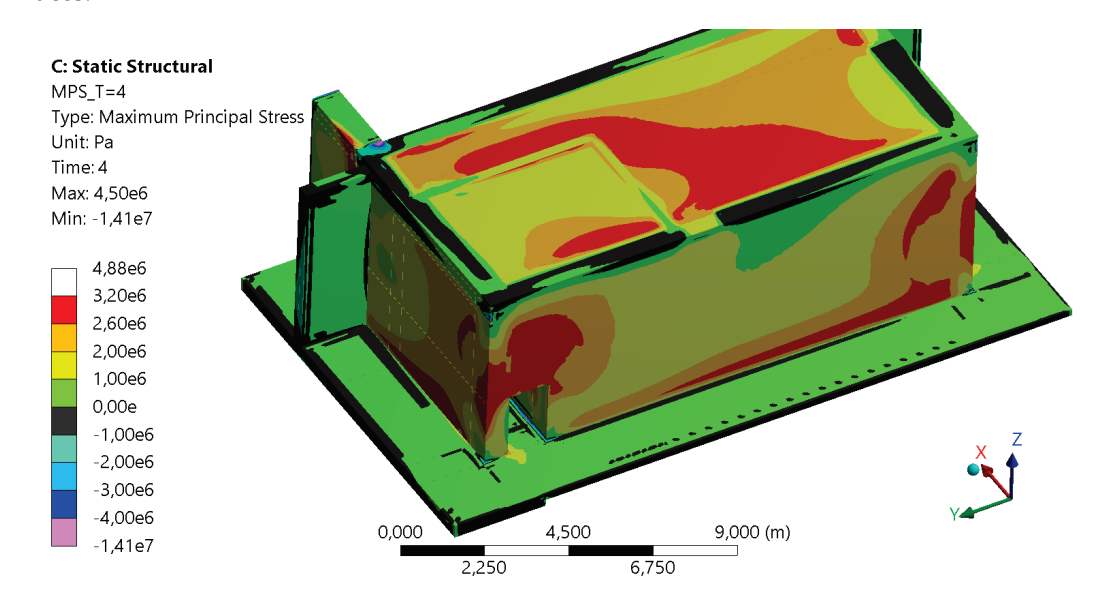


Figure 33. Maximum principal stress distribution with linear temperature distribution at time step 4. The results coloring is normalized to that of global model.

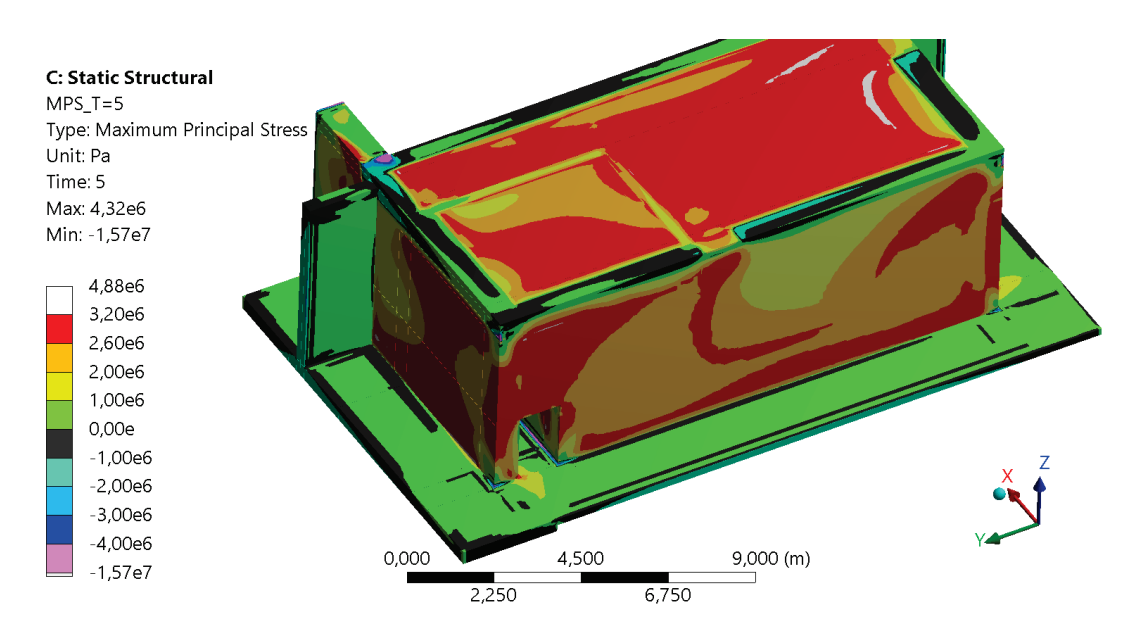


Figure 34. Maximum principal stress distribution with linear temperature distribution at time step 5. The results coloring is normalized to that of global model.



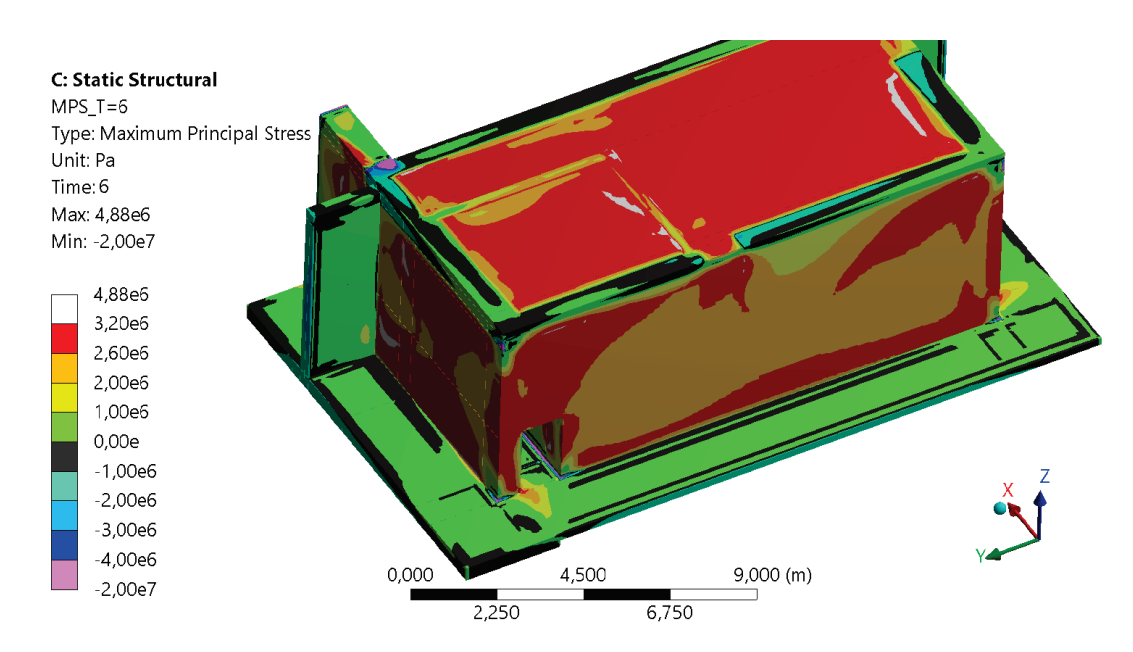


Figure 35. Maximum principal stress distribution with linear temperature distribution at time step 6. The results coloring is normalized to that of global model.



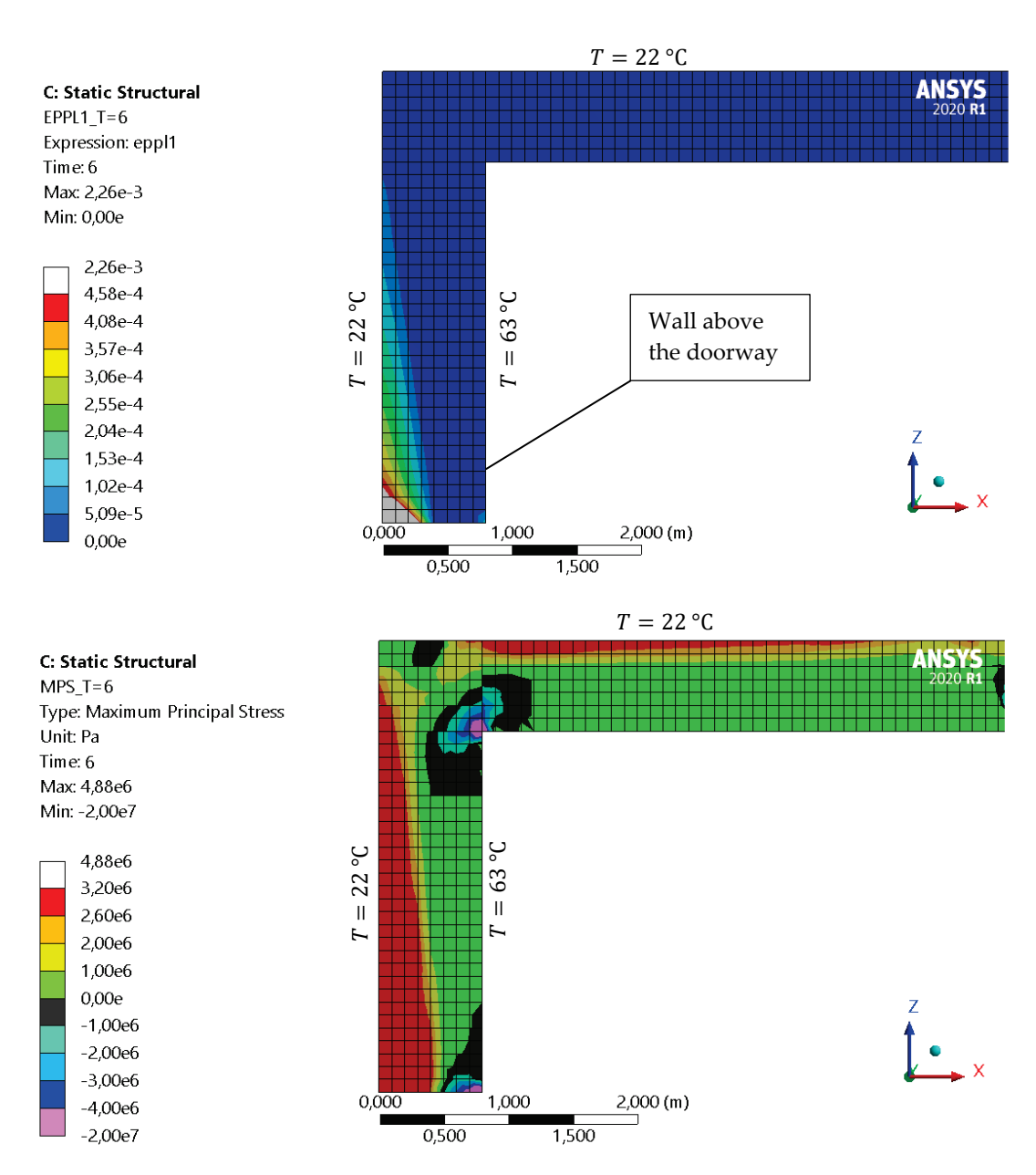


Figure 36. Maximum principal plastic strain and stress distributions for cross-section above the doorway of the studied room at load step 6. Mesh size is 100 mm.

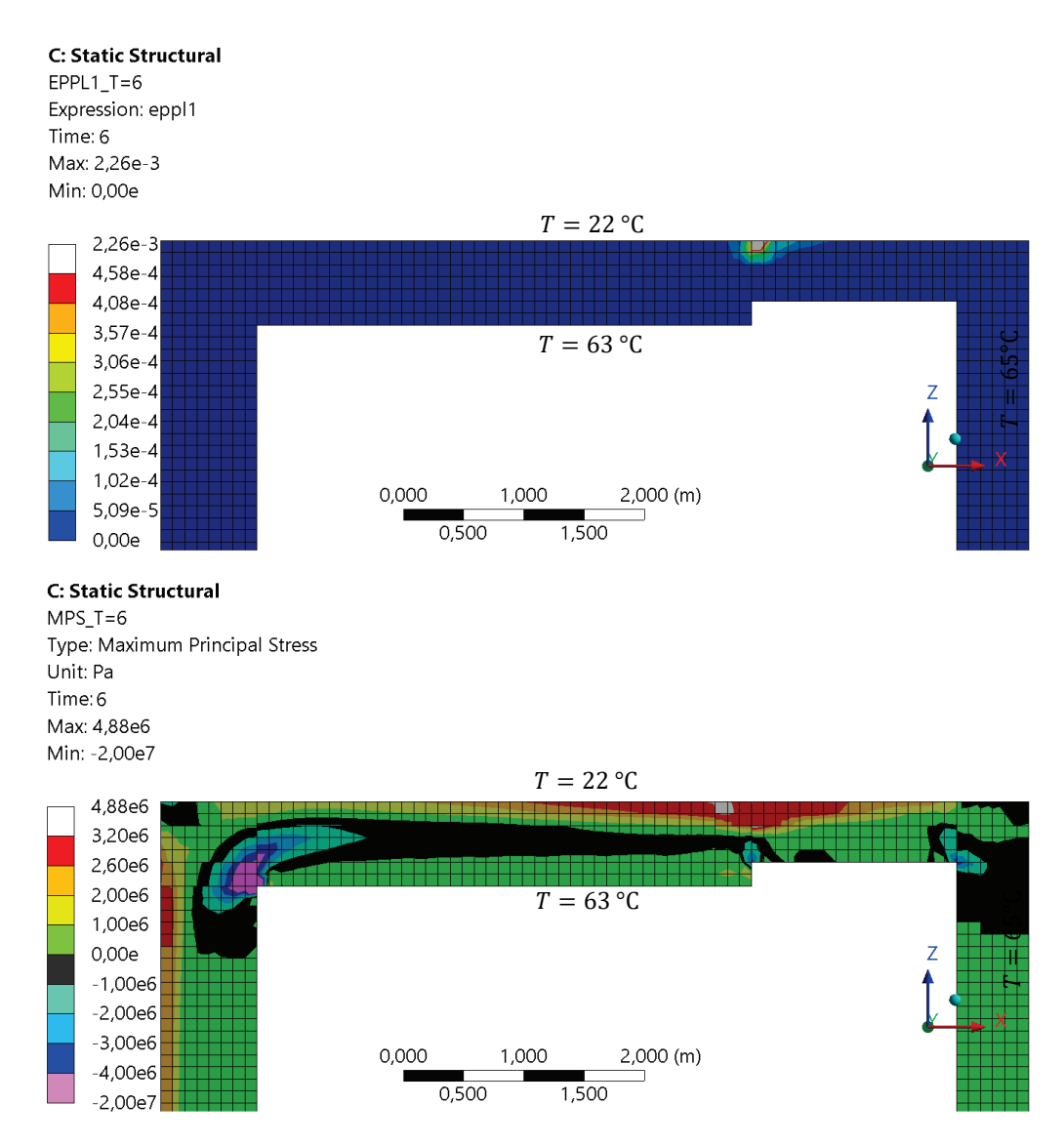


Figure 37. Maximum principal plastic strain and stress distribution for cross-sections for the floor above the studied room at load step 6. The element size is 100 mm.

Let us next consider the effect of creep in the model with a linear temperature distribution. In the scope of this thesis, creep is simply considered by dividing the nominal elastic modulus by $(1+\varphi)$ as shown by Equation (25). The resulting maximum principal plastic strain distributions have the same shapes as those seen in Figure 32, but their magnitudes and especially extents are smaller. For reference, Figure 38 shows the maximum principal plastic strain distribution of the studied room with creep modified modulus of elasticity at load step 6. This simple approach suggest that the creep effect is significant considering the response of a structure to thermal loads that are functions of structural stiffness. Even if creep tends to increase deformations from static loads, it lessens the severity or magnitude of thermal loads.



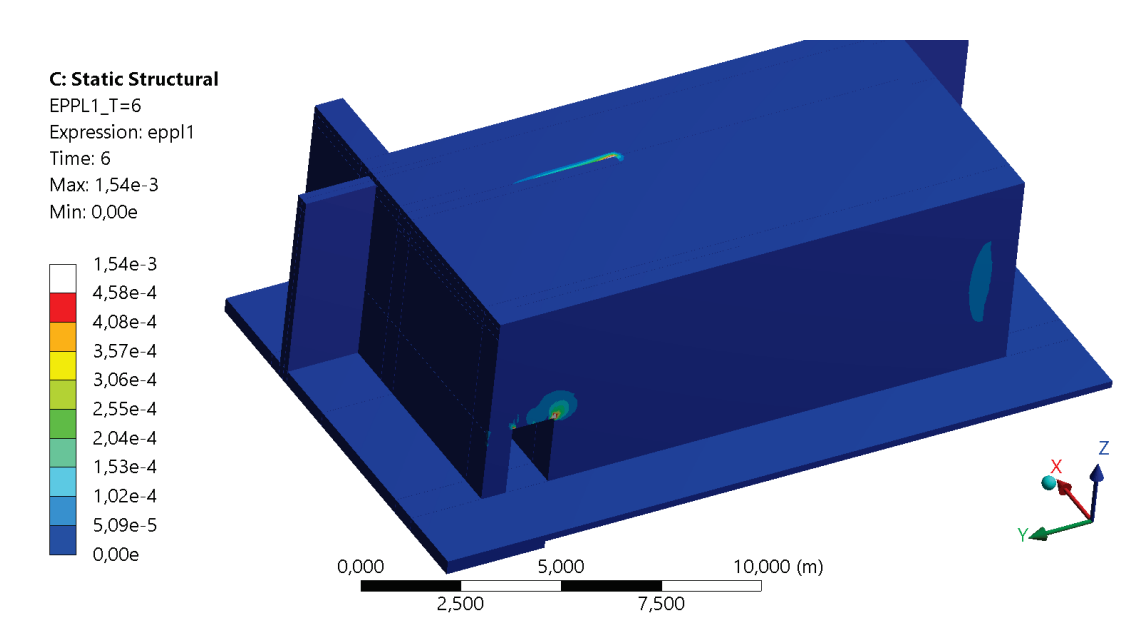


Figure 38. Principal plastic strain distribution with creep modified modulus of elasticity at time step 6. Results coloring is normalized to that with nominal modulus of elasticity.

Next, crack width estimates are given for the local model with linear temperature difference. As with the global model, the maximum stresses in the reinforcement are located where strains are maximized. As the local modelling results had singularities where maximum principal plastic strains had large magnitudes and gradients, it is not reasonable to evaluate crack widths solely based on the maximum stress in the reinforcement. To account for the singularities, crack widths based on both the maximum and an averaged reinforcement stress are calculated. Averaging is performed with some 12 to 20 nearby elements with stresses from at least two rebars (see Annex 3 for more details about averaging).

Detailed crack width calculations are represented in Annex 3 and the results are shown in Table 9. The positions where crack widths are estimated are shown in Figure 32. As shown by Table 9, averaging the reinforcement stress values has an effect on the maximum crack width values, as the averaged values are some 12 % smaller on average. The averaged values are of similar magnitude with the crack widths estimated from the global model, shown in Table 8. On average, the creep effect tends to decrease the crack widths by some 70 %, while the creep modified modulus of elasticity is 43 % of that of nominal.

Table 9. Crack width estimates with linear temperature distribution.

	Load step	Maximum crack width, floor above (mm)		Maximum crack width, left wall (mm)		Maximum crack width, front wall (mm)	
		Averaged	Maximum	Averaged	Maximum	Averaged	Maximum
Nominal modulus of elasticity	4	0.159	0.183	0.091	0.106	0.238	0.281
	5	0.377	0.417	0.303	0.347	0.430	0.510
	6	0.490	0.543	0.472	0.539	0.840	0.945
Creep modified	4	No cracking*	No cracking*	No cracking*	No cracking*	0.055	0.076
modulus of	5	0.080	0.100	No cracking*	No cracking*	0.111	0.155
elasticity	6	0.211	0.253	0.089	0.118	0.322	0.400

^{*}No plastic strains at these positions at the given load step.



All in all, the local model with linear temperature distribution supports the results of global modelling even though some differences were observed regarding the extent of yielding at colder faces and the maximum magnitude of plastic strains. Also, the crack width estimates were of similar magnitude, although the largest crack widths were obtained near the doorway in the front wall which was not a critical position in the global model as the doorway was left unmodelled. Overall, the results suggest that shell elements can estimate the response to temperature differences satisfactorily as compared to solid elements.

5.5 RESULTS FOR NONLINEAR TEMPERATURE DISTRIBUTION

Figure 39 shows the temperature distribution for different time instances in the front wall with temperature conditions corresponding to time step 6, illustrating the development of nonlinear temperature distribution with time. As the figure shows, already around 48 hours the distribution is close to linear and at 96 hours no apparent nonlinearity can be seen even though the equilibrium temperature is not yet reached. Before reaching a linear or close to a linear distribution, the concrete medium close to the warmer surface tends to warm up more rapidly relative to the medium further away from the surface. This results into nonlinearity at the close vicinity of the warmer surface at the early stages of the analysis after which the nonlinearity progresses towards middle of the section as the development continues and the distribution approaches a linear one.

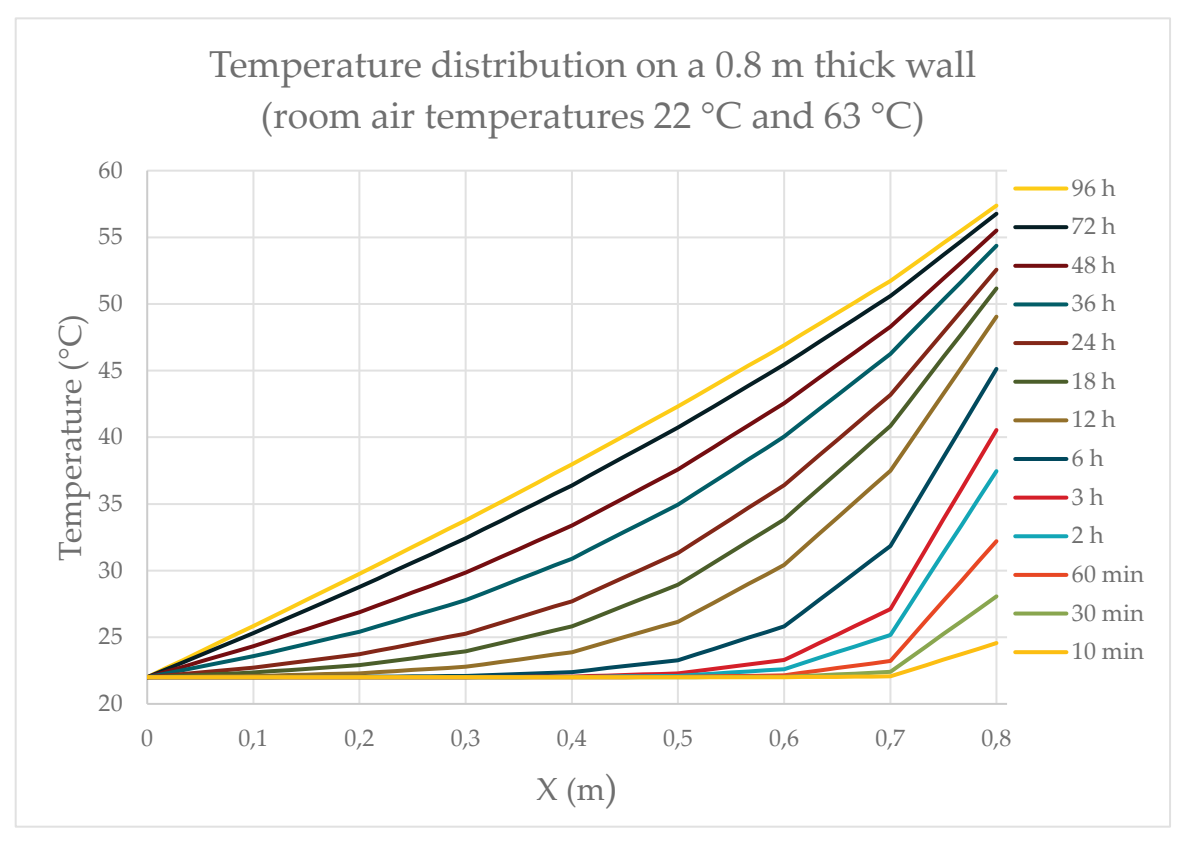


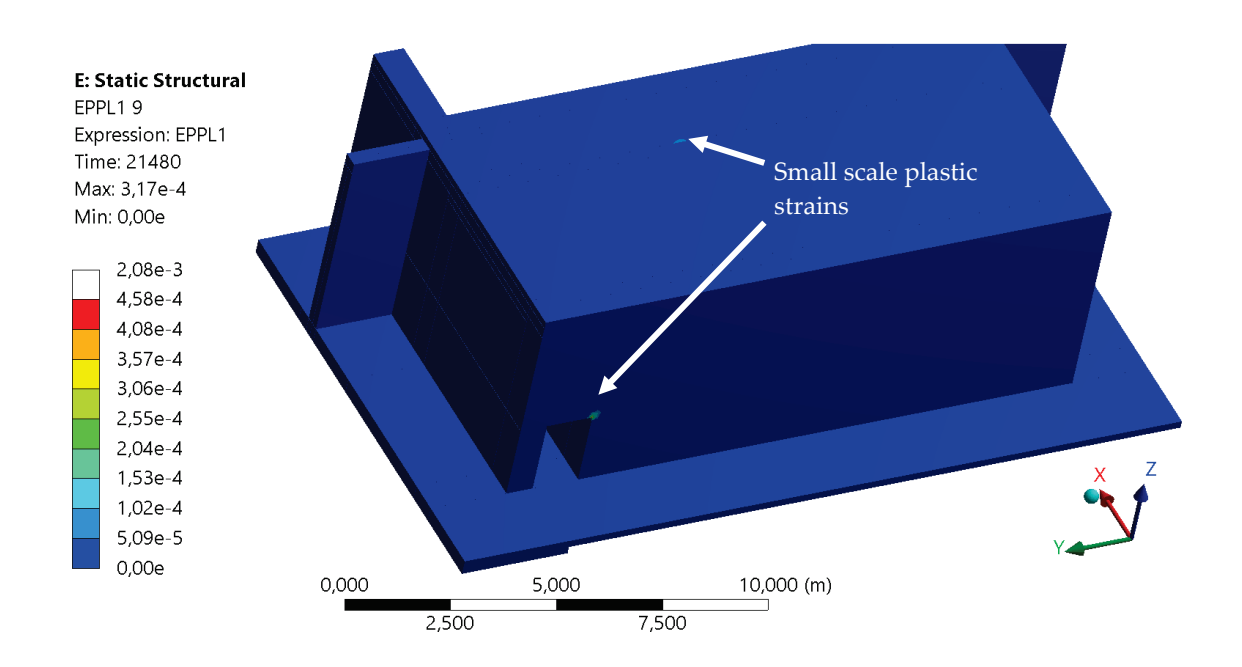
Figure 39. Development of temperature in a 0.8 m thick wall. The temperatures are retrieved from the front wall (with the doorway) of the local model.



In global modelling, a hypothesis was made that continuity thermal stresses dominate over the primary thermal stresses due to the monolithic nature of the reactor building. The results of the local analyzes support this hypothesis. Even though nonlinear temperature distributions are present, as shown by Figure 39, the response of the structure does not considerably differ from the analysis made with a linear distribution. This can be seen in the results in several ways. Figure 40 and Figure 41 show the maximum principal plastic strain distribution for the time instances of 6 hours (at the onset of yielding) and 96 hours. Firstly, the positions where plastic strains are maximized are the same as with linear temperature distribution, even at the onset of plastic strain development. Due to the perfect bond between reinforcing steel and concrete, this effectively means that the stresses in the reinforcement are also maximized in the same positions. However, during the very early time instances (first hour or two) the positions where stresses in the reinforcement are maximized differ slightly from those with larger time instances or linear temperature distribution. At 2 hours, the maximum temperature is only some 32 °C which means that the overall effect of temperature (both continuity and primary stresses) is not significant. After 2 hours, the positions for maximum stresses in reinforcement are exactly the same as with linear temperature distribution. Secondly and thirdly, the magnitudes of maximum principal plastic strain do not differ notably, and the extent of plastic strains is similar. These findings suggest that primary thermal stresses only affect the solution during the first hours after maintenance ramp-up after which the thermal stresses are governed by continuity stresses.

The results for temperature boundary conditions corresponding to load steps 4 and 5 have similar findings as discussed above. As the structural response to conditions of load step 6 is the most severe and the nonlinear temperature distribution has no significant effect on the response of the structure, the results from load steps 4 and 5 are not presented separately. Furthermore, crack width calculations are not performed again as they are equal or close to equal to those with linear temperature distribution.





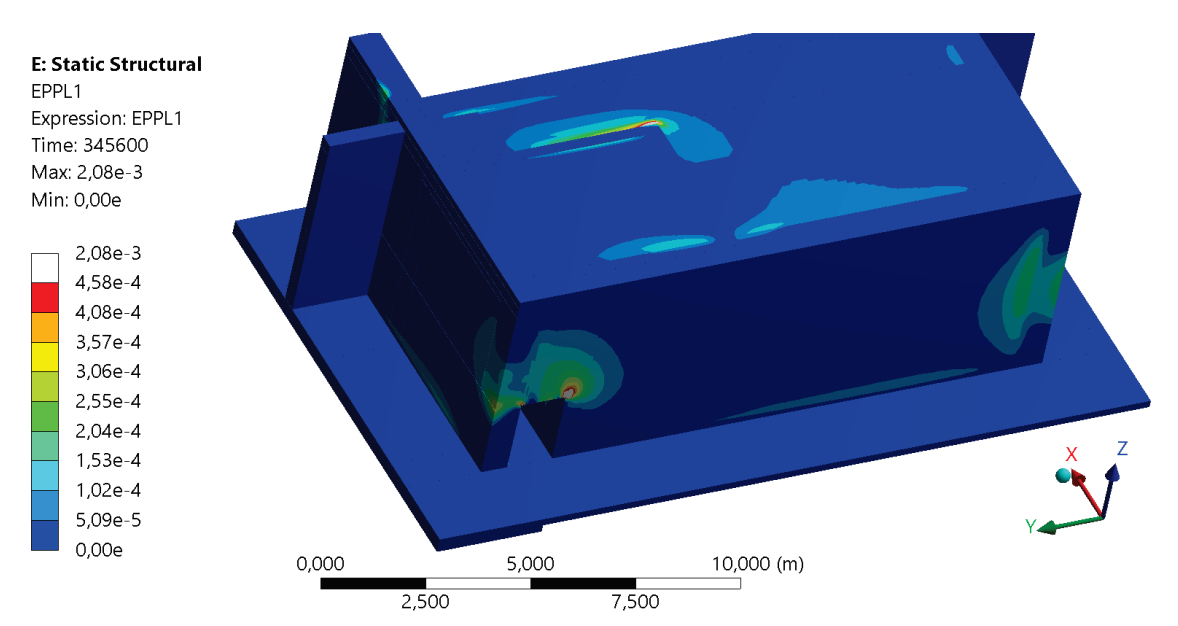


Figure 40. Maximum principal plastic strain distribution at 96 hours.

Instead of crack width calculations, let us consider different strain components present during nonlinear temperature distribution (early time instances) and linear temperature distribution (later time instances). Even though the nonlinearity of temperature distribution is not significant here, it may be more severe with larger temperature differences or when concrete is in touch with fluids that have larger convective heat transfer coefficient. As discussed in Part 3.4, thermal loads are induced by the difference between thermal strain and realized strain. With the strain components given by Ansys (2020), total mechanical strain represents the



realized strain defined as the sum of elastic strain, plastic strain and creep strain. Without creep strain, it reduces to the sum of elastic and plastic strain. Thermal strain is defined in Equation (12). In following figures "EPTO" refers to total mechanical strain, "EPTH" to thermal strain, and "EPEL" to elastic strain as per the naming used by Ansys. Letters X, Y or Z in the end of those strain components refer to the global coordinate direction in which the strain component is measured. To analyze the different strain components, let us consider two paths: one where high plastic strains occur at later time instances (Position 1) and for reference one with lower magnitudes of plastic strains (Position 2). These positions lie on the wall with the doorway as shown in Figure 42 with the paths being parallel to the wall thickness (X axis).

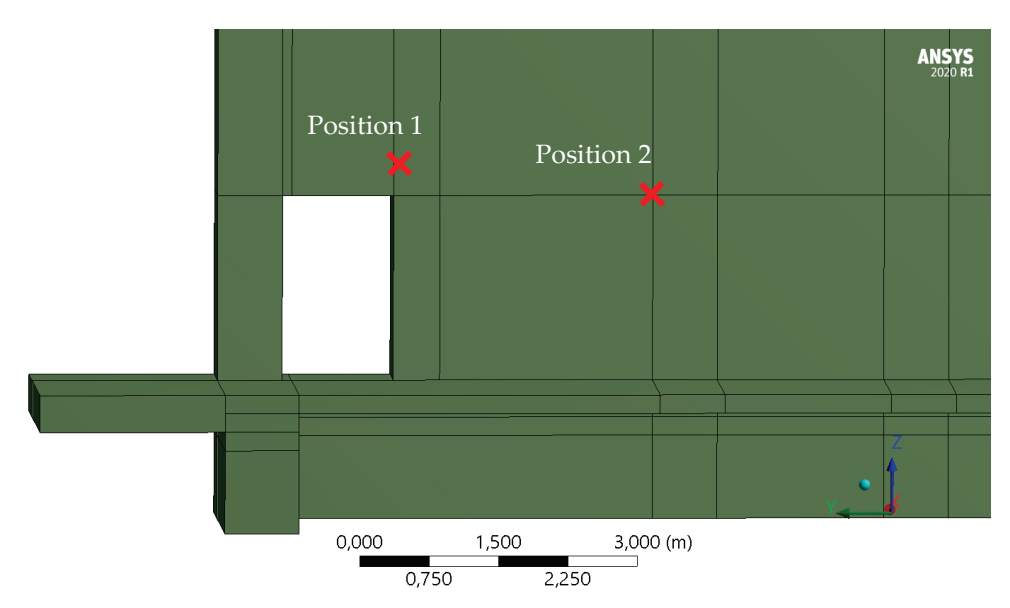


Figure 41. Positions for strain component consideration. Position 1 is offset from the corner of the doorway to account for the effect of geometric nonlinearities. The wall thickness is 800 mm. X axis is parallel to the thickness of the wall.

Figures 43 to 45 present the strain components in Position 1 for time instances of 1 hour and 96 hours. Considering first the strain components at 1 hour, the figures show that the total (mechanical) strain (EPTO) is equal to elastic strain (EPEL) meaning that no yielding is expected at 1 hour. The strain component distributions in Y and Z directions (perpendicular to the thickness direction) are effectively the same, having a relatively large compressive total strain near the warmer face. This is intuitive considering the idea in Figure 20. The nonlinear temperature distribution induces a positive thermal strain on the warmer face meaning that a relatively large positive difference between the thermal strain and total strain ($\Delta \epsilon$ = $\varepsilon_T - \varepsilon = \text{EPTH} - \text{EPTO} > 0$) occurs. This induces compressive thermal stresses to the warmer surface. Near to the colder surface, the magnitude of thermal strains is effectively zero. However, the total strain is positive meaning that $\Delta \varepsilon < 0$ which induces tensile thermal stresses to the colder surface. However, the magnitude of total strain at this stage is so small that the tensile stresses are not severe. In the X direction, $\Delta \varepsilon > 0$ through the whole thickness meaning compressive thermal stresses are induced in that direction. The stresses are again largest near the



warmer surface. Unlike in Y and Z directions, the total strain at the warmer surface is positive in the X direction which can be explained by the lack of restraint in that direction.

Figures 43 to 45 show that at 96 hours, the thermal strain is close to linear meaning that the temperature distribution has also linearized at this stage. In Y and Z directions, the shapes of the strain component distributions are again similar to each other, and the total strain is positive near the colder surface. At this time instance, the positive total strains are dominated by plastic strains as the elastic strains are notably smaller than the total strains. Note that when plastic strains are present, the strain difference Δε is not a direct measure of the magnitude of thermal stress anymore. In Y and Z directions, the depth where $\Delta \epsilon$ is zero tends to move closer to the colder surface as compared to the early time instances. At 1 hour, the zero positions are at X = 0.62 m and X = 0.50 m in Y and Z directions, respectively. At 96 hours, the zero positions are at X = 0.35 m and X = 0.25 m. These results suggest that when nonlinear temperature distributions are present, the depth where tensile thermal stresses occur, perpendicular to the thickness direction, is increased as compared to a situation with a linear temperature distribution. In the X direction, the total strain is positive at the warmer surface and negative at the colder surface. As with early time instances, Δε exceeds zero through the whole thickness.

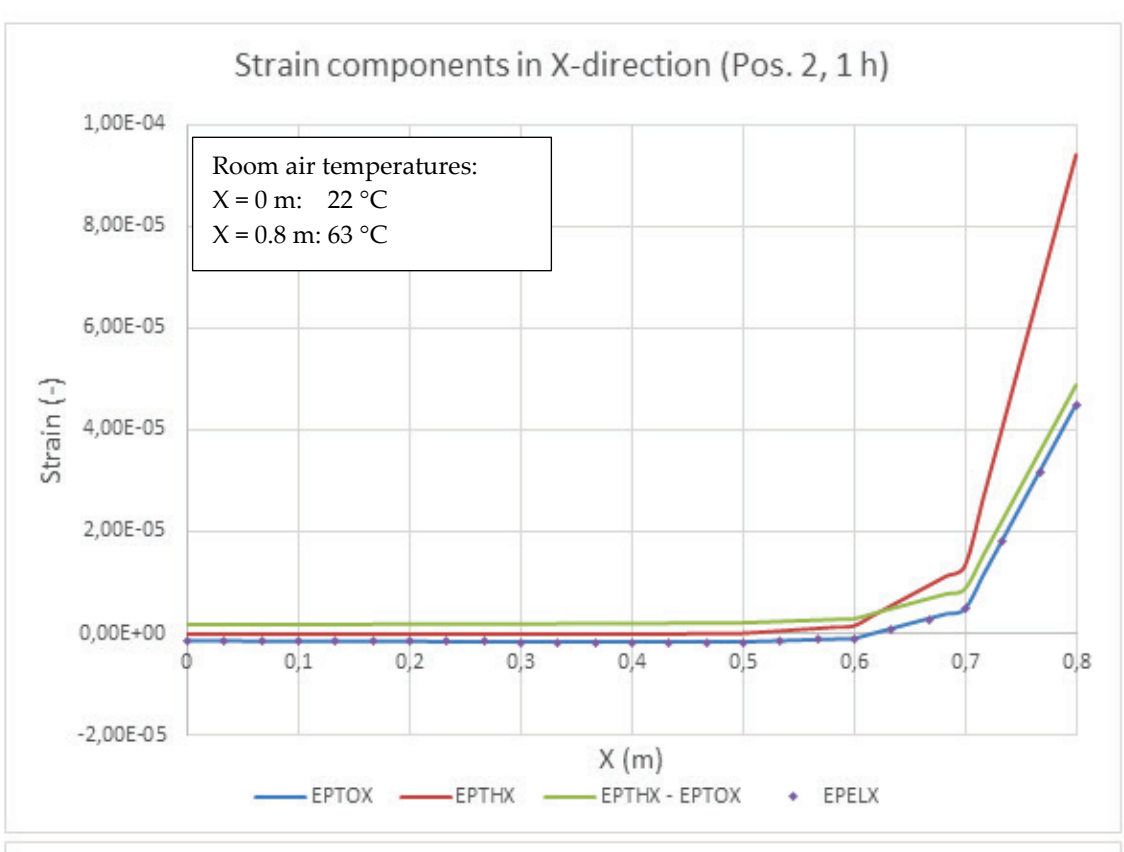
For reference, Figure 46 shows the stresses in the Y and Z directions as a function of strain difference $\Delta\epsilon$ in Position 1 at 96 hours. The results show that $\Delta\epsilon < 0$ and $\Delta\epsilon > 0$ yields tensile and compressive stresses, respectively, as assumed in previous analysis. However, in the Y direction the curve seems to be offset by a strain of some 10^{-4} to the right compared to a typical uniaxial stress-strain curve. This offset can come down to factors such as triaxiality of the stress state or Ansys formulation of directional stresses and strains on a path object. All in all, relating $\Delta\epsilon$ to the resulting stress state generally yields results that are intuitive, and measuring the thermal stress state with $\Delta\epsilon$ is estimated to be a reliable measure in this analysis.

Figure 47 shows the strain component distribution in Position 2 at 96 hours in the X, Y and Z directions. At 1 hour, the distributions are similar to those of Position 1 and are therefore not presented separately. As the figure shows, the total strain corresponds almost exactly to the elastic strain in all directions meaning that plastic strains are negligible. It is notable that the zero positions of $\Delta\epsilon$ (at X = 0.12 m) in Y and Z directions are even closer to the colder surface compared to Position 1. This means that the depth of tensile thermal stresses relative to the depth of compressive thermal stresses is small. Even at Position 1 during larger time instances, the zero position of $\Delta\epsilon$ was such that the depth of tensile thermal stresses is smaller than the depth of thermal compressive stresses. This can be interpreted so that the problem is not fully explainable by pure bending where in case of linear-elasticity the neutral axis was positioned to the center of the section. This observation magnifies the importance of choosing the reference temperature for thermal strains correctly as changing the reference temperature alters the strain distribution and corresponding stresses.



Summarizing, the transient effect induces notable nonlinearity during the first day after maintenance ramp-up, especially during the first hours. However, the response of the structure does not significantly differ from a situation where a linear temperature distribution is induced directly without considering time. This is because during the early time instances, when nonlinearity is the most apparent, the temperature differences are relatively small to induce any significant thermal stresses. Considering also the conservative manner of applying the temperature boundary conditions, it is estimated that the transient effect after maintenance ramp-up is not important on walls or floors warmed by the surrounding air in the reactor building. Even though the nonlinearity of temperature distribution had no major importance to the problem at hand, it had interesting features including increased depth of tensile stress in the directions perpendicular to the thickness and relatively large strain difference $\Delta\epsilon$ at the warmer surface that induces compressive stresses.





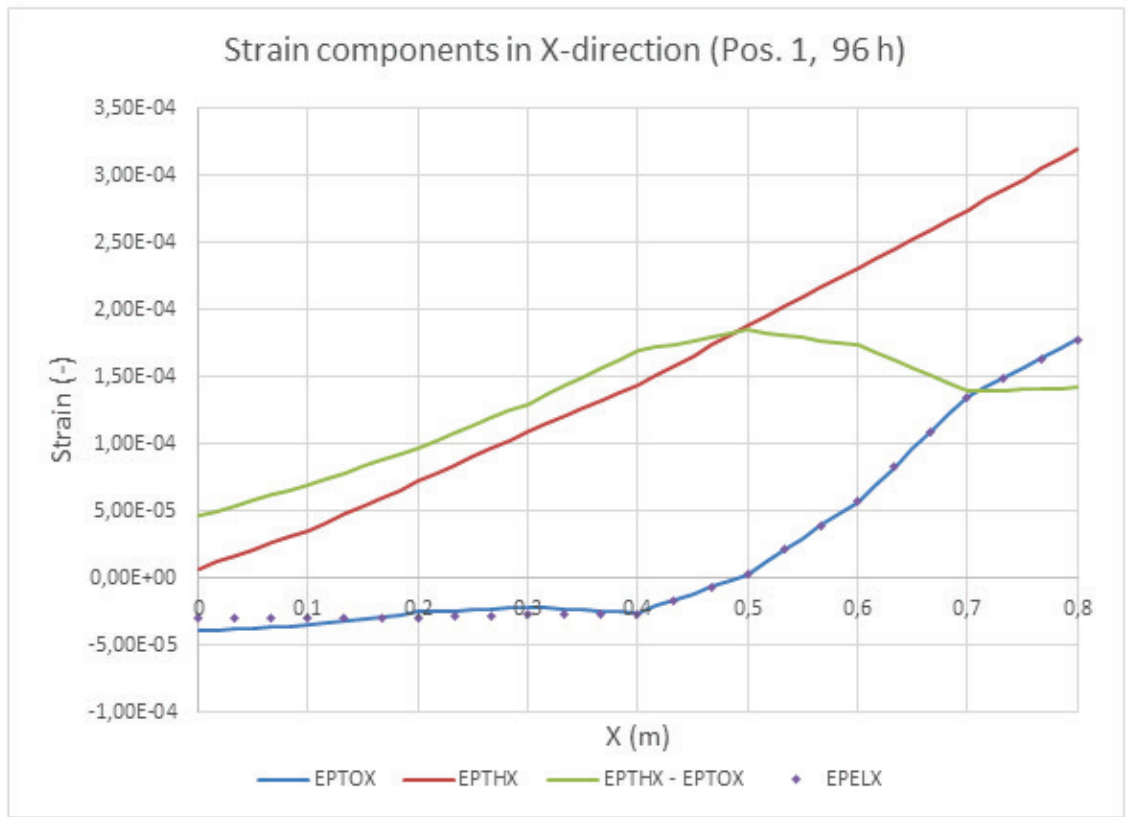
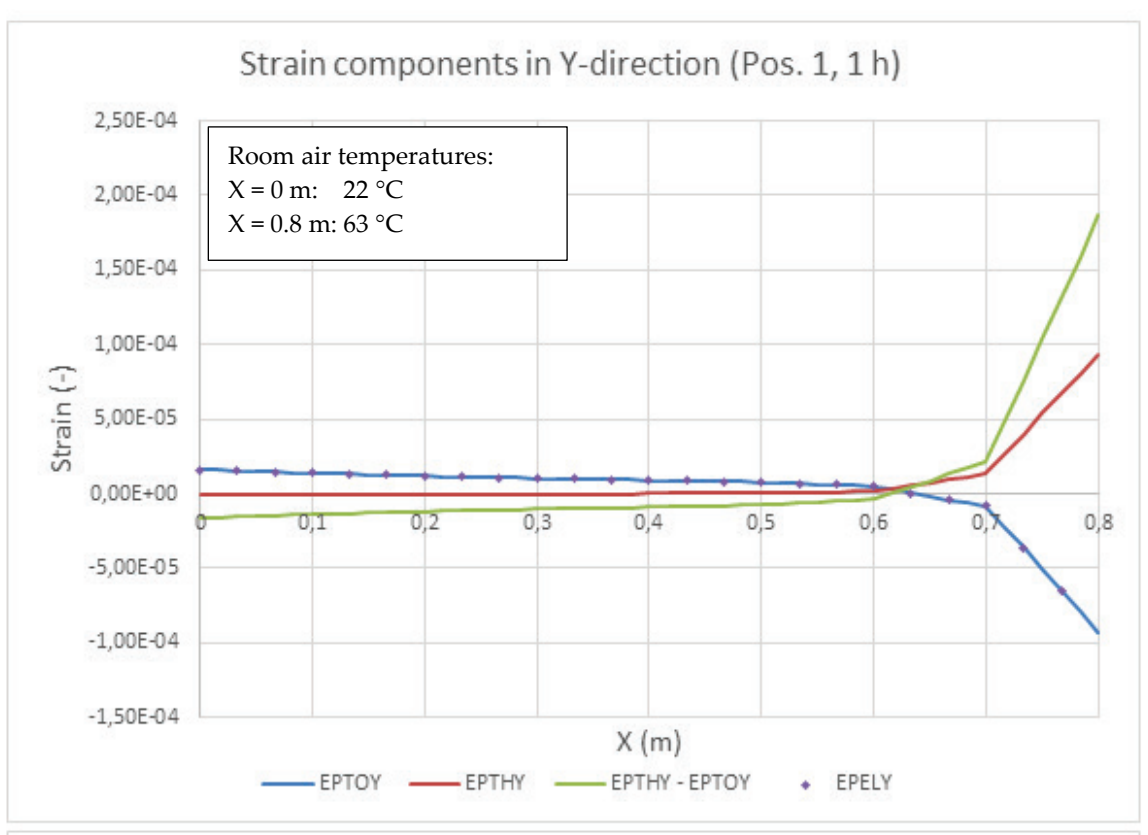


Figure 42. Strain component distribution in Position 1 in X-direction at 1 hour and 96 hours.





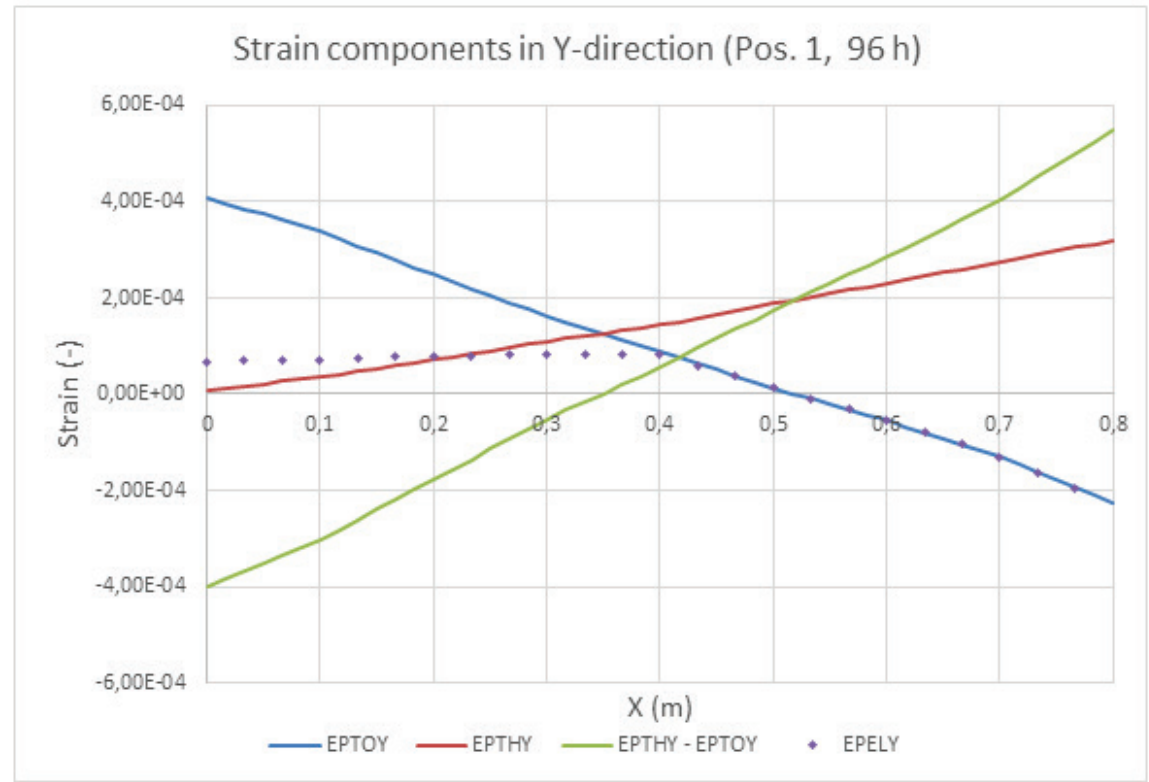
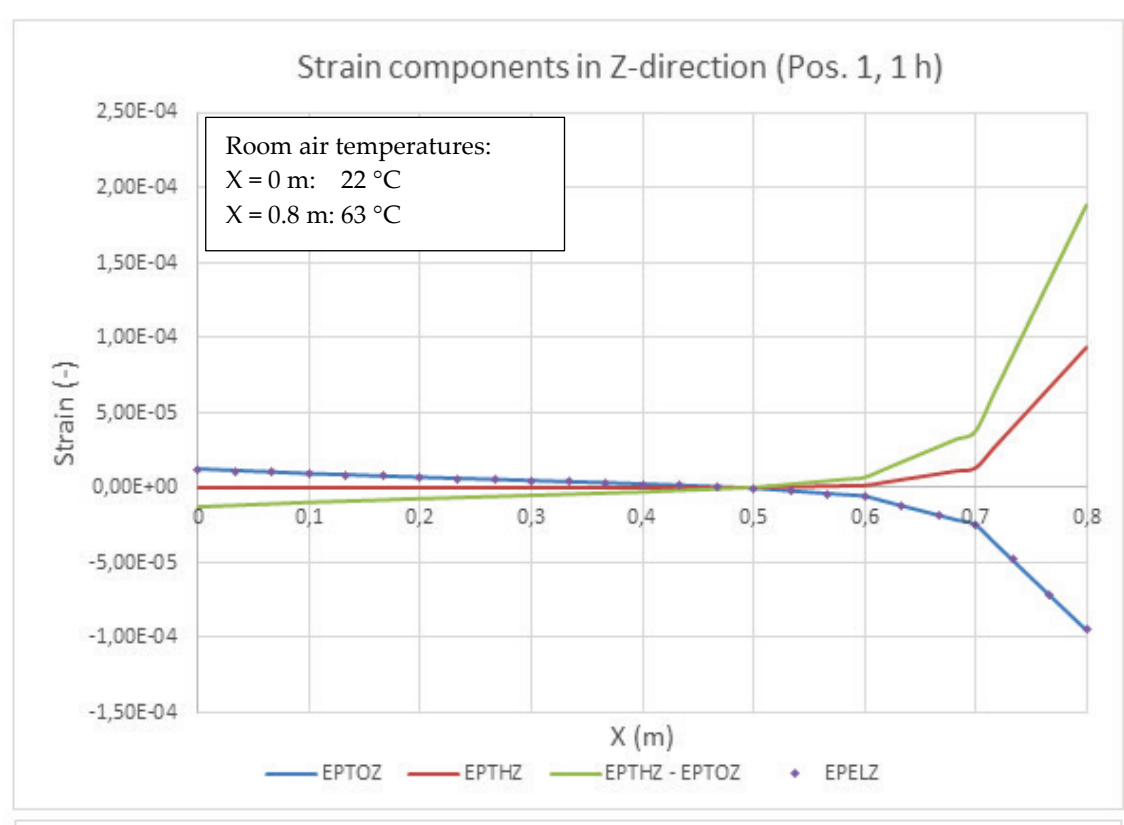


Figure 43. Strain component distribution in Position 1 in Y-direction at 1 hour and 96 hours.





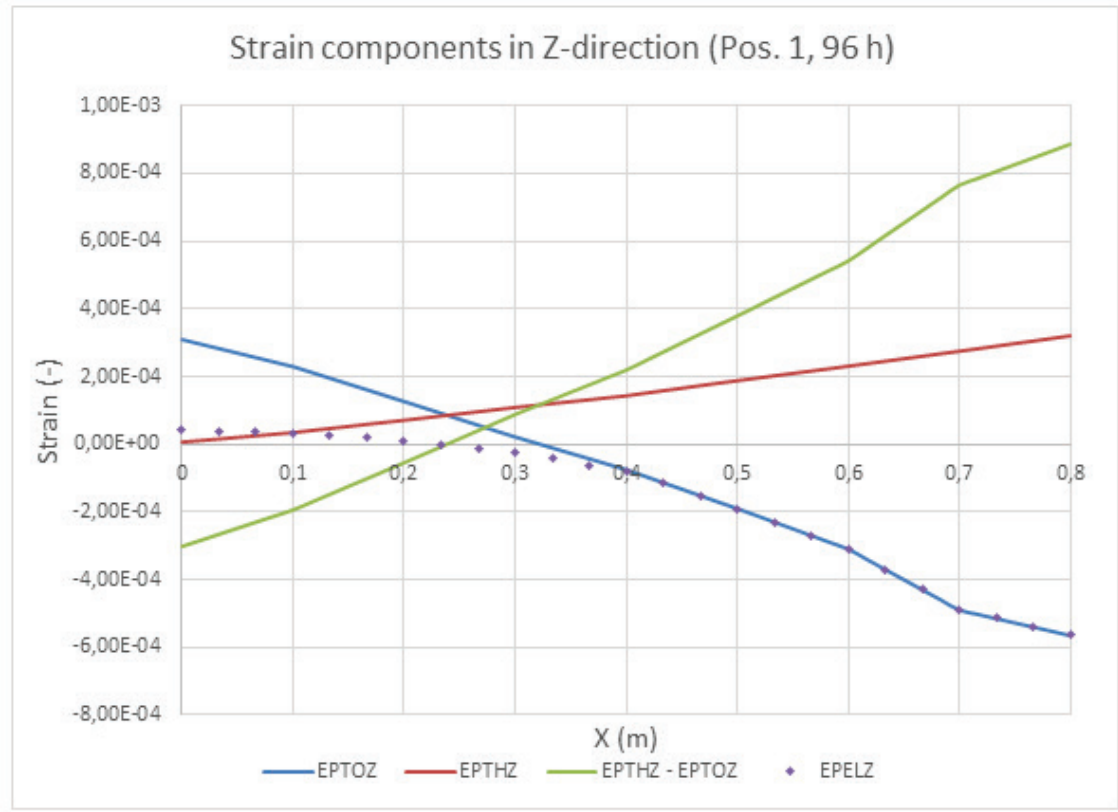
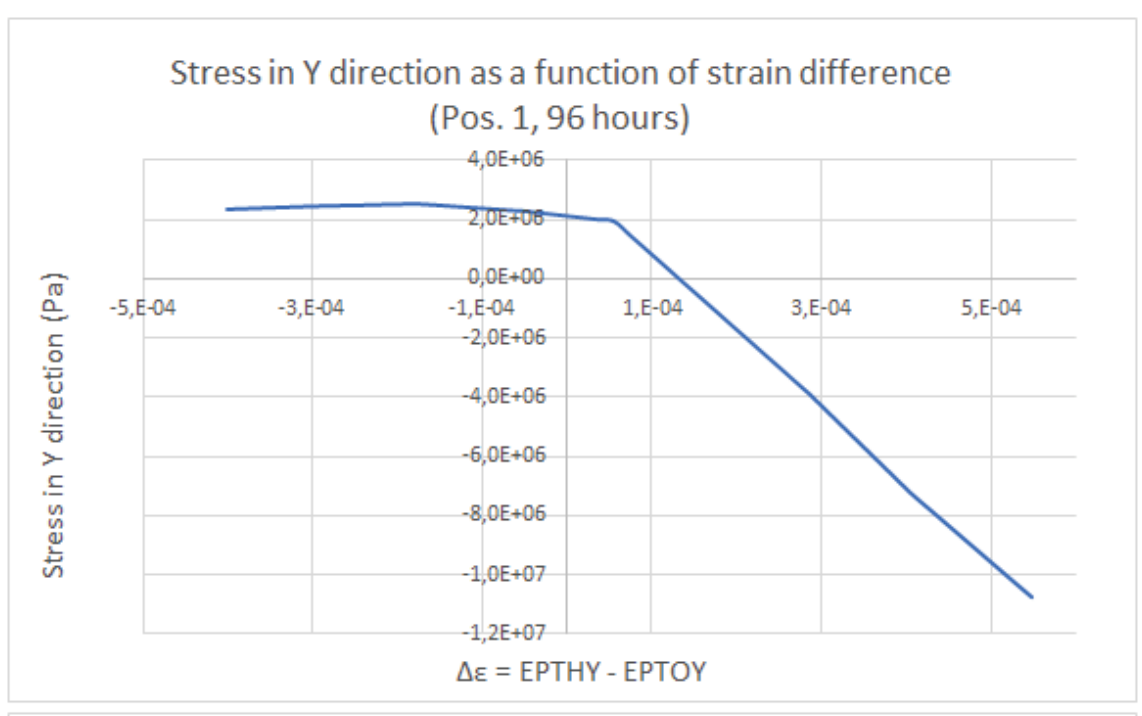


Figure 44. Strain component distribution in Position 1 in Z-direction at 1 hour and 96 hours.





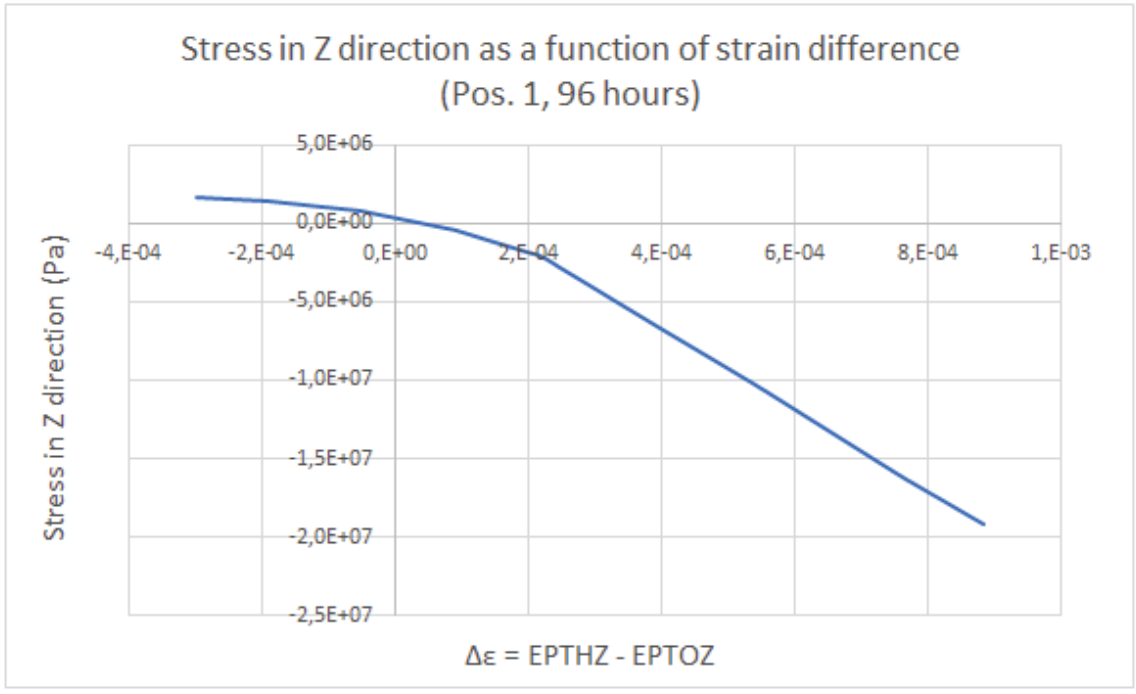


Figure 45. Stress as a function of strain difference $\Delta\epsilon$ in Y and Z directions in Position 1 at 96 hours.

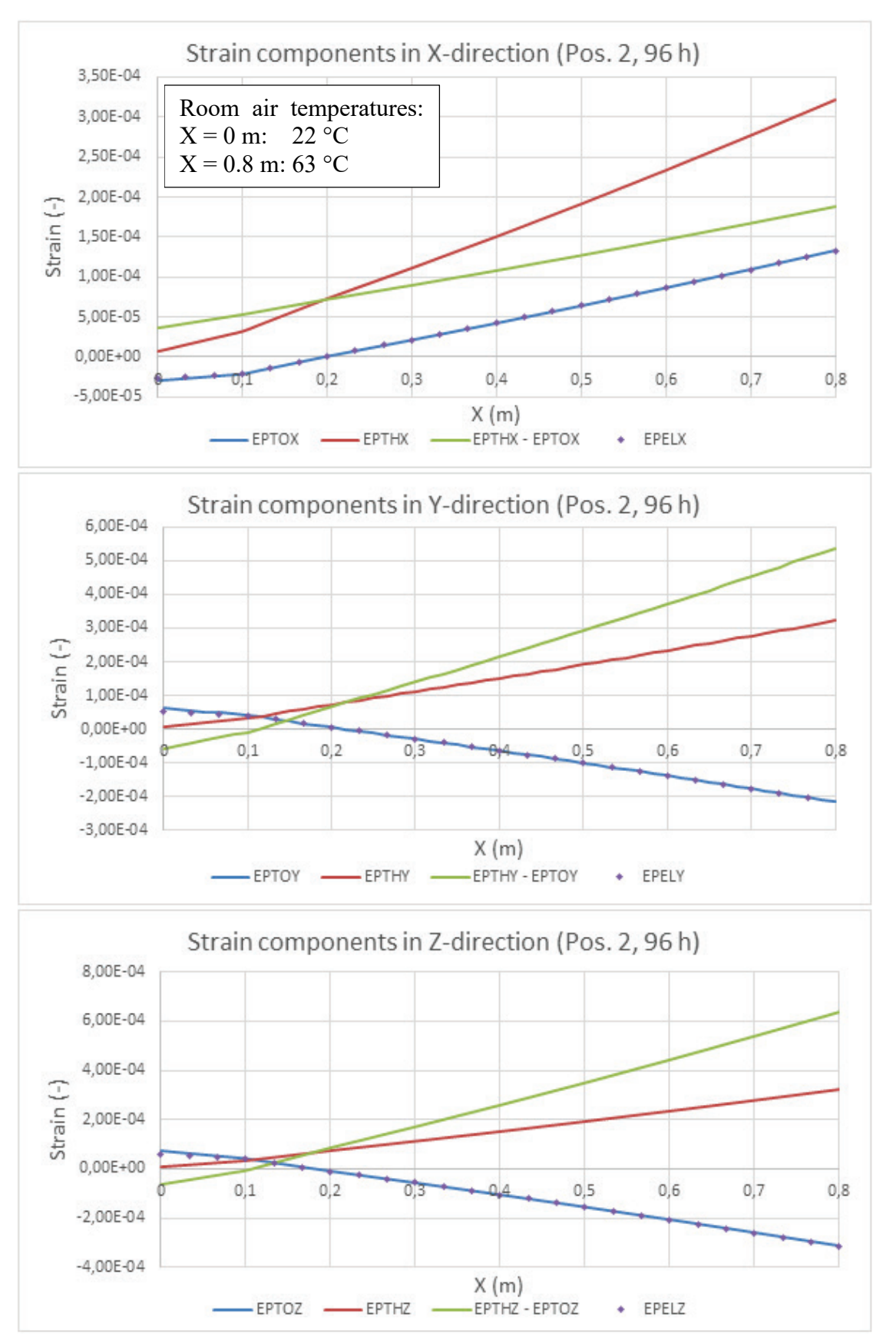


Figure 46. Strain component distribution in Position 2 in X, Y and Z directions at 96 hours.



6 Error analysis, conclusions and future research

6.1 SOURCES OF ERROR

The problem at hand is in its nature very complex and therefore contains numerous sources of errors. The errors can be divided for example into simplification errors and modelling errors, although these error types can also overlap each other. Some sources of simplification errors are induced by the assumed ideal-plasticity in concrete, equal thermo-mechanical properties between concrete and reinforcement, by the assumption of temperature-independent material parameters, and by a reference temperature of 22 °C for thermal strains.

The effect of ideal-plasticity as opposed to cracking can create localized errors in areas where crack openings occur. However, considering that the local model had numerical singularities near corners (where possible cracking is expected to occur due to thermal loads) applying a cracking behavior would likely increase the magnitudes of the singularities or simply yield non-converging solutions, as was the case here. A viable option could be to make a localized model of the local model, where the geometry is substantially smaller, corners are rounded, and the mesh does not need to be as uniform as in the local model. With smaller geometry, the analysis would not be as computationally challenging possibly allowing for a converging solution with slowly ramped-up loading, smaller time steps or other methods concerning convergence of nonlinear FEA. However, a localized model of the local model does not guarantee converging solutions and it might fail to consider macro-scale phenomena.

The ideal-plasticity assumption also induces some arbitrarity when considering the reinforcement stresses for the crack width calculations. As presented in Appendix 3, tensile forces in concrete are manually transferred to the reinforcement in order to account for tensile loss of capacity of concrete. There are numerous methods to perform the force transfer, and the results can vary between these methods. However, physical reasoning was given to the method chosen in this study. Overall, considering the numerous possibilities to perform the force transfer, it can be regarded as a source of error.

The assumption of equal thermo-mechanical properties between concrete and reinforcement, mainly coefficient of thermal expansion and same heat transfer properties, can induce errors in the vicinity of the rebars. As shown in Table 2, the coefficient of thermal expansion of concrete can be some half of that of reinforcing steel. Should the difference be that great, tensile stresses are induced around the reinforcing bar to concrete if a positive deviation from the reference temperature occurs. These effects are omitted as such a large difference is not expected. If the coefficient of thermal expansion of concrete did adopt the minimum value given by Eurocode, the thermal stresses by continuity and primary thermal stresses could hypothetically decrease significantly, resulting into a win-lose situation between the different stress components.



Regarding the temperature-independent material properties, Table 2 suggests that the change of modulus of elasticity of concrete can vary anywhere between 2 % to 30 % between the studied temperature range. In the most extreme case where modulus of elasticity drops by 30 %, with linear interpolation the average modulus of elasticity is 85 % of that of nominal between 20...65 °C. For reference, the creep modified modulus of elasticity used was 13 GPa (43 % of nominal) which resulted into a decrease of some 70 % in crack width estimates. Although only a crude estimate, linear interpolation suggests that crack widths decrease by some 18 % if the most extreme temperature dependence on elastic modulus is assumed. This can be considered as a significant decrease. However, such a strong temperature-dependency is not expected, and by not decreasing the modulus of elasticity, the crack width estimates and the magnitudes of thermal stresses are more conservative.

The assumption of a reference temperature of 22 °C for thermal strains is likely the most major source of error in the calculations. As shown by Equation (24), a deviation of 10 °C from the reference temperature can already induce tensile stresses equal to tensile strength of concrete. Therefore, deviations between assumed and actual reference temperature can induce notable error in the calculations by altering the strain and stress states as discussed in Part 5.5. Furthermore, the reference temperature can vary within the reactor building which increases the uncertainty.

Sources of modelling errors include differences between the topology of the calculation model and the actual reactor building, assumptions made in loading, and deviations of material parameters from actual values. The models, mainly the global model, do not include any stiffness for example from steel grates or the transversal stiffness from containment building. As the magnitudes of transversal forces are relatively low in the global model, leaving the containment building unmodelled is reasonable. Steel grates and similar can locally restrain deformations of concrete walls and floor and induce thermal stresses that are not accounted for in the calculation models.

In the global model, mechanical loading is set in a global manner, where structural loads are not considered room-by-room (for example, see Figure 19). This makes it easier to set-up loads but simultaneously averages the loads into larger areas, omitting local areas where mechanical loads can have larger impact. Furthermore, determining the magnitudes of mechanical loads is difficult when done in a global manner. These modelling errors can affect the results concerning the severity of thermal loads to mechanical loads. To consider the magnitude of this error, one could for example compare the cracking positions in the reactor building to the modelling results. Such a comparison would also yield information on the conservatism of the modelling results, i.e. are the results on the safe or non-safe side.

In the global model it was assumed that the distance between the face of a section and the reinforcement layer is equal to $10\,\%$ of the thickness of section. This assumption is sensible on sections that are moderately thick (say $500\,$ mm and under) after which the concrete cover is likely too large. In the global model, sections under $500\,$ mm thick comprise about $70\,\%$ of the concrete volume meaning



that the assumption is reasonable for the majority of the sections. In thicker sections with increasing concrete cover, the reinforcement is further away from the most tensioned fiber, assuming bending behavior dominates. However, determining the effect of increased concrete cover on crack width estimates is not straight-forward. Presumably, the reinforcement carries less and concrete more tensile forces according to results of FEA when concrete cover is increased. With increased tension in concrete the extent of plastic strains in concrete is likely increased meaning that more forces are transferred to reinforcement according to the process presented in Annex 3. This balances the modelling error when concrete cover is larger than in reality. Furthermore, increasing the concrete cover also increases the maximum crack spacing which is directly proportional to the magnitude of crack width estimate as shown by the equations in Annex 1.

Apart from the compressive strength of concrete, the material parameters (namely thermal properties) were determined by using estimates given by EC2 and by using common material values. Material parameters affecting the results the most are modulus of elasticity, coefficient of thermal expansion and tensile strength of concrete. Modulus of elasticity and coefficient of thermal expansion are directly related to the magnitude of thermal stresses (shown for example by Equation (18)), whereas the tensile strength affects the magnitude and extent of cracking. Assuming a perfect bond between reinforcement and concrete, the magnitude of cracking directly affects the magnitudes of stresses in reinforcement that affect the crack width estimates of EC2 method. For more precise results, the material parameters should be based on values determined by experiments.

In global models, the extent of yielding was greater than in the local model. This can either mean that the bending stiffness of solid elements in the local model is too high or that it is too low for the shell elements in the global model. To determine if the actual response to thermal loading is closer to that of local or global model or between the two modelling methods, experiments or rigorous study of the mathematics behind the finite elements should be performed.

6.2 CONCLUSIONS AND FUTURE RESEARCH

This thesis aimed to analyze the effect of room temperature differences on the integrity of the reactor building of Olkiluoto 2 nuclear power plant in the temperature range of 20...65 °C. Four different modelling goals were defined to tackle the problem (see Part 4.2). Results of Goal 1 suggest that the thermal stresses in said temperature range can induce localized cracking in the intersections of structural pieces. With current temperature conditions in the reactor building, the crack width estimates generally lie under 0.2 mm. When the temperatures are increased from the current temperatures, the crack width estimates exceed the 0.3 mm reference value given by Eurocode 2 but generally stay well under 1.0 mm.

Results of Goal 2 suggest that thermal loads can induce tensile stresses and yielding that exceed those induced by mechanical loads. Contrary to stress state caused by mechanical loads, thermal stresses are mostly induced to the intersections of structural pieces where deformations are restricted. When a non-constant temperature distribution is present in a wall or floor section, tensile thermal loads are induced to the colder face making that face prone to cracking.



However, the tensile stresses are concentrated near the colder face in the thickness-direction, and therefore possible cracks are shallow. Thermal stresses may also be induced to sections that are intersected by structural pieces subject to thermal elongation. However, the number of such conditions was minimal with the given temperature boundary conditions in the reactor building.

Results of Goal 3 indicate that primary thermal stresses induced by nonlinear temperature distributions have no significant impact on the thermal stress state. This suggests that continuity thermal stresses dominate the thermal stress state, which is intuitive considering the monolithic nature of the reactor building. Therefore, maintenance ramp-ups do not require special attention on concrete faces that are warmed by the room air when the room temperature is between 20 to 65 °C.

Results of Goal 4 suggest that concrete creep has a positive effect regarding the magnitudes of thermal stresses. Creep effect decreases nominal modulus of elasticity which effectively decreases the magnitude of thermal stresses. On average, the creep effect decreased crack widths by some 70 %. Combining the results of the modelling goals (relatively small crack widths, localized cracks, shallow tensile stress depths and the positive effect of creep) implies that thermal loads in the studied temperature range do not critically impair the integrity of the reactor building in terms of cracking. However, if thermal loads are accompanied by large tensile stresses from mechanical loads the combined effect should be considered in design. Here it should be noted that this study included no predefined criteria that determines if the integrity is impaired or not, and the verbal estimates made here are based on the assessment made by the author of this study.

In addition to Goals 1 to 4, this thesis studied the temperature-dependency of the thermo-mechanical properties of concrete between 20 and 65 °C, mainly by referring to EC2. Most notable temperature-dependency concerned the modulus of elasticity, compressive strength and compressive strain corresponding to compressive strength. Related to the problem at hand, modulus of elasticity is of major importance, and it reported decreases between 2 % and 30 % in the temperature range. Thermal properties showed no considerable temperature-dependence, but coefficient of thermal expansion and thermal conductivity showed significant discrepancy in magnitudes for example due to different aggregate types.

Finally, modelling the problem with both shell and solid elements generally showed good agreement with each other. Both global and local model were able to capture the thermal loads so that the responses between the models were similar, even though differences in the extent and magnitude of concrete yielding were observed. Furthermore, both models yielded crack width estimates that were of similar magnitudes, which increases the credibility of those estimates. These observations also imply that shell elements can be used to model temperature related problems with satisfactory precision and reduced computational effort compared to solid elements.

Due to the complexity regarding thermal stresses, there are numerous possibilities for future research including increased maximum temperature, effect of reference



temperature, or a more sophisticated study of creep. The maximum temperature could be increased for example to 90 °C. However, attention should be given to possible long-term microstructural changes, temperature-dependency of thermomechanical properties and softening behavior of concrete if the temperature is increased. Coupled with increased temperature, the nonlinearity of temperature distribution could have a more significant effect if concrete faces were imposed to a larger convective heat transfer coefficient, for example due to increased air velocity or if concrete was in touch with water.

Studying the effect of changing the reference temperature for thermal strains could yield interesting results as the reference temperature has a significant importance on the strain and stress distribution of wall or floor sections. Thus, changing the reference temperature could notably alter the results.

The creep effect was considered in a simplified manner in this thesis with only changing the modulus of elasticity of concrete. As creep is a time-dependent property, a large time-scale finite element analysis with suitable creep models should be performed to yield a better representation of the creep effect. Performing such an analysis would link the development of creep strains to the development of thermal load magnitudes in a more sophisticated manner as compared to the method used in this study. Furthermore, if such an analysis was to be compared to monitored strains and loading, the creep effect could be studied with even more precision.



References

Suomen virallinen tilasto (SVT). 2018. *Sähkön ja lämmön tuotanto* [online publication, referenced 14.7.2020]. ISSN=1798-5072. Helsinki: Tilastokeskus. Available on: http://www.stat.fi/til/salatuo/2018/salatuo_2018_2019-11-01_tie_001_fi.html

EN 1992-1-1. 2005. Eurocode 2: Design of concrete structures. Part 1-1: general rules and rules for buildings.

Vecchio, F.J. 1987. *Nonlinear Analysis of Reinforced Concrete Frames Subjected to Thermal and Mechanical Loads*. In: ACI Structural Journal, 84.6, pp. 492-501. DOI: 10.14359/2750.

Teollisuuden Voima Oyj. 2013. *OL1&OL2 Nuclear power plant units*. Available on: https://www.tvo.fi/en/index/news/publications.html.

Bazant, Z.P., Jirasek, M. 2018. *Creep and Hygrothermal Effects in Concrete Structures*. Dordrecht, Netherlands: Springer. ISBN: 978-94-024-1138-6.

Ashar, H., Scott, B., Artuso, J.F., Stevenson, J.D. 2009. *Code for Concrete Reactor Vessels and Containments*. (Companion Guide to the ASME Boiler and Pressure Vessel Code, Volume 1, 3rd ed.). DOI: https://doi.org/10.1115/1.802694.ch14.

Teollisuuden voima Oyj. 2020. *Plant units* [online publication, referenced 10.7.2020]. Available on: https://www.tvo.fi/en/index/production/plantunits.html.

Teollisuuden Voima Oyj. 2007. *Nuclear power plant units Olkiluoto 1 and Olkiluoto 2.* Available on: https://www.tvo.fi/en/index/news/publications.html.

Wight, J.K., MacGregor, J.G. 2009. *Reinforced concrete: mechanics and design*. 6th ed. Upper Saddle River, New Jersey, USA: Pearson Education. ISBN 0-13-217652-1.

Hind, M.K., Mustafa, Ö., Talha, E. 2016. A Review of Nonlinear Finite Element Analysis of Reinforced Concrete Beams Retrofitted with Fiber Reinforced Polymers. In: Journal of Advanced Research in Applied Mechanics, 22.1, pp. 13-48.

Chen, H.H., Su, R.K.L. 2013. *Tension softening curves of plain concrete*. In: Construction and Building Materials, Vol. 44, pp. 440-451. DOI: https://doi.org/10.1016/j.conbuildmat.2013.03.040.

Kupfer, H., Hilsdorf, H.K., Rusch, H. 1969. *Behavior of Concrete Under Biaxial Stresses*. In: ACI Journal Proceedings, 66.8, pp. 656-666. DOI: 10.14359/7388.

D.J. Naus. 2010. A Compilation of Elevated Temperature Concrete Material Property Data and Information for Use in Assessments of Nuclear Power Plant Reinforced Concrete Structures. Technical report NUREG/CR-7031, ORNL/TM-2009/175. Oak Ridge National Laboratory.

EN 1992-1-2. 2004. Eurocode 2: Design of concrete structures. Part 1-2: General rules. Structural fire design.



EN 1992-3. 2006. Eurocode 2: Design of concrete structures. Part 3: Liquid retaining and containment structures.

Kassir, M.K., Bandyopadhyay, K.K., Reich, M. 1996. *Thermal degradation of concrete in temperature range from ambient to 315* °C (600 °F). DOI: 10.2172/432891.

Elghazouli, A.Y., Cashell, K.A., Izzuddin, B.A. 2009. *Experimental evaluation of the mechanical properties of steel reinforcement at elevated temperature*. In: Fire Safety Journal, 44.6., pp. 909-919. DOI: https://doi.org/10.1016/j.firesaf.2009.05.004.

Naik, T.R., Kraus, R.N., Kumar, R. 2011. *Influence of Types of Coarse Aggregates on the coefficient of Thermal expansion of Concrete*. In: Journal of Materials in Civil Engineering, 23.4, pp. 467-472. DOI: https://doi.org/10.1061/(ASCE)MT.1943-5533.0000198.

Vodak, F., Cerny, R., Drchalova, J., Hoskova, S., Kapickova, O., Michalko, O., Semerak, P., Toman, J. 1997. *Thermophysical properties of concrete for nuclear-safety related structures*. In: Cement and Concrete Research, 27.3, pp. 415-426. DOI: https://doi.org/10.1016/S0008-8846(97)00033-1.

Schneider, U. 1988. *Concrete at High Temperatures – A General Review*. In: Fire Safety Journal, 13.1, pp. 55-68. DOI: https://doi.org/10.1016/0379-7112(88)90033-1.

EN1991-1-5. 2009. Eurocode 1: Actions on structures – Part 1-5: General actions – Thermal actions.

Thurston, S.J. 1978. *Thermal stresses in concrete structures*. PhD Thesis and Research Report No. 78/21. Department of Civil Engineering, University of Canterbury.

El-Badry, M., Ghali, A. 1995. Control of Thermal Cracking of Concrete Structures. In: ACI Structural Journal, 92.4, pp. 435-450. DOI: 10.14359/993.

El-Badry, M., Ghali, A. 1986. *Thermal Stresses and Cracking of Concrete Bridges*. In: ACI Structural Journal, 83.6, pp. 1001-1009. DOI: 10.14359/2670.

Vecchio, F.J., Sato, J.A. 1990. *Thermal Gradient Effects in Reinforced Concrete Frame Structures*. In: ACI Structural Journal, 87.3, pp. 262-275. DOI: 10.14359/2516.

Santaoja, K. 2014. *Lecture Notes on Continuum Thermodynamics*. 6th ed. Espoo, Finland: Taras. ISBN 978-952-67899-1-0.

Thirumaleshwar, M. 2006. Fundamentals of Heat and Mass Transfer. 1st ed. Pearson India.

ANSYS®Pro Mechanical, Release 20.1, Help System, ANSYS, Inc.

Kedziora, S., Anwaar, M.O. 2019. Concrete-filled steel tubular (CFTS) columns subjected to eccentric compressive loading. In: AIP Conference Proceedings 2060. DOI: https://doi.org/10.1063/1.5086135.

Lee, Y., Choi, M.S., Yi, S.T., Kim, J.K. 2009. *Experimental study on the convective heat transfer coefficient of early-age concrete*. In: Cement & Concrete Composites, 31, pp. 60-71. DOI: 10.1016/j.cemconcomp.2008.09.009.



Table of Annexes

- Annex 1. Crack width calculations according to Eurocode 2 Part 1-1
- Annex 2. Crack width calculations (Global model)
- Annex 3. Crack width calculations (Local models)



Annex 1. Crack width calculations according to Eurocode 2 Part 1-1

Eurocode 2 part 1-1 expression (7.8) yields the crack width, w_k , as

$$w_k = s_{r,max}(\varepsilon_{sm} - \varepsilon_{cm}) \tag{1.1}$$

$$\varepsilon_{sm} - \varepsilon_{cm} = \frac{\sigma_s - k_t \frac{f_{ct,eff}}{\rho_{p,eff}} \left(1 + \alpha_e \rho_{p,eff} \right)}{E_s} \ge 0.6 \frac{\sigma_s}{E_s}$$
(1.2)

$$s_{r,max} = k_3 c + k_1 k_2 k_4 \phi / \rho_{p,eff}$$
 (1.3)

where	c	is the maximum crack spacing
WHELE	$S_{r.max} \ arepsilon_{sm}$	is the mean strain in the reinforcement
	\mathcal{E}_{cm}	is the mean strain in the concrete between crack
	00	
	$\sigma_{_S}$	is the stress in the tension reinforcement assuming cracked section
	k_t	is a factor dependent on the duration of the load
		(0.6 for short term and 0.4 for long term loading)
	$f_{ct,eff}$	is the mean value of tensile strength of the concrete
		effective at the time when cracks are first expected to
		occur
	$ ho_{p,eff}$	= $A_s/A_{c,eff}$ for solely reinforced sections
	A_s	is the area of tensile reinforcement
	$A_{c,eff}$	is the effective area of concrete in tension surrounding
	2,2,,	the reinforcement (here, $\sim 2.5c$ is used)
	α_e	is the ratio E_s/E_{cm}
	E_s	is the modulus of elasticity of steel reinforcement
	E_{cm}	is the secant modulus of elasticity of concrete
	k_1	is a coefficient taking into account the bond properties o
		bonded reinforcement (0.8 for high bond bars and 1.6
		for bars with an effectively plain surface
	k_2	is a coefficient taking into account the distribution of
	-	strain
		(0.5 for bending and 1.0 for pure tension)
	k_3	is a coefficient with recommended value of 3.4
	k_4	is a coefficient with recommended value of 0.425
	C	is the cover to the longitudinal reinforcement
		U



is the bar diameter

Annex 2. Crack width calculations (Global model)

Assumptions for parameters (see Annex 1 for details)

For all sections, $\rho_{p,eff} = \frac{A_s}{A_{c,eff}} = \frac{A_s^*}{A_{c,eff}^*}$, where "*" refers to area that is normalized to the thickness, t, of the section. $A_s^* = 0.0015$ and $A_{c,eff}^* = 2.5 \frac{c}{t} = 2.5 \cdot \left(\frac{0.1t}{t}\right) = 0.25$ as discussed in section 4.4.1 regarding the modelling of reinforcement. Therefore, $\rho_{p,eff} = \frac{0.0015}{0.25} = 0.006$.

Strength related parameters

- $f_{ct,eff} = 3 MPa$
- $E_s = 210 GPa$
- $E_{cm} = 30 \, GPa \, (creep \, not \, considered)$
- $\alpha_e = E_s/E_{cm} = 210/30 = 7$

The load combination is assumed to be long term combination and thus $k_t = 0.4$.

The bond between bars is assumed to be strong and therefore $k_1 = 0.8$. The temperature boundary conditions tend to induce bending strain distribution, as shown by Figure 20, thus $k_2 \approx 0.5$.

Bar diameters are assumed to be $\phi = 12 \, mm$ and $\phi = 16 \, mm$ for floor and wall, respectively.

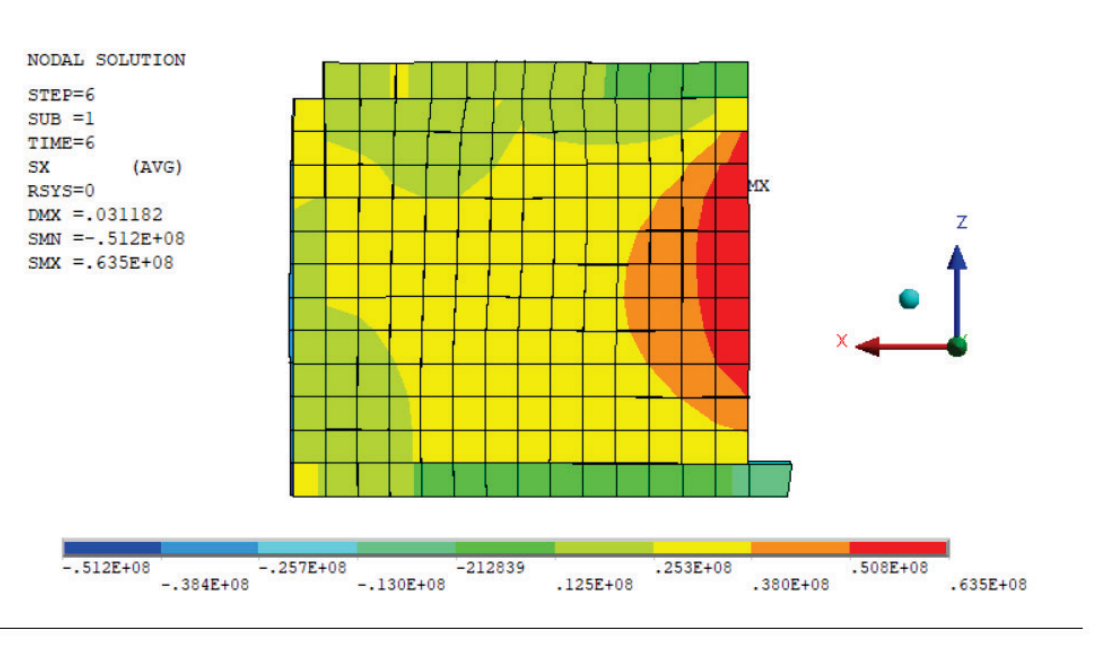
Crack width estimates

Crack width estimates concerning the studied room are made for both the wall surrounding the room and the floor that is above the room (see Figure 24). The thickness of the wall in question is 700 mm and the concrete cover is assumed to be 10 % of the thickness equalling 70 mm. Respective values for the floor are 500 mm and 50 mm mm. With these values, the maximum crack spacing, $s_{r.max}$, gets values of 691.3 mm and 510.0 mm for the wall and floor, respectively.

Global modelling showed maximum stresses in reinforcement where maximum principal plastic strains for concrete were maximized. This is intuitive because of the perfect bond assumed between concrete and reinforcement. The axial stress distribution of reinforcement at load step 6 is shown in Figure 2.1, according to the results given by FEM. Due to ideal-plasticity, the FEM results do not consider the loss of tensile capacity of concrete which increases the stresses in the reinforcement. This is taken into account by manually transferring forces from cracked concrete to the reinforcement. The process is covered in more detail in Annex 3, where an example is given with the local model (the process is the same for global and local model). The reinforcement stresses given by FEM and by the transfer process are given in Table 2.1. Then, in Table 2.2 the crack width estimates are given for both wall and the upper floor.







b)

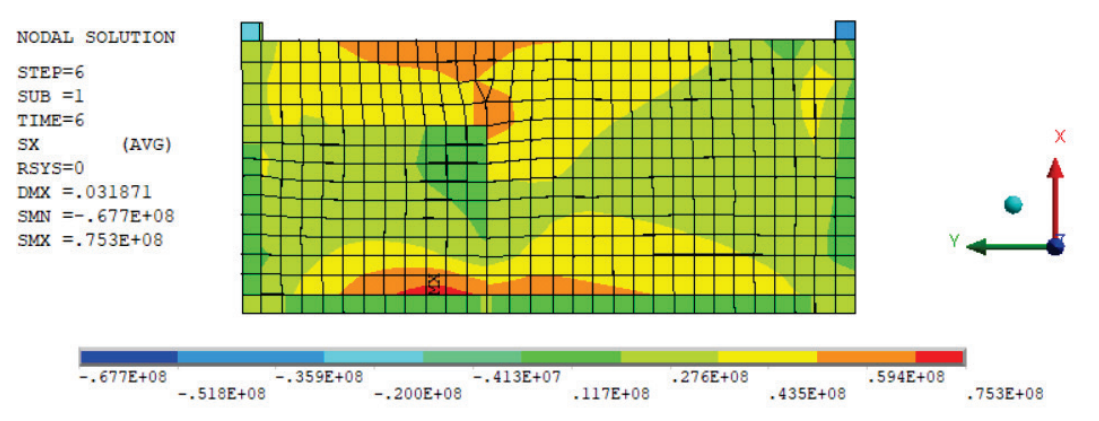


Figure 2.1. Axial stress distribution in reinforcement at the *a*) wall and *b*) above floor.



Table 2.1. The reinforcement stress components in the global model with total stress $\sigma_s = \sigma_{s.FEM} + \sigma_{s.crack}$. Load step 3 is not considered as it did not result into plastic strains in these positions.

Position	Load step	$\sigma_{s.FEM}$ [MPa]	$\sigma_{s.crack}$ [MPa]	σ_{s} [MPa]
	4	19.0	42.7	61.7
Wall	5	42.5	145.2	187.7
	6	63.5	262.2	325.7
	4	30.2	98.1	128.3
Floor	5	52.0	178.8	230.8
	6	75.0	301.3	376.3

Table 2.2. Maximum axial stress in reinforcement, strain difference and estimated crack widths of the studied room according to global model.

Load step	Measure	Wall	Floor
	σ_s (MPa)	No cracking*	No cracking*
3	$\varepsilon_{sm} - \varepsilon_{cm} (-)$	_	_
	$w_k (mm)$	_	_
	σ_s (MPa)	61.7	128.3
4	$\varepsilon_{sm} - \varepsilon_{cm} (-)$	$1.76 \cdot 10^{-4}$	$3.67 \cdot 10^{-4}$
	$w_k (mm)$	0.122	0.187
	σ_s (MPa)	187.7	230.8
5	$\varepsilon_{sm} - \varepsilon_{cm} (-)$	$5.36 \cdot 10^{-4}$	$6.59 \cdot 10^{-4}$
	$w_k (mm)$	0.371	0.336
	σ_s (MPa)	325.7	376.3
6	$\varepsilon_{sm} - \varepsilon_{cm} (-)$	$9.31 \cdot 10^{-4}$	$1.08 \cdot 10^{-3}$
	$w_k (mm)$	0.643	0.548

^{*}No plastic strains at this load step in positions where crack widths were evaluated.



Annex 3. Crack width calculations (Local model)

In the local model, crack widths are evaluated from three different positions. See Figure 32 for the positions. The positions are named "floor above", "left wall" and "front wall" according to their location in the figure. All the parameters not mentioned here are the same as in Annex 1 and Annex 2. Concrete cover, c=50 mm is assumed in local model. Variables changing by position are σ_s , A_s , $A_{c,eff}$, ϕ , $s_{r,max}$ and $\varepsilon_{sm}-\varepsilon_{cm}$. Furthermore, variable s is used to denote the rebar spacing.

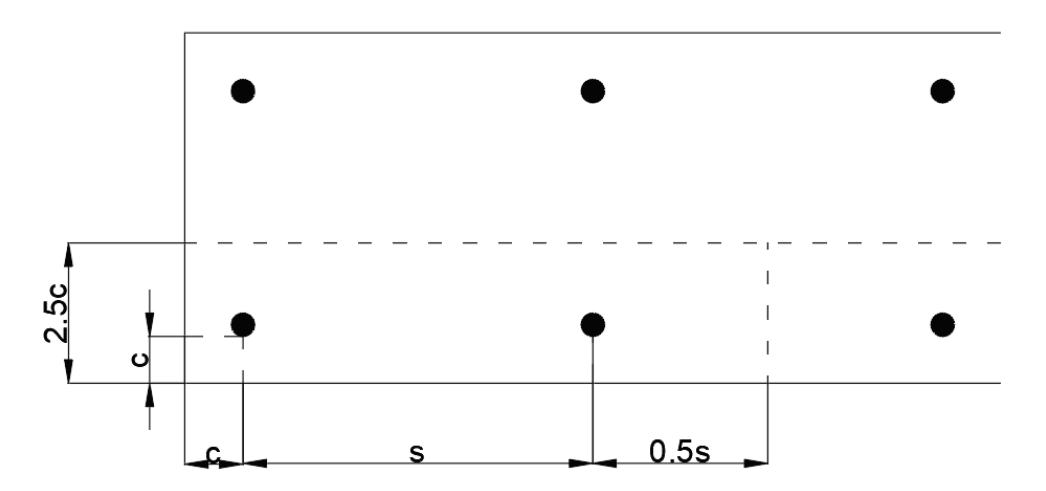


Figure 3.1. Floor or wall cross-section with rebar dimensioning.

Atleast n=2 reinforcing bars are used to average the axial stresses in the reinforcement. Figure 3.1 shows a floor or wall cross-section with rebars marked with black circles. $A_{c,eff}$ is determined by two different equations depending on the location of the rebars used in averaging. $A_{c,eff}$ is given by

$$A_{c,eff} = \begin{cases} 2.5c \cdot (c + (n-1)s + 0.5s), if \ rebar \ lays \ on \ edge \\ 2.5c \cdot (ns), if \ no \ rebar \ lay \ on \ edge \end{cases}$$

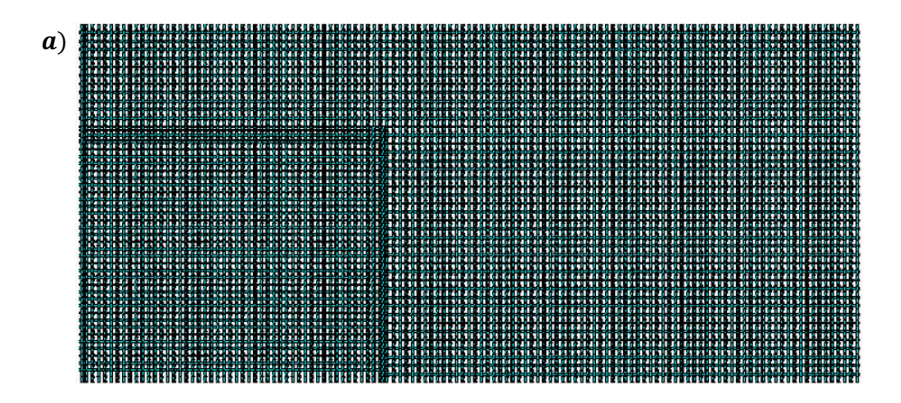
 A_s is given by $A_s = \frac{n\pi}{4} \cdot \phi^2$. Table 3.1 summarizes the varying values for each position.

	Floor above	Left wall	Front wall	
φ (mm)	12	16	16	
Maximum rebar stress direction (global)	Х	Z	Υ	
s (mm)	125	400	400	
n (-)	6	2	2	
$A_s (mm^2)$	678.58	402.12	402.12	
$A_{c.eff} \ (mm^2)$	93750	81250 (edge)	81250 (edge)	
$\rho_{p,eff}$ (-)	0.00724	0.00495	0.00495	
$s_{r.max} (mm)$	451.84	719.58	719.58	

Table 3.1. Crack width variables for each considered position.



Figures 3.2, 3.3 and 3.4 show the reinforcing bars on the layer where maximum axial stress occurs together with axial stresses at load step 6 and a representation of the elements used in reinforcement stress averaging. These elements are the same for all local models as the largest axial stresses tend to occur on these localized positions regardless of temperature distribution or consideration of creep.



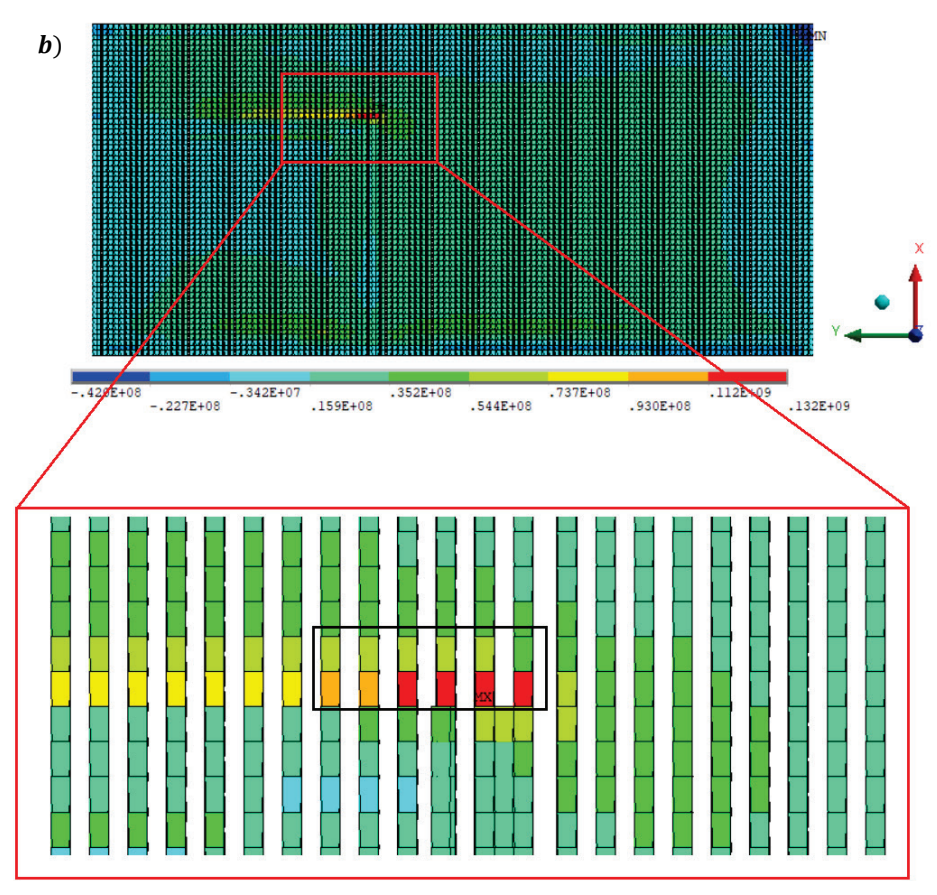
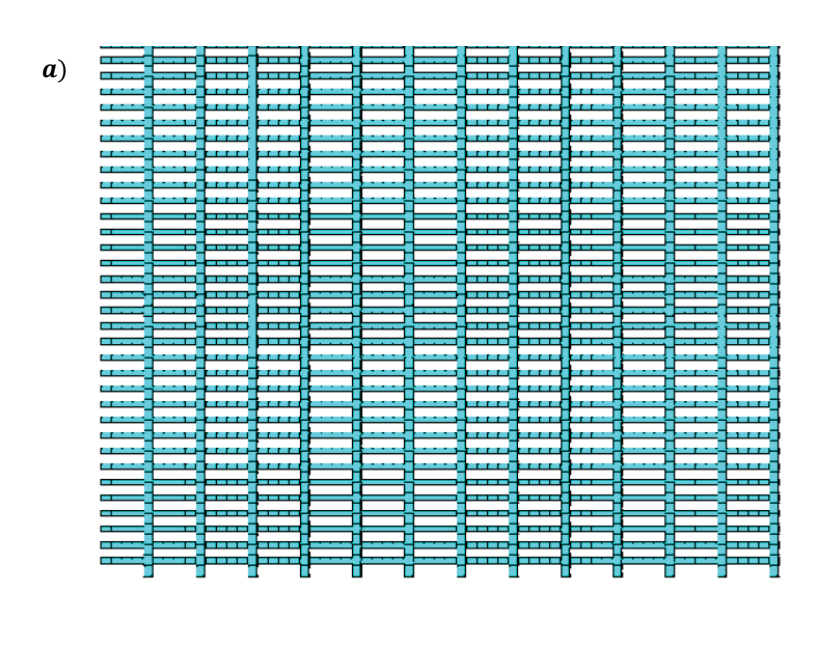


Figure 3.2. *a*) Tensile reinforcing layer and *b*) the axial stress in global X-direction at load step 6 of "floor above". Black rectangle represents the elements used in averaging. Results are from model with linear temperature distribution and nominal modulus of elasticity.





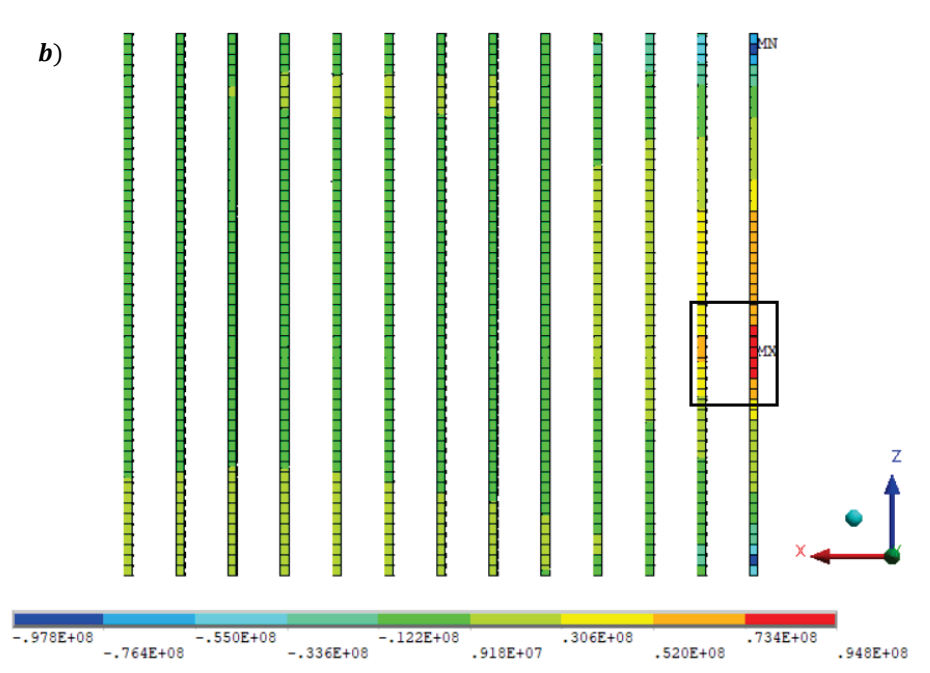
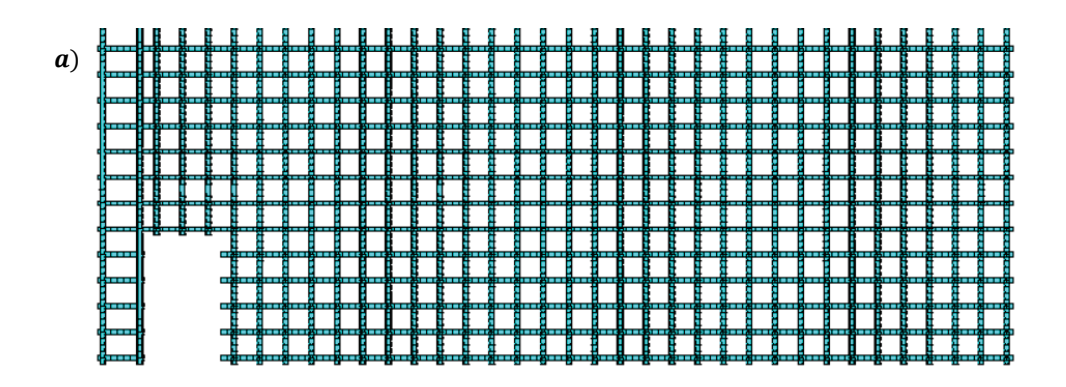


Figure 3.3. *a*) Tensile reinforcing layer and *b*) the axial stress in global Z-direction at load step 6 of "left wall". Black rectangle represents the elements used in averaging. Results are from model with linear temperature distribution and nominal modulus of elasticity.





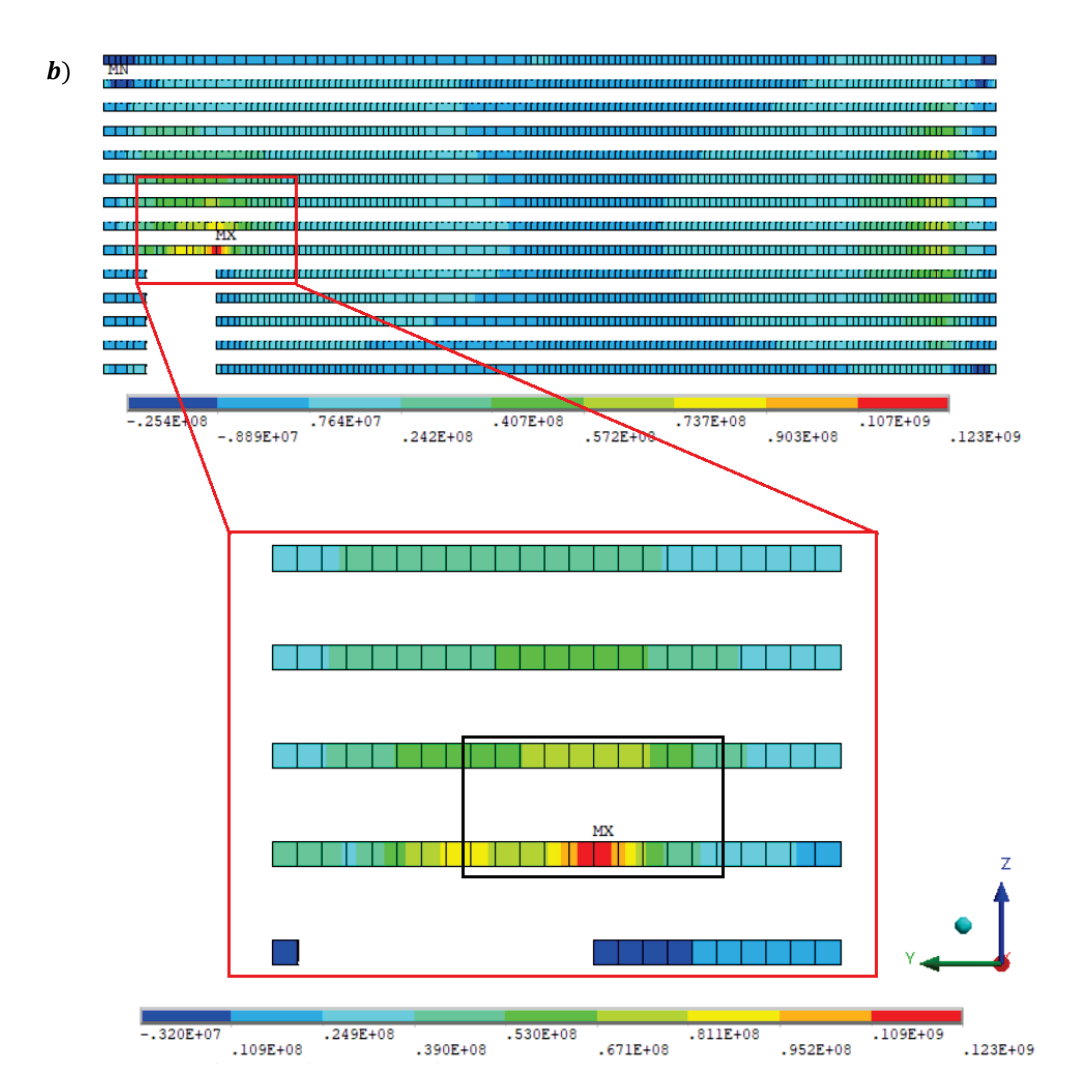


Figure 3.4. *a*) Tensile reinforcing layer and *b*) the axial stress in global Y-direction at load step 6 of "front wall". Black rectangle represents the elements used in averaging. Results are from model with linear temperature distribution and nominal modulus of elasticity.



As the material model used in finite element modelling is ideally-plastic, it does not consider the loss of tensile capacity automatically, and therefore it underestimates the stresses in reinforcement. This is manually taken into account in the crack width estimates as follows. A conservative estimate is made where it is assumed that concrete has no tensile capacity when tensile plastic strains are formed. In the positions where crack widths are estimated, a sectional cut is taken with plastic strains presented. Then, the cross-sectional area of concrete that has plastic strains, $A_{cracked}$, is calculated. Then, the force that is transferred to reinforcement from the cracked concrete is $F_{transfer}$ = $A_{cracked} \cdot f_{ct,eff}$. This force is distributed to the reinforcement that lies on the tensile side of the corresponding floor or wall slab. As the plastic strain distribution is not uniform, distributing the forces to all the tension rebars effectively averages the stresses in the reinforcement. The plastic strain is considered "zero" between range $0...5 \cdot 10^{-5}$ (see results coloring in Figure 3.5), where $5 \cdot 10^{-5}$ corresponds to 1/2 of the tensile strain of concrete.

Although the stresses in the reinforcement are averaged (non-conservative simplification), the process is conservative in the sense that it assumes that the tensile stresses from the cracked concrete are fully transferred to the reinforcement in one global coordinate direction. In other words, it is assumed that the cracks are perpendicular to the reinforcement. This direction depends on the maximum rebar stress direction as shown by Table 3.1. Realistically, the forces are also transferred to the reinforcement that is perpendicular to the chosen direction, unless the tensile forces in concrete are actually directed towards the chosen direction. Due to complexity of the structure, with geometric nonlinearities, it is unlikely that such a situation would occur.

Figure 3.5 shows an example of the process, where position "floor above" is considered. For example, let us consider load step 4. In the figure, A_{cracked} is estimated by a right triangle, with height h_c and width w_c so that

$$A_{cracked} = \frac{1}{2}h_c w_c.$$

With $h_c = 130 \, mm$ and $w_c = 2\,820 \, mm$, the transferrable force is

$$F_{transfer} = \frac{1}{2} h_c w_c \cdot f_{ct,eff} = \frac{1}{2} \cdot 130 \cdot 2820 \ mm^2 \cdot 3 \frac{N}{mm^2} = 452700 \ N.$$

Table 3.1 shows that the diameter of rebar and rebar spacing in this position are $\phi =$ 12 mm and $s_{r.max} = 125$ mm. With slab width $w_s = 5300$ mm, the number of rebar in the slab, n, and the area of reinforcement $A_{s.crack}$ are

$$n = \frac{w_S}{s_{r,max}} = \frac{5300 \ mm}{125 \ mm} = 42.4,$$

$$A_{s.crack}=n\cdot\pi\cdot\frac{\phi^2}{4}=42.4\cdot\pi\cdot\frac{(12\ mm)^2}{4}pprox4795.3\ mm^2.$$
 Therefore, the extra stress in reinforcement due to cracked concrete is

$$\sigma_{s.crack} = \frac{F_{transfer}}{A_{s.crack}} = \frac{452\ 700\ N}{4795.3\ mm^2} \approx 94.4 \frac{N}{mm^2}.$$

This is added to the reinforcement stress given by FEM for the crack width calculations.



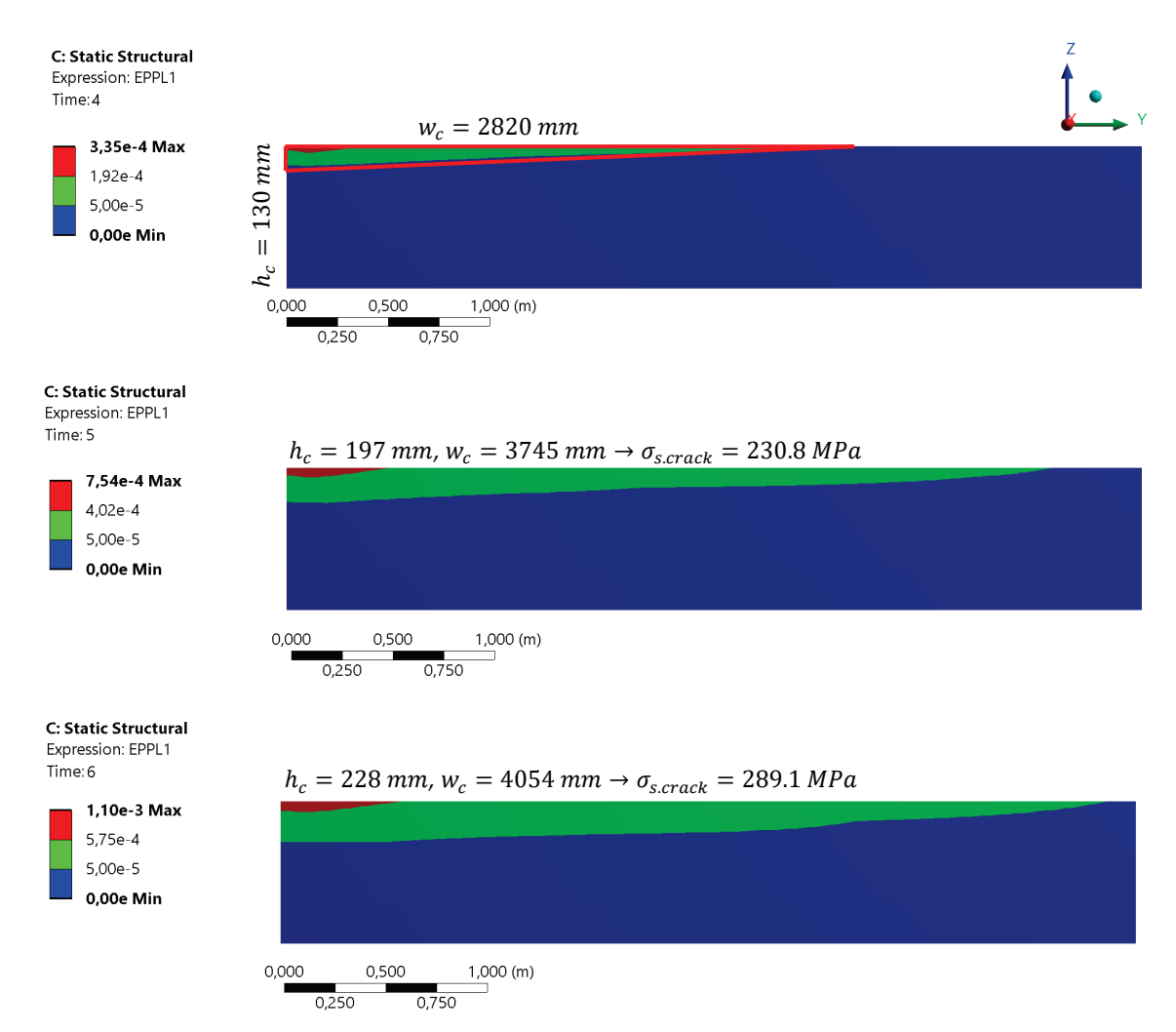


Figure 3.5. Example of a force transferal between cracked concrete and reinforcement. The position is "floor above" with load steps 4 to 6.

Table 3.2 summarizes the components of reinforcement stresses used in the crack width estimates with nominal modulus of elasticity. As the table shows, $\sigma_{s.crack}$ dominates the total stress σ_s often being two to three times larger than $\sigma_{s.FEM}$. Table 3.3 summarizes these for the creep modified modulus of elasticity. As Table 3.3 shows, with creep modified modulus of elasticity the magnitudes of $\sigma_{s.crack}$ are significantly smaller which can be explained by the substantially smaller extent of plastic strains as compared to the analyzes made with nominal modulus of elasticity.

Table 3.2. The reinforcement stress components with nominal modulus of elasticity and the total stress $\sigma_s = \sigma_{s.FEM} + \sigma_{s.crack}$.

Position	Load step	$\sigma_{s.FEM}$	[MPa]	σ [MDa]	σ_s [MPa]	
POSITION		Avg.	Max.	$\sigma_{s.crack}$ [MPa]	Avg.	Max.
	4	28.6	47.2	94.4	123.0	141.6
Floor above	5	60.9	92.3	230.8	291.7	323.1
	6	90.8	131.6	289.1	379.9	420.7
	4	17.8	24.9	26.5	44.3	51.4
Left wall	5	40.8	61.9	106.7	147.5	168.6
	6	62.2	94.8	167.3	229.5	262.1
	4	25.9	47.0	89.9	115.8	136.9
Front wall	5	49.8	88.9	159.3	209.1	248.2
	6	72.3	123.3	336.1	408.4	459.4

Table 3.3. The reinforcement stress components with creep modified modulus of elasticity and the total stress $\sigma_s = \sigma_{s.FEM} + \sigma_{s.crack}$.

5 5.1 Lin 5.01 uck						
Position	Load step	$\sigma_{s.FEM}$	[MPa]	σ [MDa]	σ_s [MPa]	
FUSICIOII		Avg.	Max.	$\sigma_{s.crack}$ [MPa]	Avg.	Max.
	4	21.3	24.5	0.0	21.3	24.5
Floor above	5	38.5	54.2	23.3	61.8	77.5
	6	56.0	89.0	107.3	163.3	196.3
	4	17.0	22.5	0.0	17.0	22.5
Left wall	5	29.3	38.2	0.0	29.3	38.2
	6	40.7	54.9	2.7	43.4	57.6
	4	22.0	32.3	4.6	26.6	36.9
Front wall	5	36.5	57.9	17.3	53.8	75.2
	6	51.2	89.2	105.4	156.6	194.6



Crack width estimates for local models with linear temperature distribution

Tables 3.4 and 3.5 present the averaged and maximum axial stresses in reinforcement together with strain difference and maximum crack width for load steps 4 to 6 with nominal and creep modified modulus of elasticity, respectively. Table 3.3 included entries where $\sigma_{s.crack} = 0$ MPa, which can be interpreted to mean that the section has not cracked yet in the analysis made by using the creep modified modulus of elasticity. These entries are considered in Table 3.5 by noting that no cracking occurs at that load step and position.

Table 3.4. Maximum crack width estimates of the local model with linear temperature distribution and nominal modified modulus of elasticity.

		Floor above		Left wall		Front wall	
Load step	Measure	Avg.	Max.	Avg.	Max.	Avg.	Max.
	σ_s (MPa)	123.1	141.6	44.4	51.4	115.8	136.9
4	$\varepsilon_{sm} - \varepsilon_{cm} \; (-)$	$3.5\cdot 10^{-4}$	$4.0 \cdot 10^{-4}$	$1.3 \cdot 10^{-4}$	$1.5 \cdot 10^{-4}$	$3.3 \cdot 10^{-4}$	$3.9 \cdot 10^{-4}$
	$w_k (mm)$	0.159	0.183	0.091	0.106	0.238	0.281
	σ_s (MPa)	291.7	323.1	147.5	168.6	209.1	248.2
5	$\varepsilon_{sm} - \varepsilon_{cm} \; (-)$	$8.3 \cdot 10^{-4}$	$9.2 \cdot 10^{-4}$	$4.2 \cdot 10^{-4}$	$4.8 \cdot 10^{-4}$	$6.0 \cdot 10^{-4}$	$7.1 \cdot 10^{-4}$
	$w_k (mm)$	0.377	0.417	0.303	0.347	0.430	0.510
	σ_s (MPa)	379.9	420.7	229.5	262.1	408.4	459.4
6	$\varepsilon_{sm} - \varepsilon_{cm} \; (-)$	$1.1 \cdot 10^{-3}$	$1.2 \cdot 10^{-3}$	$6.6 \cdot 10^{-4}$	$7.5 \cdot 10^{-4}$	$1.2 \cdot 10^{-3}$	$1.3 \cdot 10^{-3}$
	$w_k (mm)$	0.490	0.543	0.472	0.539	0.84	0.945

Table 3.5. Maximum crack width estimates of the local model with linear temperature distribution and creep modified modulus of elasticity.

		Floor above		Left wall		Front wall	
Load step	Measure	Avg.	Max.	Avg.	Max.	Avg.	Max.
	σ_s (MPa)	_	_	_	_	26.6	36.9
4	$\varepsilon_{sm} - \varepsilon_{cm} \; (-)$	_	_	_	_	$7.6 \cdot 10^{-5}$	$1.1 \cdot 10^{-4}$
	$w_k (mm)$	No cracks	No cracks	No cracks	No cracks	0.055	0.076
	σ_s (MPa)	61.8	77.5	_	_	53.8	75.2
5	$\varepsilon_{sm} - \varepsilon_{cm} \; (-)$	$1.8 \cdot 10^{-4}$	$2.2 \cdot 10^{-4}$	_	_	$1.5 \cdot 10^{-4}$	$2.1 \cdot 10^{-4}$
	$w_k (mm)$	0.080	0.100	No cracks	No cracks	0.111	0.155
	σ_s (MPa)	163.3	196.3	43.4	57.6	156.6	194.6
6	$\varepsilon_{sm} - \varepsilon_{cm} \; (-)$	$4.7 \cdot 10^{-4}$	$5.6 \cdot 10^{-4}$	$1.2\cdot 10^{-4}$	$1.6 \cdot 10^{-4}$	$4.5\cdot 10^{-4}$	$5.6 \cdot 10^{-4}$
	$w_k (mm)$	0.211	0.253	0.089	0.118	0.322	0.400



EFFECT OF ROOM TEMPERATURE DIFFERENCES ON SAFETY-RELATED REINFORCED CONCRETE FLOORS AND WALLS IN THE REACTOR BUILDING OF OL2 NPP

The goal of this study was to estimate the magnitudes of thermal stresses compared to structural, mechanical stresses in normal operational conditions and to determine if the thermal stresses are large enough to cause significant crack widths.

The results suggests that thermal stresses can induce tensile stresses that exceed those induced by the mechanical stresses in the reactor building even with temperature differences of 20 °C. However, the crack widths evaluated are smaller than a recommended value of 0.3 mm with the current temperature distribution with a maximum temperature of some 40 °C. The results also suggest that the integrity of the reactor building is not critically impaired in normal operational conditions between 20 and 65 °C. However, attention should be given to situations where thermal and mechanical stresses simultaneously induce tension to a structural piece.

Furthermore, the study also includes a literature review on the temperature dependence of the thermal and mechanical properties of concrete. In the studied temperature range, the thermal properties showed no significant temperature dependence. As for the mechanical properties, compressive stress and strain as well as the modulus of elasticity showed considerable temperature dependence, although some models suggested negligible dependence.

Energiforsk is the Swedish Energy Research Centre – an industrially owned body dedicated to meeting the common energy challenges faced by industries, authorities and society. Our vision is to be hub of Swedish energy research and our mission is to make the world of energy smarter!

